Technical Physics Letters, Vol. 26, No. 2, 2000, pp. 102–104. Translated from Pis'ma v Zhurnal Tekhnicheskoĭ Fiziki, Vol. 26, No. 3, 2000, pp. 23–29.

Bandwidth of Synchronous Generation in the Chains and Lattices of Josephson Junctions with Finite Interaction Radius

V. K. Kornev and A. V. Arzumanov

Moscow State University, Moscow, 119899 Russia

Received July 27, 1999

Abstract—The bandwidth of synchronous generation in one- and two-dimensional multielement Josephson structures exhibits narrowing with increasing number of elements, but only as far as the system dimensions remain smaller compared to the effective radius of electrodynamic coupling between the Josephson junctions.

INTRODUCTION

The use of synchronized multielement Josephson structures instead of a single Josephson junction is a promising way to the creation of synchronous generators of a narrow-band electromagnetic radiation in the submillimeter and near-IR wavelength range [1]. For example, the bandwidth of synchronous generation may decrease in inverse proportion to the number N of Josephson elements in one-dimensional chains and drop even more rapidly with increasing N in two-dimensional structures [2, 3].

Recently, we suggested multielement structures of a new type in which the coherent Josephson generation regime is stable with respect to technological scatter of the Josephson junction parameters within rather broad limits (40–50%). This is achieved as a result of strong interaction between all Josephson elements in the system [4–6]. However, virtually all real electrodynamic coupling circuits that may ensure a nonlocal character of the interaction between the Josephson elements are characterized by finite effective radius of interaction.

The purpose of this work was to study the effect of the finite radius of interaction between the Josephson elements in one- and two-dimensional systems on the character of variation of the bandwidth of synchronous generation depending on the number of Josephson elements in these structures.

ONE-DIMENSIONAL CHAINS OF JOSEPHSON JUNCTIONS

The simplest model system for investigation of the effect of the finite radius of interaction between Josephson elements on the bandwidth of coherent generation is offered by a chain of parallel elements, in which the Josephson junctions are coupled by superconducting inductors with the inductance L (Fig. 1a). All the Josephson elements in this structure possess the same generation frequency $\omega = (2e/\hbar)V$, where V is the constant component of the voltage across the chain. In the absence of magnetic fields, there is additional synchronous oscillation of the voltage across all Josephson junctions in the chain. The radius of effective coupling between Josephson elements in this structure depends on the normalized coupling inductance $l = (2e/\hbar)I_cL$, where I_c is the critical current along a single Josephson junction. For simplicity, it is assumed that all the Josephson elements are identical and can be described by a model of resistor with capacitor (RCSJ model) [7].

Figure 2 shows a family of plots describing variation of the generation bandwidth $\Delta\omega$ versus the number N of the Josephson elements in the chains with various normalized coupling inductances l. To simplify representation, the curves are constructed using algorithmic frequency scale and linear N scale, whereby the plots of $\Delta\omega$ versus $1/N$ must be linear. As seen, the bandwidth decreases in proportion to N in systems with small numbers of elements. As the N value increases, the

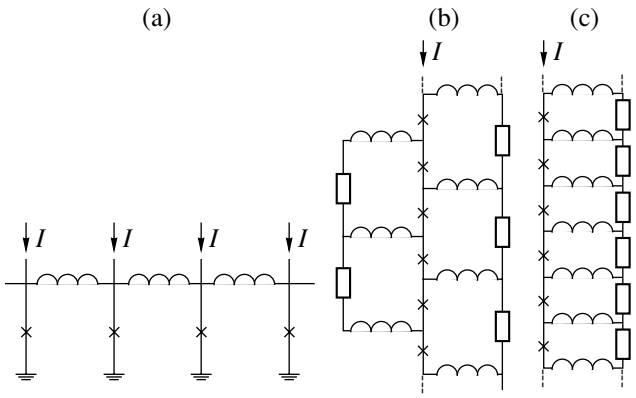

Fig. 1. Model one-dimensional structures of Josephson elements with electrodynamic coupling chains of various types.

effect of band narrowing exhibits "saturation." This phenomenon is related to the fact that the chain size becomes comparable with the radius of effective interaction between Josephson elements in the structure. The further increase in N does not affect the generation bandwidth. As is known from practice, it is difficult to reduce the parameter l markedly below unity. Therefore, more than 100-fold decrease in the generation bandwidth can hardly be achieved in this linear system.

Figures 1b and 1c show the model chains of serial Josephson elements with different electrodynamic coupling circuits. The dynamic properties of these systems were recently studied in [3, 4, 6]. In the structure of Fig. 1b, the Josephson elements are coupled in pairs, which implies a local character of the electrodynamic coupling. Here, the effect of the generation bandwidth narrowing is manifested only within a single elementary unit ($N = 2$) and no decrease in $\Delta\omega$ is observed for $N > 2$. This result was reported previously [1], where the effect was commented as "unexpected." In the other parallel structure (Fig. 1c), the effective radius of interaction between Josephson elements is formally infinite and this system must, in principle, feature a continuous decrease in the bandwidth of synchronous generation in proportion to the number of Josephson elements in the chain. However, we may suggest that a distributed character of such structures at large N values in real experiments would also give rise to saturation in the effect of bandwidth narrowing.

TWO-DIMENSIONAL JOSEPHSON STRUCTURES

Figure 3a shows a two-dimensional structure composed of unit cells representing four-contact interferometers. In this structure, a strong interaction between Josephson elements is provided by the motion of spatially-periodic system of single magnetic-flux quanta [1, 5]. It was previously established that the synchronous generation bandwidth of such a unit cell decreases in proportion to N^2, that is, drops by a factor of $N_1^2 = 16$ as compared to the bandwidth of a single Josephson junction [3].

The results of our investigation showed that, as far as the structure dimensions do not exceed the effective radius of electrodynamic coupling of the Josephson elements, the spectral linewidth of the coherent radiation measured decreases in proportion to the number of unit cells K. Provided the optimum values of the Maccumber parameter $\beta = (2e/\hbar)I_c R_n^2 C \sim 1$ (R_n and C are the normal resistance and capacitance of the Josephson junction) and the normalized inductance $l \sim 10$, the effective electrodynamic coupling radius in this system is equivalent to the size of three unit cells in each direction. Thus, the maximum possible effect of the generation bandwidth narrowing in the system studied is approximately $8N_1^2 \sim 100$.

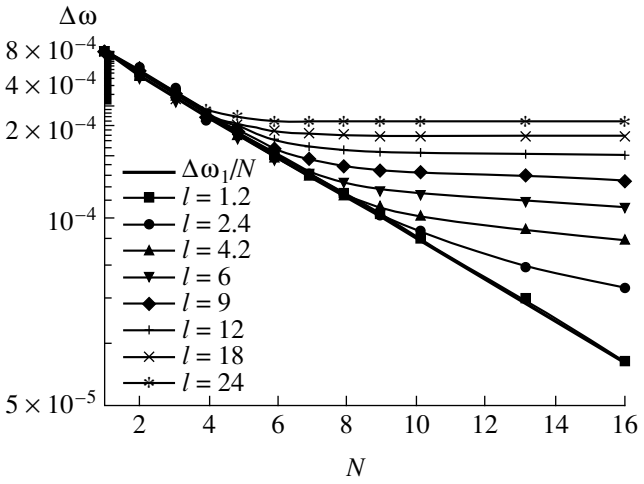

Fig. 2. Plots of the Josephson generation bandwidth $\Delta\omega$ vs. number N of the Josephson elements in the parallel chain (Fig. 1a) for various values of the normalized coupling inductance l.

Should the size of the two-dimensional structure exceed the effective radius of interaction between elements, the spectral line exhibits splitting into several closely spaced components (see the spectra presented in Fig. 3b), so that the total linewidth becomes even greater than that before splitting (cf. data in Tables 1 and 2). The system dynamics is such that the instantaneous oscillation frequency exhibits a periodic switching from one to another component at a certain beat frequency of ω_b, as evidenced by the corresponding component in the generation spectrum. This is probably

Table 1. The bandwidth of the Josephson generation in a two-dimensional structure (Fig. 3a) at $\omega/\omega_c = 1$ for $l = 1$, $\beta = 10$, and $\gamma \equiv \pi s_i(0) = 2 \times 10^{-4}$, where $s_i(0)$ is the normalized spectral density of fluctuations of the low-frequency current $i \equiv I/I_c$

	Single junction (J)	4J-cell	3×2 lattice structure	3×3 lattice structure	3×4 lattice structure
$\Delta\omega/\omega_c$	1.3×10^{-3}	7.5×10^{-5}	1.7×10^{-5}	2.6×10^{-5}	3.4×10^{-5}

Table 2. The bandwidth of the Josephson generation in a two-dimensional structure of one vertical cell column (dashed contour in Fig. 3b) at $\omega/\omega_c = 1$ for $l = 1$, $\beta = 10$, and $\gamma \equiv \pi s_i(0) = 2 \times 10^{-4}$

	2 cells	3 cells	4 cells	5 cells
$\Delta\omega/\omega_c$	$3/7 \times 10^{-5}$	1×10^{-4} (3 lines)	7.5×10^{-5}	2×10^{-4} (5 lines)

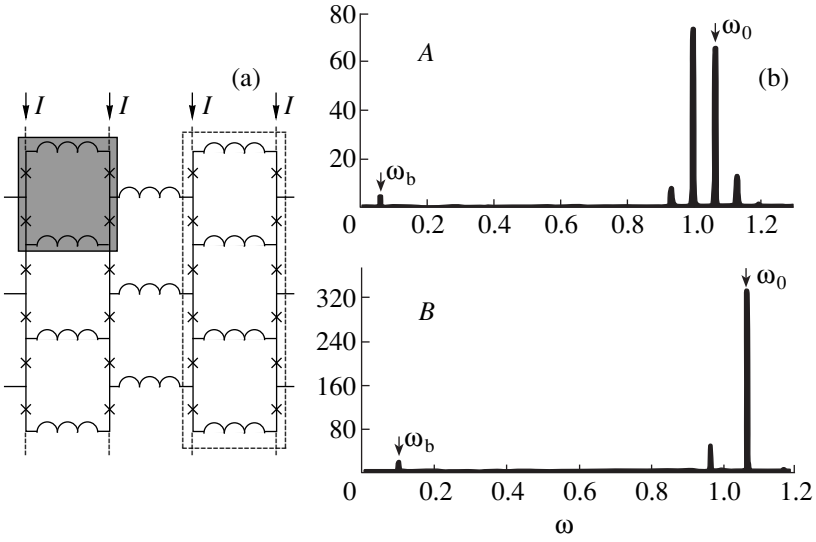

Fig. 3. (a) Model two-dimensional structures of Josephson elements representing four-contact superconducting interferometers and (b) typical spectra of the Josephson radiation from a structure with dimensions exceeding the effective radius of electromagnetic coupling: (*A*) a column of 5 cells (indicated by dashed contour); (*B*) a lattice structure of 3×5 unit cells (ω_0 is the average Josephson generation frequency; ω_b is the beat frequency).

related to the formation and motion of hypervortices in these structures.

CONCLUSION

The main conclusion of this work is that the effect of narrowing of the coherent generation bandwidth with increasing number of elements in one- and two-dimensional multielement Josephson structures is observed as far as the characteristic system size does not exceed the effective radius of electrodynamic coupling between Josephson junctions in the structure studied. Estimates indicate that a maximum degree of the generation bandwidth narrowing achievable in real systems cannot exceed 100. We believe that the creation of synchronous generators of a narrow-band electromagnetic radiation in the submillimeter wavelength range should be based on multielement Josephson structures with distributed electrodynamic coupling parameters, which would provide for additional decrease in the generation bandwidth as a result of resonance properties of these coupling circuits [8].

ACKNOWLEDGMENTS

This work was supported in parts by the State Program “Actual Directions in the Physics of Condensed Media” (project no. 98051), the Federal Program “Integration” (project no. AO111), and a special program of the Ministry of Education of the Russian Federation (project no. 97-8.3-58).

REFERENCES

1. V. K. Kornev, A. V. Arzumanov, A. D. Mashtakov, *et al.*, IEEE Trans. Appl. Supercond. **7**, 3111–3114 (1997).
2. A. K. Jaĭn, K. K. Likharev, J. E. Lukkens, *et al.*, Phys. Rep. **109**, 309 (1984).
3. V. K. Kornev and A. V. Arzumanov, Pis’ma Zh. Tekh. Fiz. **24**, 52 (1998).
4. A. D. Mashtakov, V. K. Kornev, and G. A. Ovsyannikov, Radiotekh. Elektron. **40**, 1735 (1995).
5. V. K. Kornev, A. D. Mashtakov, and G. A. Ovsyannikov, Pis’ma Zh. Tekh. Fiz. **20**, 44 (1994).
6. A. V. Arzumanov, V. K. Kornev, G. A. Ovsyannikov, *et al.*, Pis’ma Zh. Tekh. Fiz. **24**, 1 (1998).
7. K. K. Likharev, *Introduction to the Dynamics of Josephson Junctions* (Nauka, Moscow, 1985).
8. V. K. Kornev and A. V. Arzumanov, in *Extended Abstr. 7th Int. Conf. Superconductive Electronics (ISEC-99), Berkeley, USA, June 21–25, 1999*, pp. 437.

Translated by P.P. Pozdeev

Technical Physics Letters, Vol. 26, No. 2, 2000, pp. 105–106. Translated from Pis'ma v Zhurnal Tekhnicheskoĭ Fiziki, Vol. 26, No. 3, 2000, pp. 30–34.

The Effect of the Filler Particle Size on the Efficiency of Mechanoelectrical Transformations in Concretes

T. V. Fursa and V. F. Gordeev

Tomsk Polytechnic University, Tomsk, 634034 Russia

Received May 18, 1999

Abstract—The mechanoelectrical transformations in concretes were studied using the method of physical modeling. It is demonstrated that the filler particle size has a decisive effect on the efficiency of mechanoelectrical transformations in concretes. Dependence of the amplitude of electromagnetic response to shock excitation on the surface area of inclusions is determined. © *2000 MAIK "Nauka/Interperiodica".*

As was demonstrated by the results of previous investigations, a mechanical excitation of multicomponent heterogeneous materials consisting of a binder and a filler (in particular, concretes) gives rise to electromagnetic emission whose efficiency is determined by the presence of filler in the material and by the quality of the adhesion contact between filler and matrix [1–3]. It was the objective of this study to investigate the effect of the filler particle size on the efficiency of mechanoelectrical transformations (MET) in concretes.

For solving the problem set, special experiments were performed using the method of physical modeling. A series of model samples sized $5 \times 5 \times 10$ mm were manufactured of cement stone with various inclusions (in particular, metal plates, soda-lime glass, ceramics, rubber, and cardboard) of various dimensions. The choice of inclusions was governed, on the one hand, by the principle of different MET efficiency: the inclusions such as glass and ceramics exhibit a fairly high intrinsic efficiency, while metals, rubber, and cardboard are characterized by very low efficiency. On the other hand, these inclusions differ by their physical and mechanical characteristics. Note that, in order to eliminate the effect of the cement matrix on the conditions of acoustic wave propagation through the sample, all samples in the series were manufactured from the same manually prepared batch of cement–sand mixture and processed in a single mold divided by spacers into sections.

The mechanoelectrical transformations were investigated with the aid of an EMISSION setup [4]. The testing procedure was as follows: a special electromechanical device was used to produce a single impact (normalized in force) against the surface of the sample being tested. An electromagnetic response in the sample was recorded by a capacitive electrical detector located at a distance of 5 mm from the surface. A computer was used for automatic triggering, digitizing, and recording of signals.

The results of testing model samples comprising a cement stone with single inclusion demonstrated a fairly high efficiency of MET in all samples. Note that, under conditions of shock excitation of model samples consisting of pure cement stone without inclusions, almost no electromagnetic response is recorded. Consequently, whatever the mechanical and acoustoelectrical properties of the inclusions, their introduction into a cement–sand mixture results in a considerable increase of the efficiency of MET compared with pure cement stone.

It has been found that the size (area) of inclusions is decisive from the standpoint of variation of the amplitude of electromagnetic response to shock excitation (Fig. 1). The obtained dependence covers inclusions characterized by different values of the efficiency of MET and differing by their physical and mechanical properties (metal, glass, ceramics, rubber, cardboard).

As seen from Fig. 1, the amplitude of electromagnetic response increases in proportion to the size of

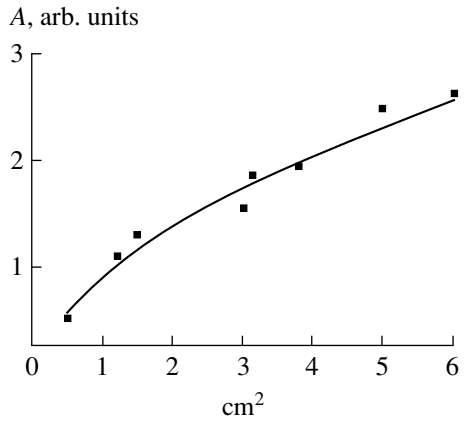

Fig. 1. The amplitude of electromagnetic response as a function of the area of inclusion placed into a cement sample.

1063-7850/00/2602-0105$20.00 © 2000 MAIK "Nauka/Interperiodica"

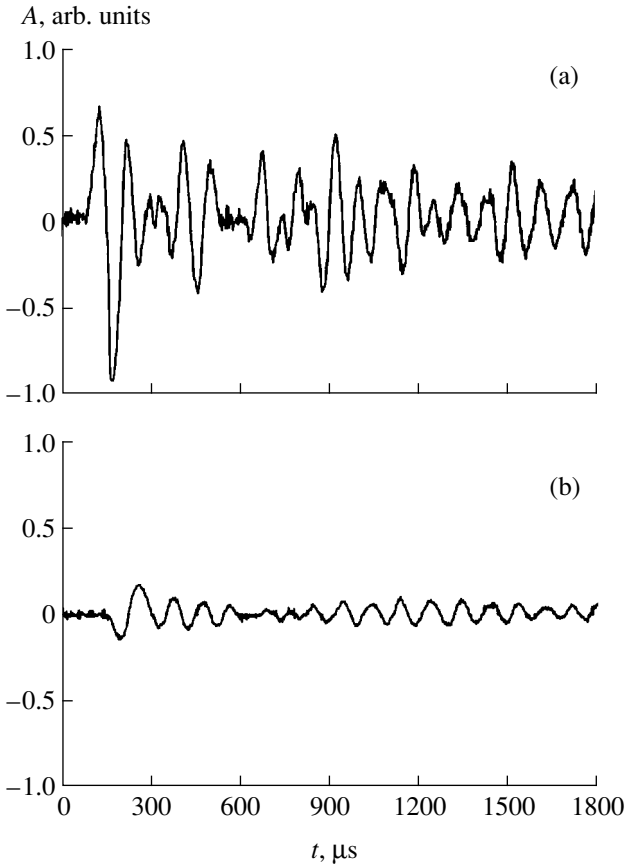

Fig. 2. Electromagnetic responses recorded during testing of cement samples with single inclusions of gravel grains sized (a) $35 \times 35 \times 20$ and (b) $12 \times 9 \times 6$ mm.

inclusions. As revealed by mathematical treatment, this dependence is described by the equation

$$A = k(-14.4 + 9.3S^{0.5}),$$

where A is the amplitude of electromagnetic response (in arbitrary units), S is the area of inclusion (mm^2), and k is the dimensionality factor (mm^{-2}).

Proceeding from this formula, one can use the extrapolation of the curve to zero amplitude values to estimate the minimum area of inclusion that leads to the appearance of a signal of electromagnetic emission detectable by our equipment: this area is 14.4 mm^2. As a result of these investigations, it becomes clear why no electromagnetic response is recorded in the case of cement stone: the sand in the cement stone composition is characterized by much smaller dimensions than 14.4 mm^2.

The obtained dependence of the amplitude of electromagnetic response on the interface area proves the fact of decisive importance of these boundaries, at least in the case of the formation of a pulsed electromagnetic signal. The electromagnetic emission generation may be associated with variation of the dipole moment of the electric double layer at the interface between matrix and inclusion during the shock wave propagation through the sample. The surface energy and the surface of electric double layer are proportional to the area (S). On the other hand, the signal energy is proportional to the square of amplitude (A^2); therefore, the dependence $A \approx S^{0.5}$ may serve an argument in favor of the adhesion mechanism of electromagnetic emission upon shock excitation of multicomponent heterogeneous materials consisting of a cement base and an inclusion.

The results obtained in model samples consisting of a cement base and artificial inclusions were checked in model samples of concrete in which single grains of gravel of different size were placed. Figure 2 shows the oscillograms of electromagnetic response recorded during testing of cement samples with inclusions of gravel grains of substantially different size. It is demonstrated that an increase in the amplitude of electromagnetic response is observed with increasing gravel grain size. Estimates of the correlation between the surface area of gravel grains and the amplitude of electromagnetic response from the model samples in which these grains are included fit the same dependence $A \approx S^{0.5}$.

The investigation results indicate that the efficiency of mechanoelectrical transformations in concretes increases with the size of inclusion. It is demonstrated that, when the area of inclusion is less than 14.4 mm^2, the efficiency of mechanoelectrical transformations in concretes is zero, at least, for the sensitivity of the recording equipment employed. The obtained correlation between the amplitude of electromagnetic response and the surface area of inclusion points to the mechanism of generation of electromagnetic emission by the electric double layer at the boundary between cement matrix and filler.

REFERENCES

1. Yu. P. Malyshkov, T. V. Fursa, V. F. Gordeev, *et al.*, Izv. Vyssh. Uchebn. Zaved., Stroit., No. 12, 31 (1996).
2. T. V. Fursa, V. V. Lasukov, Yu. P. Malyshkov, *et al.*, Izv. Vyssh. Uchebn. Zaved., Stroit., No. 10 (1997).
3. T. V. Fursa, N. N. Khorsov, and E. A. Baturin, Zh. Tekh. Fiz., No. 10 (1999) [Tech. Phys. **44**, 1175 (1999)].
4. V. F. Gordeev, V. P. Eliseev, Yu. P. Malyshkov, *et al.*, Defektoskopiya, No. 4, 48 (1994).

Translated by H. Bronsteĭn

Technical Physics Letters, Vol. 26, No. 2, 2000, pp. 107–108. Translated from Pis'ma v Zhurnal Tekhnicheskoĭ Fiziki, Vol. 26, No. 3, 2000, pp. 35–37.

Exoelectron Emission from $LiIO_3$ Crystals

N. A. Zakharov*, V. A. Klyuev*, Yu. P. Toporov, and T. V. Zakharova****

** Kurnakov Institute of General and Inorganic Chemistry, Russian Academy of Sciences, Leninskiĭ pr. 31, Moscow, 117907 Russia*

*** Institute of Physical Chemistry, Russian Academy of Sciences, Leninskiĭ pr. 31, Moscow, 117915 Russia*

Received May 11, 1999

Abstract—Thermostimulated exoelectron emission from $LiIO_3$ crystals in the temperature interval from 20 to 500°C was studied. Relationships between the character of emission and the composition, crystal structure, and sample preparation features are established. © *2000 MAIK "Nauka/Interperiodica".*

Below we report on the results of investigation of the effect of thermostimulated exoelectron emission (TSEE) from $LiIO_3$ crystals applied in various fields of technology [1]. The importance of this study was explained by significant dependence of the properties of $LiIO_3$ crystals on the method and conditions of sample crystal growth and the post-growth processing [2–4]. The method of TSEE measurements was selected for the study of $LiIO_3$ crystals because this effect is known to be highly sensitive to changes in the structure of samples and showed good results when used for the investigation of phase transitions in ferroelectrics [5] and biocompatible materials [6].

The experiments were performed on $LiIO_3$ crystals grown from an aqueous solution by the evaporation technique [2], representing a hexagonal α-$LiIO_3$ phase with the unit cell parameters $a = 5.48$ Å, $b = 5.17$ Å and the space group $P6_3$. The TSEE effect was studied on predominantly *c*-cut crystal plates. The measurements were carried out in the temperature interval from 20 to 500°C using a procedure described elsewhere [5]. The emission was activated by exposing samples to a field of corona discharge.

Heating the samples in the course of TSEE measurements was accompanied by the appearance of several peaks in the curve of TSEE intensity versus temperature. All the samples studied in this work exhibited a comparatively weak and broad maximum in the region of 200°C, followed by the peaks of greater intensity at about 250 and 300°C (see figure). It should be noted that the shape and position of the first maximum (200°C) exhibited rather insignificant variations, irrespective of the conditions of an α-$LiIO_3$ crystal preparation and the single crystal region from which a particular sample was cut. At the same time, the positions of maxima peaked at 250 and 290°C varied within the temperature intervals 200–250 and 220–300°C, respectively.

The behavior of the latter peaks agrees with the results of DTA and DTG measurements [1], according to which the pattern of polymorphous transitions in $LiIO_3$ can be described by the following scheme:

$$\alpha \xleftarrow{247^\circ C} \gamma \underset{390^\circ C}{\overset{285^\circ C}{\rightleftarrows}} \beta \xrightarrow{435^\circ C} \text{Liquid}.$$

Thus, the intense TSEE peaks observed in the region of 250 and 290°C (see figure) correspond to the structural transitions of $LiIO_3$ from α to γ and β phases, respectively. Note that the temperature-induced transition to the β-$LiIO_3$ phase involves a crystal reconstruction [1] resulting in breakage of the sample. The corresponding TSEE peak (see figure) is typical of the emission accompanying the phenomenon of mechanodestruction in crystals [7]. These structural transitions are accompanied, as noted above, by anomalous variation of the physical characteristics such as the dielectric permittivity, piezoelectric moduli, and electromechanical coupling coefficients [2–4]. A lack of reproducibility in the measured temperatures of polymorphous transitions is probably explained, as

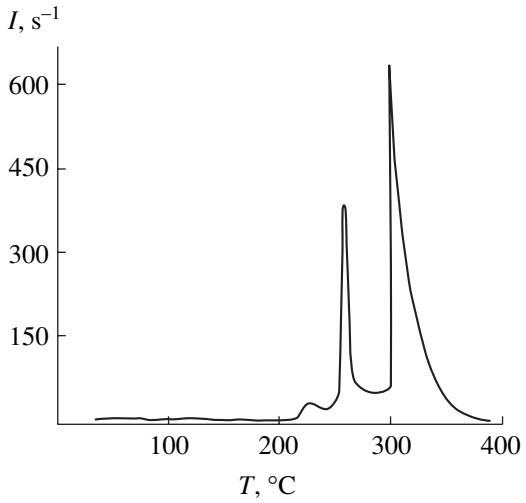

A typical glow curve of a $LiIO_3$ crystal, representing the TSEE current intensity variation during heating of a sample.

1063-7850/00/2602-0107$20.00 © 2000 MAIK "Nauka/Interperiodica"

indicated in [2], by variations in the composition and quality of the crystals studied.

The TSEE feature observed at 200°C can be assigned to an increase in proportion of the γ-$LiIO_3$ phase in the bulk of the crystal [4]. The appearance of this phase is related to the separation of a $Li_xH_{1-x}IO_3$ solid solution in the region of inclusions of a α-$LiIO_3$ crystal phase growing from an acid (pH 2) solution and the melting of HIO_3 phase (T_m = 110°C). Important information on the course of these processes can probably be extracted from the character of anomalies in the properties of $LiIO_3$ crystals in the region of 200°C. However, this would require additional investigations, which will be reported in our subsequent publications.

Thus, the results of our study of the thermostimulated exoelectron emission from $LiIO_3$ crystals indicate that the TSEE measurements offer an effective means of monitoring properties of the crystals in the course of their preparation and use. This method significantly supplements the other physical techniques (including the X-ray diffraction) used for the investigation of properties and the monitoring of quality of the $LiIO_3$ crystals.

REFERENCES

1. *Lithium Iodate Crystals: Growth, Properties, and Applications*, Ed. by S. V. Bogdanov (Nauka, Novosibirsk, 1982).
2. N. A. Zakharov, A. V. Egorov, N. S. Kozlova, *et al*., Zh. Tekh. Fiz. **60**, 165 (1990).
3. N. A. Zakharov, N. S. Kozlova, V. N. Nosov, *et al*., Neorg. Mater. **26**, 2437 (1990).
4. N. A. Zakharov, A. V. Egorov, N. S. Kozlova, *et al*., Fiz. Tverd. Tela (Leningrad) **30**, 3166 (1988).
5. N. A. Zakharov, V. A. Klyuev, Yu. P. Toporov, *et al*., Neorg. Mater. **31**, 1100 (1995).
6. V. P. Orlovskiĭ, N. A. Zakharov, V. A. Klyuev, *et al.*, Neorg. Mater. **31**, 1103 (1995).
7. Yu. V. Deryagin, N. A. Krotova, and V. P. Smilga, *Adhesion of Solids* (Nauka, Moscow, 1973).

Translated by P.P. Pozdeev

Technical Physics Letters, Vol. 26, No. 2, 2000, pp. 109–111. Translated from Pis'ma v Zhurnal Tekhnicheskoĭ Fiziki, Vol. 26, No. 3, 2000, pp. 38–43.

Detection of Nitrogen Dioxide by Amorphous Films of Tungsten Trioxide

E. A. Tutov, S. V. Ryabtsev, and A. Yu. Andryukov

Voronezh State University, Voronezh, 394893 Russia

Received May 26, 1999

Abstract—Data are given about the good "sensor" properties of amorphous tungsten trioxide with respect to NO_2 adsorption. The resistance of WO_3 film varies appreciably due to the binding of semiconductor electrons by NO_2 molecules. *© 2000 MAIK "Nauka/Interperiodica".*

Nitrogen oxides NO_x form one of the most toxic components of industrial emissions and exhaust gases of transport vehicles. In solving the problem of monitoring the concentration of nitrogen oxides in the atmosphere, metal-oxide semiconductor gas sensors present an alternative to chemiluminescent techniques.

Amorphous films of tungsten trioxide (a-WO_3) are characterized by high porosity. The developed internal surface of WO_3 provides for the possibility of diverse functional applications of this material and related structures, in particular, in physical and chemical sensors [1, 2]. The reversible formation of H_xWO_3 hydrogen–tungsten bronzes under conditions of dissociative absorption of hydrogen, ammonia, and alcohols is the basis of the bulk mechanism of sensitivity of this material with respect to donor gases [3]. On the contrary, acceptor gases (except for oxygen) are characterized by the surface mechanism of interaction with WO_3. In this case, the greatest expectations are associated with a high sensitivity of tungsten trioxide to nitrogen oxides [4], although this process has not been investigated for amorphous films.

The amorphous films of tungsten trioxide for our experiments were prepared by vacuum condensation of a thermally evaporated WO_3 powder onto a dielectric substrate provided with a platinum heater and a thermoresistive transducer for setting and monitoring the desired sensor temperature. The film was 50–500 nm thick, with a characteristic microcrystallite size of about 1 nm. Depending on the conditions of the condensation process, one can prepare the WO_3 layers of different degrees of structure ordering and anion deficiency [5–7]. By varying these conditions (in particular, the substrate temperature), one can control the size of the active surface of the film and, consequently, the sensitivity of its electric conductivity with respect to adsorbed gas molecules (NO_2). The concentration of NO_2 in a flow of air was varied within 0–6 ppm, and the sensor temperature ranged from 300 to 600 K.

The mechanism of interaction between NO_2 and a-WO_3 is typical of that between acceptor gas and

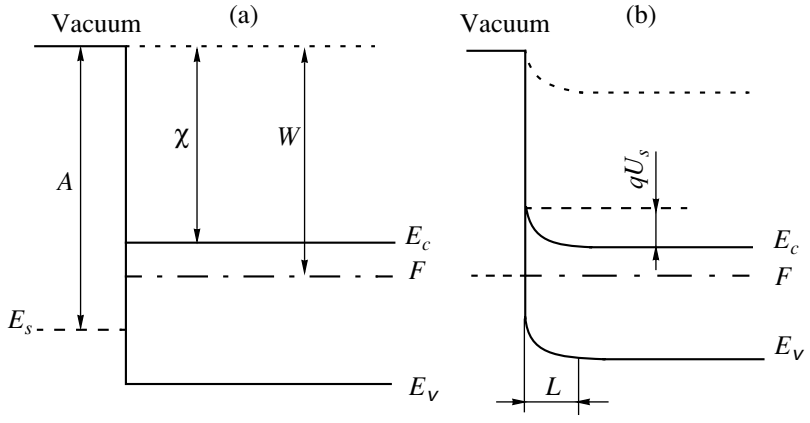

Fig. 1. The state of a-WO_3 surface (a) prior to and (b) after the chemisorption of acceptor molecules of NO_2: A, affinity of NO_2 molecule for electron; χ, affinity of WO_3 for electron; W, electron work function of WO_3; F, Fermi level; E_s, adsorption level; E_c, bottom of the conduction band; E_v, top of the valence band; U_s, magnitude of the potential barrier; L, width of the depleted region.

1063-7850/00/2602-0109$20.00 © 2000 MAIK "Nauka/Interperiodica"

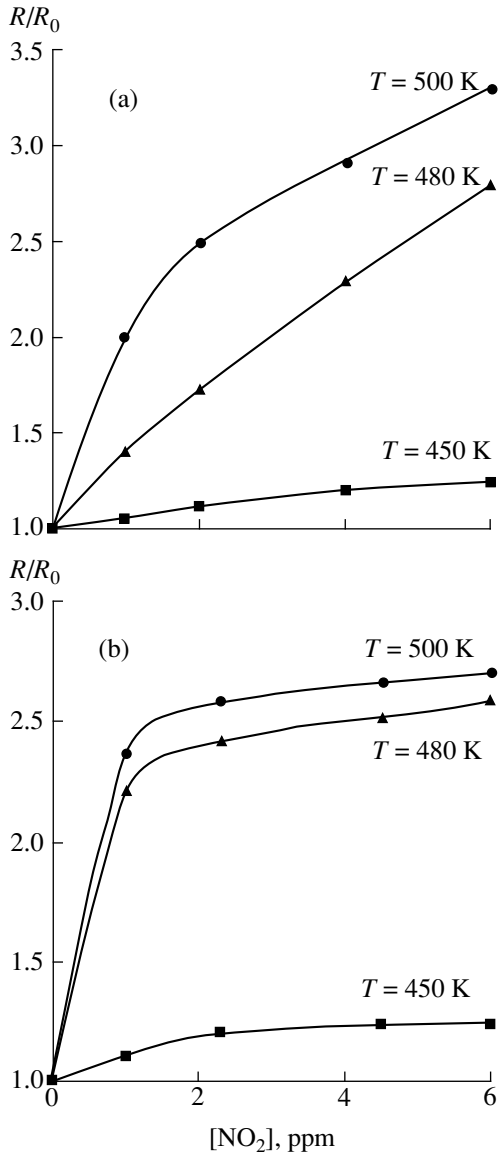

Fig. 2. The concentration dependence of the sensor response to NO_2 for different values of the working temperature: (a) for a film of *a*-WO_3 condensed on unheated substrate; (b) for a film of *a*-WO_3 condensed at the substrate temperature of 600 K.

n-type semiconductor [8]; the *n*-type conductivity in tungsten trioxide is due to the polyvalence of tungsten cation and nonstoichiometry of the film composition. The W^{5+} and W^{4+} ions with one or two excess electrons, respectively, are donors in the W^{6+} lattice,

$$W^{5+} \longrightarrow W^{6+} + e^-, \quad W^{4+} \longrightarrow W^{6+} + 2e^-.$$

When electronegative molecules of NO_2 (as well as of NO [9]) reach the semiconductor surface, they capture electrons from the conduction band and, thereby, are chemisorbed on the surface. On further adsorption, the surface is charged negatively, and a layer with relative positive charge is formed in the semiconductor bulk. As a result of adsorption, the energy levels of semiconductor bend upwards, and the surface layer is depleted of free carriers (Fig. 1).

The thickness L of the space charge region is related to the donor concentration N and the potential barrier height U_s by the expression $L = \sqrt{\frac{2\varepsilon\varepsilon_0 U_s}{qN}}$, where ε is the dielectric permittivity of semiconductor [8]. Because the semiconductor film has a significant resistance and a small thickness, the space charge region may involve the entire thickness of the sample, reaching the substrate. This is favored by high dielectric permittivity of tungsten trioxide [5] and, as a result, the film resistance must increase considerably. Analogous behavior is observed in SnO_2—another well-known *n*-type semiconductor widely studied as a nitrogen oxide sensor [10, 11].

Solis and Lantto [12] reported an anomalous conductivity buildup in tungsten trioxide in response to the NO adsorption; however, they provided no interpretation of their observations.

The relative variation of resistance of an *a*-WO_3 film as function of the NO_2 concentration for various sensor temperatures is given in Fig. 2. In the case of a tungsten trioxide film condensed at a substrate temperature of 600 K, the resistance increases by a factor of 2.5 to reach saturation at 2 ppm NO_2 in air (Fig. 2b). For more disordered films (Fig. 2a), the resistance increases by a factor of 3.5 showing no saturation even at 6 ppm NO_2. Note that the films of tungsten trioxide prepared (condensation and/or short-term annealing) at temperatures not exceeding 600 K, remain X-ray- and electron-amorphous [5]; however, the transition to a thermodynamically more stable state is undoubtedly accompanied with some structural ordering that is registered, in particular, by X-ray spectroscopy [6].

The optimum temperature of the sensor is 500 K. At lower temperatures, the sensitivity and kinetic characteristics of the sensor decrease, while at higher temperatures an active additional oxidation of nonstoichiometric tungsten trioxide with atmospheric oxygen is observed, which is accompanied by a sharp rise of the film resistance [3].

Unlike the bulk mechanism of the dissociation sorption of hydrogen and hydrogen-containing donor gases (NH_3, C_2H_5OH), which leads to emergence of the phase of hydrogen–tungsten bronze H_xWO_3 [3], the sorption of acceptor gas NO_2 obeys a surface mechanism, which is characterized by the saturation of sensitivity at a concentration of the order of 10 ppm [9]. This is indicative of the absence, at the temperatures studied, of mobile electrically active products of interaction between nitrogen dioxide and *a*-WO_3 film, which are capable of penetrating into the bulk of tungsten trioxide.

We have investigated the temperature and concentration dependences of the electric conductivity of amorphous films of tungsten trioxide under conditions of surface chemisorption of nitrogen dioxide. A sensor employing undoped films of *a*-WO_3 has demonstrated a reaction to NO_2 at a concentration on a level of several ppm and below at a temperature of 500 K. The possibility is demonstrated of controlling the sensor response by varying the degree of structural ordering in the *a*-WO_3 film.

REFERENCES

1. E. A. Tutov, A. A. Baev, S. V. Ryabtsev, *et al.*, Thin Solid Films **296**, 184 (1997).
2. E. A. Tutov, S. V. Ryabtsev, and E. N. Bormontov, Pis'ma Zh. Tekh. Fiz. **23**, 7 (1997) [Tech. Phys. Lett. **23** (6), 456 (1997)].
3. E. A. Tutov, S. V. Ryabtsev, A. Yu. Andryukov, *et al.* (submitted to Zh. Tekh. Fiz.).
4. M. Akiyama, J. Tamaki, N. Miura, *et al.*, Chem. Lett. **10**, 1611 (1991).
5. V. I. Kukuev, E. A. Tutov, É. P. Domashevskaya, *et al.*, Zh. Tekh. Fiz. **57**, 1957 (1987) [Sov. Phys. Tech. Phys. **32**, 1176 (1987)].
6. V. I. Kukuev, E. A. Tutov, M. V. Lesovoĭ, *et al.*, Poverkhnost' Fiz. Khim. Mekh., No. 11, 87 (1988).
7. E. A. Tutov, V. I. Kukuev, A. A. Baev, *et al.*, Zh. Tekh. Fiz. **65**, 117 (1995) [Tech. Phys. **40** (7), 697 (1995)].
8. A. I. Buturlin, T. A. Gabuzyan, N. A. Golovanov, *et al.*, Zarubezhn. Élektron. Tekh., No. 10, 3 (1983).
9. A. A. Tomchenko and V. V. Khatko, in *Proceedings of 11th European Conference on Solid State Transducers, Warsaw, Poland, 1997*, Vol. 1, 1P1.1, p. 79.
10. G. Williams and G. S. V. Goles, Sensors Actuat. B **1**, 349 (1993).
11. F. J. Gutierrez, L. Ares, J. I. Robla, *et al.*, Sensors Actuat. B **1**, 354 (1993).
12. J. L. Solis and V. Lantto, in *Proceedings of 11th European Conference on Solid State Transducers, Warsaw, Poland, 1997*, Vol. 1, 1P2.4, p. 199.

Translated by H. Bronsteĭn

Technical Physics Letters, Vol. 26, No. 2, 2000, pp. 112–114. Translated from Pis'ma v Zhurnal Tekhnicheskoĭ Fiziki, Vol. 26, No. 3, 2000, pp. 44–49.

Orientation Dependence of the Diffraction Efficiency of Holograms in Cubic Photorefractive (111)-Cut Piezocrystals

S. F. Nichiporko, A. E. Zagorskiĭ, V. V. Shepelevich, Yi. Hu, K. H. Ringhofer, and E. A. Shamonina

Mozyrsk State Pedagogical Institute, Belarus

Osnabruck University, Germany

Received August 19, 1999

Abstract—The diffraction efficiency of the transmission holograms in the photorefractive (111)-cut crystals of the classes $\bar{4}3m$ and 23 depends on the orientation of the lattice vector. This effect is determined by combined manifestation of the piezoelectric and photoelastic properties of the crystal. The shape of this dependence is determined both theoretically and experimentally for the fixed linear polarizations of the readout light waves in a 2.1-mm-thick (111)-cut $Bi_{12}SiO_{20}$ crystal (class 23). © *2000 MAIK "Nauka/Interperiodica".*

The interaction of light waves in cubic photorefractive (111)-cut crystals is extensively studied in recent years. In particular, Ding and Eichler [1] studied four- and two-wave interaction in (111)-cut InP and GaAs crystals (class $\bar{4}3m$). Eichler *et al.* [2] studied two-wave interaction in arbitrarily cut (including (111)-cut) crystals of the same class. Based on the results of theoretical and experimental studies of GaAs crystals, Sugg *et al.* [3] came to a conclusion that the diffraction efficiency of holograms in (111)-cut crystals of the class $\bar{4}3m$ does not depend on the orientation of the holographic grating vector in the shear plane, provided that the polarization direction of the recording waves (i.e., vector of the electric field strength **E**) is perpendicular to the plane of incidence. The reflection holographic gratings in (111)-cut $Bi_{12}TiO_{20}$ crystal (class 23) were studied in [4].

In all the above mentioned works, the diffraction processes were studied with neglect of the piezoelectric effect. However, this effect was observed in many crystals, including $Bi_{12}SiO_{20}$, $Bi_{12}TiO_{20}$, $Bi_{12}GeO_{20}$, GaAs, etc. (see, for example, [5–7]).

In a recent paper [8], we studied the influence of the piezoelectric effect on the orientation dependence of the amplification of the signal light beam in cubic photorefractive (111)-cut crystals in the case of two-wave interactions.

This work is aimed at the study of the orientation dependence of the diffraction efficiency of the transmission holograms recorded in cubic photorefractive (111)-cut crystals of the class 23 with regard to the piezoelectric properties and optical activity of these media. To our knowledge, this is the first attempt at the study of this relationship.

For calculations of the diffraction efficiency of holograms, we use the equations of coupled waves (see formulas (1), (2), and (8) in [9]) that are valid for an arbitrarily cut crystal. In the case of small Bragg angles $\varphi(\varphi < 5^\circ$, $\cos\varphi \approx 1$, $\sin\varphi \approx \tan\varphi \approx 0)$ in a (111)-cut crystal the coupling constants κ_i $(i = 1, 2, 3, 4)$ are given by approximate relationships:

$$\begin{aligned}
\kappa_1 &\approx -\kappa_0\{3(b_{11} + b_{22} - 2b_{12})\cos^2\theta \\
&+ [b_{11} + b_{22} + 2b_{12} + 4(b_{33} - b_{13} - b_{23})]\sin^2\theta \\
&+ \sqrt{3}[b_{11} - b_{22} + 2(b_{23} - b_{13})]\sin(2\theta)\}, \\
\kappa_2 \approx \kappa_3 &\approx -\kappa_0\{[-b_{11} - b_{22} + 2(b_{33} + 2b_{12} - b_{23} - b_{13})] \\
&\times \sin(2\theta) + \sqrt{3}(b_{11} - b_{22} + 2(b_{23} - b_{13}))\cos(2\theta)\}, \\
\kappa_4 &\approx -\kappa_0\{3(b_{11} + b_{22} - 2b_{12})\sin^2\theta \\
&+ [b_{11} + b_{22} + 2b_{12} + 4(b_{33} - b_{13} - b_{23})]\cos^2\theta \\
&+ \sqrt{3}[-b_{11} + b_{22} + 2(b_{13} - b_{23})]\sin(2\theta)\},
\end{aligned} \tag{1}$$

where θ is the orientation angle between the direction $[\bar{1}\bar{1}2]$ and the lattice vector **K**, $\kappa_0 = \pi n^3(12\lambda)^{-1}E_G$, n is the refractive index of the crystal, λ is the wavelength of the light beams, E_G is the amplitude of the electric field strength of the holographic grating. General expressions for the components of the inverse tensor of the dielectric permittivity b_{ij} can be found in [10].

Neglecting self-diffraction (the preset grating approximation) and assuming that the coupling constants are small ($\kappa_0 \ll \alpha$, where α is the specific optical rotation of the crystal in rad/mm), one can obtain analytical solution for the system of coupled equations and

an expression for the diffraction efficiency of the hologram:

$$\eta = a^2 + b^2 + c^2 + 2a\{b\cos(2\Psi_0 - \alpha d) + c\sin(2\Psi_0 - \alpha d)\}, \quad (2)$$

where

$$a = -\{(\kappa_1 + \kappa_4)/2\}d,$$

$$b = (\kappa_1 - \kappa_4)\{\sin(\alpha d)\}/(2\alpha),$$

$$c = \{\kappa_2 \sin(\alpha d)\}/\alpha,$$

d is the thickness of the crystal. Here we assume that the readout of the hologram is performed by a linearly polarized light with the polarization azimuth Ψ_0.

Based on more general expressions for the diffraction efficiency [9, 11], one can demonstrate that the formula (2) is also applicable to crystals of the class $\bar{4}3m$ by assuming that $\sin(\alpha d)/(\alpha d) = 1$, $\alpha = 0$ and taking into account that the photoelastic parameters p_2 and p_3 coincide in the crystals of these classes.

An analysis of expression (2) shows that, in the case of absence of the piezoelectric effect, $a = 0$, $b^2 + c^2 =$ const and, therefore, the diffraction efficiency does not depend on the orientation angle θ for the crystals of both classes (23 and $\bar{4}3m$), which is in agreement with the results reported in [3]. However, an allowance of this effect in real piezocrystals of these classes leads to dependence of the parameters a and $b^2 + c^2$ on θ. Thus, the variation of the diffraction efficiency of holograms in a wide range can be achieved by means of variation of the sample orientation and the polarization of the readout light beam.

Figure 1 shows the theoretical curves of the diffraction efficiency of hologram η versus the orientation angle θ for various fixed polarizations of the readout light for a 2.1-mm-thick (111)-cut $Bi_{12}SiO_{20}$ crystal. The diffraction efficiency was calculated for the amplitude of the electric field strength of the holographic grating $E_G = 0.458$ kV/cm. As seen (curves *1–5*), the diffraction efficiency does not depend on polarization of the readout light only for the fixed values of the orientation angle $\theta = 30° + k \times 60°$, where k is an integer. It can be easily demonstrated that the maximum values of the diffraction efficiency are achieved for the angles $\theta = k \times 60°$ (curve 6).

For verification of the theoretical curves we have experimentally studied the diffraction of light waves in a 2.1-mm-thick (111)-cut $Bi_{12}SiO_{20}$ crystal.

A light beam from a He–Ne laser with a power of 50 mW was split into two beams with the ratio of intensities 1 : 2.1. These beams were incident on the crystal at the Bragg angle in air $\varphi_0 \approx 11.5°$ (which corresponds to $\varphi \approx 4.5°$). A semiconductor diode with current amplifier was used for measurements of the diffracted light intensity. Polarization of the laser beam was varied by

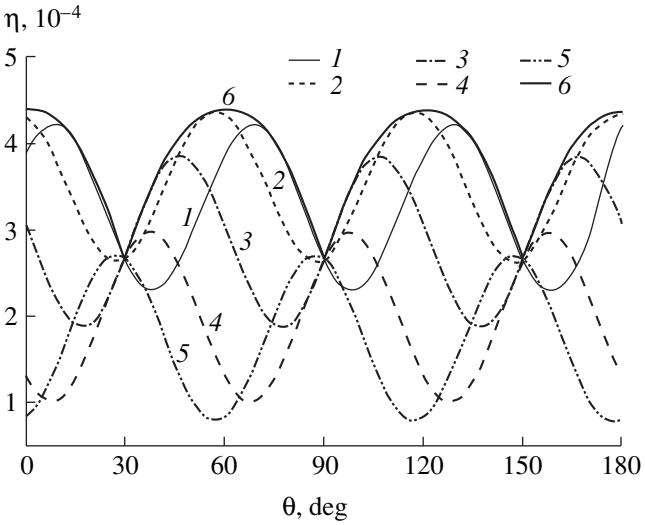

Fig. 1. Theoretical curves of the diffraction efficiency η of the holographic grating in $Bi_{12}SiO_{20}$ crystal versus the orientation angle θ: (*1*) $\Psi_0 = 0$; (*2*) $\Psi_0 = 30°$; (*3*) $\Psi_0 = 60°$; (*4*) $\Psi_0 = 90°$; (*5*) $\Psi_0 = 120°$. Curve *6* shows the dependence of the maximal values of the diffraction efficiency, achieved due to the change of polarization of the readout light, on the orientation angle. The calculations were performed for the following values of parameters of the crystal (see, e.g., [11]): $n = 2.54$; electrooptical coefficient $r = -5 \times 10^{-12}$ m/V; components of the elasticity tensor $c_1 = 12.96 \times 10^{10}$ N/m, $c_2 = 2.99 \times 10^{10}$ N/m, $c_3 = 2.45 \times 10^{10}$ N/m; photorefractive constants $p_1 = -0.16$, $p_2 = -0.13$, $p_3 = -0.12$, $p_4 = -0.015$; piezoelectric coefficient $e = 1.12$ C/m^3, $\lambda = 6.328 \times 10^{-7}$ m. Specific optical rotation $\alpha = 0.38$ rad/mm was measured for the sample under study.

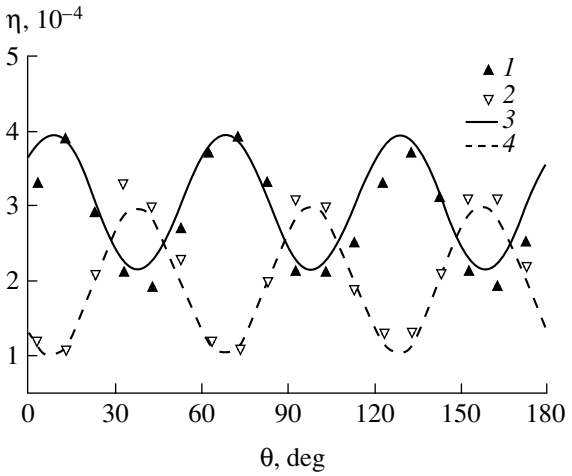

Fig. 2. Comparison of the experimental and theoretical curves of the diffraction efficiency for the readout light polarized in the plane of incidence ($\Psi_0 = 0$) and perpendicularly to this plane ($\Psi_0 = 90°$): (*1*, *2*) experimental curves $\eta(\theta)$ for (*1*) $\Psi_0 = 0$ and (*2*) $\Psi_0 = 90°$; (*3*, *4*) theoretical curves $\eta(\theta)$ for (*3*) $\Psi_0 = 0$ and (*4*) $\Psi_0 = 90°$. Here we take into account a certain decrease of the visibility of the holographic grating and the value of E_G for $\Psi_0 = 0$ due to noncollinearity of vectors of the electric field strength for the incident waves that record the holograms.

means of a quarter-wave retardation plate and a polarizer.

The holographic grating was recorded during 30 s. After that, one of the beams was cut off and the measurements of the ratio of intensities of the diffracted and readout beams were performed.

Experimental curves of $\eta(\theta)$ for the polarizations of the light beams $\Psi_0 = 0(\blacktriangle)$ and $\Psi_0 = 90°(\triangledown)$ are presented in Fig. 2. The best agreement between theoretical and experimental curves is achieved for E_G = 0.458 kV/cm.

Reasonable agreement between the experimental and theoretical orientation dependences proves that the above approximations and the proposed phenomenological model comply with the real diffraction process.

ACKNOWLEDGMENTS

The authors are grateful to M. V. Shamonin, V. P. Kamenev, N. N. Egorov, and A. A. Firsov for the helpful discussion of the results.

This work was supported in part by grants from the Foundation for Basic Research of the Republic of Belarus, Ministry of Education of Belarus, and the Board on Education of the Post-Graduate Students of Osnabruck University.

REFERENCES

1. Y. Ding and H. J. Eĭchler, Opt. Commun. **110**, 446 (1994).
2. H. J. Eĭchler, Y. Ding, and B. Smandek, Phys. Rev. A: Gen. Phys. **52**, 2411 (1995).
3. B. Sugg, F. Kahman, R. A. Rupp, *et al.*, Opt. Commun. **106**, 6 (1993).
4. N. Kukhtarev, B. S. Chen, P. Venkateswarlu, *et al.*, Opt. Commun. **104**, 23 (1993).
5. S. I. Stepanov, S. M. Shandarov, and N. D. Khat'kov, Fiz. Tverd. Tela **24**, 3054 (1987).
6. L. Solymar, D. I. Webb, and A. Grunnet-Jepsen, *The Physics and Applications of Photorefractive Materials* (Clarendon Press, Oxford, 1996), pp. 226–230.
7. E. Shamonina, V. P. Kamenov, K. H. Ringhofer, *et al.*, J. Opt. Soc. Am. B **15**, 2552 (1998).
8. V. V. Shepelevich, S. F. Nichiporko, A. E. Zagorskiy, *et al.*, OSA Trends Optics Photonics **27**, 353 (1999).
9. V. V. Shepelevich, Opt. Spektrosk. **83**, 172 (1997).
10. S. M. Shandarov, V. V. Shepelevich, and N. D. Khat'kov, Opt. Spektrosk. **70**, 1068 (1991).
11. V. V. Shepelevich, S. M. Shandarov, and A. E. Mandel, Ferroelectrics **110**, 235 (1990).

Translated by A. Chikishev

Technical Physics Letters, Vol. 26, No. 2, 2000, pp. 115–118. Translated from Pis'ma v Zhurnal Tekhnicheskoĭ Fiziki, Vol. 26, No. 3, 2000, pp. 50–59.

Equilibrium Magnetization State of Magnetic Composites

S. O. Gladkov

Semenov Institute of Chemical Physics, Russian Academy of Sciences, ul. Kosygina 4, Moscow, 117977 Russia

Received April 20, 1999

Abstract—Based on the general thermodynamic principles, a stable equilibrium state of magnetization is found in a composite consisting of a ferromagnetic matrix and a finely dispersed magnetic impurity. It is demonstrated that this state is energetically less beneficial than the analogous state in a homogeneous (one-component) substance. © *2000 MAIK "Nauka/Interperiodica".*

Prior to investigation of some nonequilibrium properties of a magnetic structure, it is usually necessary to establish the stable ground state of the given magnetic configuration [1, 2]. Once this state is known (which, in the case of magnetic atoms, is equivalent to a certain geometric orientation of the magnetization components), one can readily solve particular physical problems, for example, (a) describe the establishment of thermodynamic equilibrium in a given structure, (b) reveal the features of absorption of the energy of a radio-frequency field, and (c) find the decrement of sound waves in these substances, etc. (see, e.g., [3–5]).

Because magnetic composites are not exempted from the general rule, an adequate description of their nonequilibrium properties requires preliminary determination of the ground equilibrium configuration of spins at $T = 0$, when ferromagnetic particles play the part of filler. This communication presents the results of calculation of the ground state energy in the case when the particles have a spherical shape, and the external magnetic field **H** is absent. This case is interesting in that there is nothing that could cause all magnetic moments to orient strictly along the field direction and, therefore, we may analyze the natural geometric orientation of spins in a given substance at $T = 0$, when their arrangement is determined only by the spin-orbit effects.

Let β_0 and β_1 be the anisotropy constants in the base matrix (phase "0") and in the impurity structure (phase "1"), respectively. Because the interaction between phases occurs according to the mechanism of dipole–dipole coupling, a general expression for the system Hamiltonian must be written in the following form:

$$H = -V(1-x)\beta_0 M_{0z}^2 + \beta_1 V^{-1}\sum_{j=1}^{\nu} v_{1j} M_{1jz'}^2$$

$$-\sum_{j=1}^{\nu}(\delta V_j/R_j)\{3\mathbf{M}_0\mathbf{M}_{1j} - (\mathbf{M}_0\mathbf{d}_j)(\mathbf{M}_{1j}\mathbf{d}_j)/d_j^2\} \quad (1)$$

$$-V^{-1}\sum_{j=1}^{\nu}\mathbf{H}_1\mathbf{M}_{1j}dV,$$

where $x = V_1/V$, $V_1 = \nu v_1$ is the average volume of particles of the finely dispersed phase, ν is the number of particles, v_{1j} is the volume of a single particle, $V = V_0 + V_1$ is the composite volume, V_0 is the base matrix volume, R_j is the radius of the jth particle, d_j is the distance between an atom of the matrix and an atom of the ferromagnetic impurity particle occurring at the interface (Fig. 1), $\delta V_j = d_j S_j$ is the interface volume, $S_j = 4\pi R_j^2$, and the axis z_j forms an angle α_j with the axis z (Fig. 2).

Because the external magnetic field is absent ($H = 0$), the magnetic induction in the matrix is $\mathbf{B}_0 = 4\pi\mathbf{M}_0$, where $\mathbf{M}_0$ is the spontaneous magnetization. Therefore, the role of an external field for the finely dispersed phase will be played by $\mathbf{B}_0$; this means that the

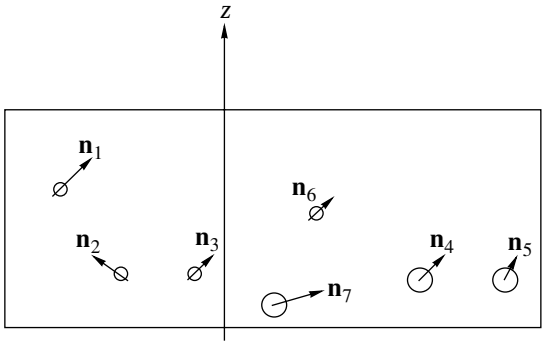

Fig. 1. Schematic diagram showing orientations of the axes of anisotropy for a system of particles of a finely dispersed ferromagnetic phase; $z = \mathbf{n}_0$ is the axis of anisotropy of the ground matrix. The circles indicate the regions of contact of the finely dispersed phase with the magnetic matrix.

1063-7850/00/2602-0115$20.00 © 2000 MAIK "Nauka/Interperiodica"

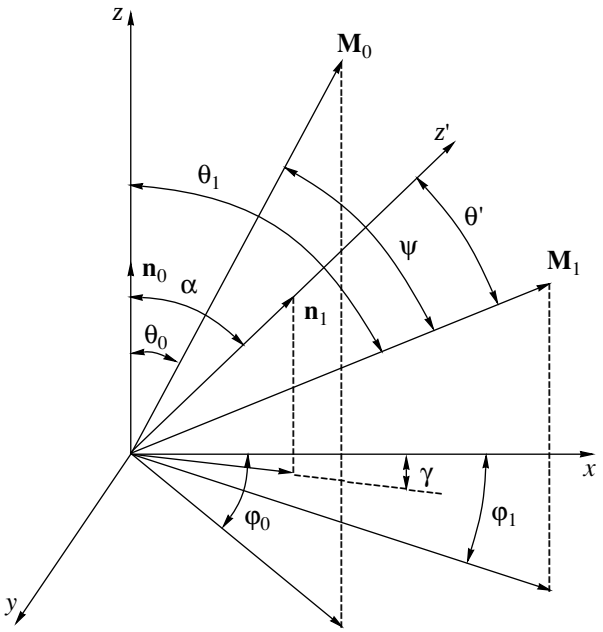

Fig. 2. Geometry of an arbitrary arrangement of magnetic moments in the presence of a single ferromagnetic particle ($\nu = 1$). All of the marked angles are found from the condition of minimum energy of the system phase "0" + phase "1" + interaction between them.

internal field in the particle is $\mathbf{H}_1^{(i)} = \mathbf{B}_0 - 4\pi N_1 \mathbf{M}_1 = \mathbf{B}_0 - 4\pi N_1 \chi_1 \mathbf{H}^{(i)}$, because $\mathbf{M}_1 = \chi_1 \mathbf{H}_0^{(i)}$. Consequently,

$$\mathbf{H}_1^{(i)} = \frac{4\pi \mathbf{M}_0}{1 + 4\pi N_1 \chi_1}. \tag{2a}$$

As for the induction $\mathbf{B}_1$, we obtain

$$\begin{aligned} \mathbf{B}_1 &= \mathbf{H}_1^{(i)} + 4\pi \mathbf{M}_1^{(i)} + 4\pi \mathbf{M}_1 \\ &= \mu_1 \mathbf{H}_1^{(i)} + 4\pi \mathbf{M}_1 = 4\pi \mathbf{M}_1 + \frac{4\pi \mu_1 \mathbf{M}_1}{1 + 4\pi N_1 \chi_1}, \end{aligned} \tag{2b}$$

where $\mathbf{M}_1$ is the spontaneous magnetization in a particle of the finely dispersed phase; χ_0 is the magnetic susceptibility of the matrix, and χ_1 is that of the impurity structure; N_1 denotes the demagnetization coefficients for particles of the impurity phase; and μ_1 is their magnetic permeability.

The distance d_j is assumed to be constant for each jth magnetic atom lying in the surface layer. Because $\delta V_j = a_1^2 d_j N_s$, where $N_s = 8\pi R_j / a_1^2$ is the total number of atoms in the surface layer (the factor 8π appears instead of 4π because these atoms are located on both sides of the interface), a_1 is the interatomic distance in phase "1." Therefore, $\delta V_j = 3 d_j \nu_{1j} / R_j$.

The substitution of expression (2a) into Hamiltonian (1) gives

$$\begin{aligned} H &= -V(1-x)\beta_0 M_{0z}^2 + \beta_1 V^{-1} \sum_{j=1}^{\nu} \nu_{1j} M_{1jz}^2 \\ &- \sum_{j=1}^{\nu} (\delta V_j / R_j) \{ 3 \mathbf{M}_0 \mathbf{M}_{1j} - (\mathbf{M}_0 \mathbf{d}_j)(\mathbf{M}_{1j} \mathbf{d}_j) / d_j^2 \} \\ &- 4\pi \sum_{j=1}^{\nu} \frac{\mathbf{M}_0 \mathbf{M}_{1j} \nu_j}{V(1 + 4\pi N_1 \chi_1)}. \end{aligned} \tag{3}$$

Obviously (this is verified by calculation), the minimum value of Hamiltonian (3) will be attained only in the case of a coplanar arrangement of all $\nu + 1$ vectors. We will refer to such plane as the *G*-plane. In addition, because the vector $\mathbf{d}_j$ coincides in direction with a vector normal to the surface of each jth ferromagnetic particle, the third term in expression (3), which is proportional to the product $\mathbf{M}_{1j}\mathbf{d}_j$, gives zero as a result of integration over all angles ψ ($\mathbf{M}_{1j}\mathbf{d}_j = M_{1j} d_j \cos\psi$). This means that

$$\begin{aligned} H = -V \Bigg\{ &(1-x)\beta_0 M_{0z}^2 + \beta_1 V^{-1} \sum_{j=1}^{\nu} \nu_{1j} M_{1jz}^2, \\ &- (9/V) \sum_{j=1}^{\nu} (d_j^* \nu_{1j} / R_j) \mathbf{M}_0 \mathbf{M}_{1j} \Bigg\}, \end{aligned} \tag{4}$$

where

$$d_j^* = d_j + 4\pi R_j / 9(1 + 4\pi N_1 \chi_1). \tag{4a}$$

In what follows, the asterisk in d_j^* will be omitted, but we will keep relation (4a) in mind. We introduce the angles θ_0 and θ_1 between the anisotropy axes z and z' and the vectors $\mathbf{M}_0$ and $\mathbf{M}_{1j}$, respectively, to derive

$$\begin{aligned} H = -V \Bigg\{ &(1-x)\beta_0 M_0^2 \cos^2\theta_0 \\ &+ \beta_1 V^{-1} \sum_{j=1}^{\nu} \nu_{1j} M_{1j}^2 \cos^2(\theta_{1j} - \alpha_j) \\ &- 3 M_0 M_1 \sum_{j=1}^{\nu} (d_j \nu_{1j} / R_j) \cos(\theta_0 - \theta_{1j}) \Bigg\}, \end{aligned} \tag{5}$$

where α_j is the angle between the anisotropy axes $\mathbf{n}_0$ and $\mathbf{n}_1$ (Fig. 1).

The conditions of extremum for the derived Hamiltonian with respect to the angles θ_0 and θ_1 yield the following set of equations:

$$\begin{cases} (1-x)\beta_0 M_0 \sin 2\theta_0 \\ -(3M_1/V)\sum_{j=1}^{\nu}(d_j \nu_{1j}/R_j)\sin(\theta_0-\theta_{1j}) = 0, \\ \beta_1 M_1 \sin 2(\theta_{1j}-\alpha_j) \\ +3(M_0 d_j \nu_{1j}/R_j)\sin(\theta_0-\theta_{1j}) = 0. \end{cases} \quad (6)$$

We will find a solution of the resultant set of equations in the case when $\nu = 1$ (a single ferromagnetic particle).

Introducing the parameters

$$\begin{cases} y = \cos\theta_1/\cos\theta_0, \\ z = \sin\theta_1/\sin\theta_0, \end{cases} \quad (7)$$

we obtain (for $\nu = 1$)

$$z - y + 2bk = 0, \quad (8a)$$

$$zy\cos 2\alpha + b + \sin 2\alpha[(z^2-y^2)/(1-y^2)^{1/2} - zy(1-y^2)^{1/2}]/(z^2-1)^{1/2} = 0, \quad (8b)$$

where

$$\begin{cases} b = (1-x)\beta_0 M_0^2/x\beta_1 M_1^2, \\ k = (R/3d)\beta_1 M_1/M_0, \\ x = \nu_1/V. \end{cases} \quad (9)$$

If the volume of a particle of the disperse ferromagnetic phase is small ($x \ll 1$), the solution of the set of equations (8) will be greatly simplified. Assuming that

$$\begin{cases} z = -2bk + \delta, \\ y = \delta, \end{cases}$$

we readily find that

$$\delta = \frac{1 + 2k\sin 2\alpha}{2k\cos 2\alpha}. \quad (10)$$

Solving the set of equations (7), we obtain

$$\begin{cases} \sin\theta_0 = -(4bk-\delta^2)^{1/2}/2bk, \\ \cos\theta_0 = (1-\delta/2bk), \end{cases} \quad (11)$$

$$\begin{cases} \sin\theta_0 = [1-\delta^2(1-\delta/2bk)^2]^{1/2}, \\ \cos\theta_0 = \delta(1-\delta/2bk). \end{cases} \quad (12)$$

Substitution of the resultant angles into initial Hamiltonian (5) with $\nu = 1$ yields

$$H_{\min} = -V\{(1-x)\beta_0 M_0^2(1-\delta/2bk) + x\beta_1 M_1^2[\delta\cos\alpha + (4bk-\delta^2)^{1/2}\sin\alpha]^2 - 9xd\delta M_0 M_1/R\}. \quad (13)$$

One can see from expression (13), in particular, that the additional phase "spoils" the ground state and increases (in proportion to the concentration x) the energy of the system (phase "0" + phase "1").

In order to take into account the ensemble of particles of the finely dispersed phase, one must integrate the second term in expression (13) over all angles α. This gives the following formula for the energy of the ground state of magnetic composite:

$$\langle H_{\min}\rangle = -V\{(1-x)\beta_0 M_0^2(1-\delta/2bk) + 4x\beta_1 M_1^2/3 - 9xd\delta M_0 M_1/\langle R\rangle\}. \quad (14)$$

Figure 3a demonstrates a geometry of the arrangement of magnetic moments in the case when the impurity phase is represented by a single particle ($\nu = 1$). In the case of an ensemble of particles, the arrangement of magnetic moments is illustrated schematically in Fig. 3b. Note once again that all spins in the equilibrium state are coplanar and oriented in the *G*-plane.

We will find a solution of the set of equations (6) in the case when the value of ν is large. Introducing a density of the volume distribution of particles for the finely dispersed magnetic phase $f(V)$ having a dimensionality

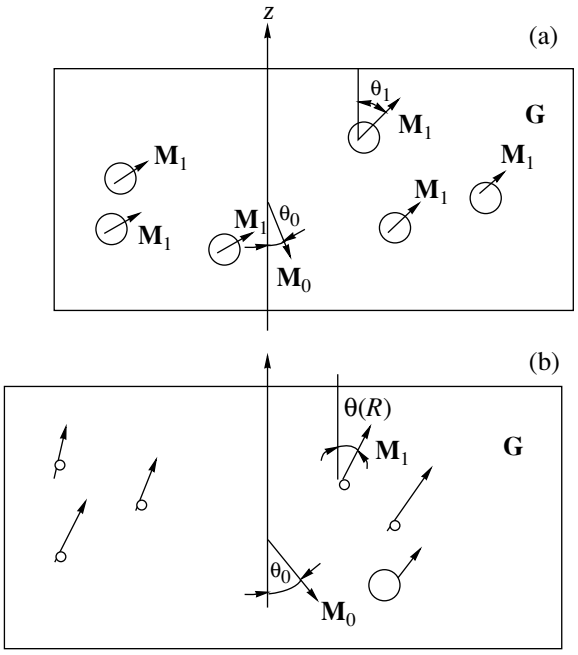

Fig. 3. Schematic diagrams showing (a) the equilibrium orientations of magnetic moments at $\nu = 1$ (for the corresponding values of parameters; see the text for comments) and (b) an equilibrium configuration of magnetic moments in the *G*-plane in the presence of an ensemble of finely dispersed particles.

of 1/cm^3, one can readily derive, on the condition that $d_j = d$ = const,

$$\begin{cases} b\sin 2\theta_0(v) \\ \quad - \int_0^v vf(v)\sin 2[\theta_0(v) - \alpha]dv/v_1 = 0, \end{cases} \quad (15a)$$

$$\begin{cases} k\sin 2[\theta_1(v) - \alpha] \\ \quad + \sin[\theta_0(v) - \theta_1(v)] = 0, \end{cases} \quad (15b)$$

where $\langle v_1 \rangle$ is some mean volume of particles of the impurity phase,

$$\begin{cases} k = k(R) = (R/3d)\beta_1 M_1/M_0, \\ b = \text{const} = [(1-x)/x](\beta_0/\beta_1)(M_0/M_1)^2. \end{cases} \quad (16)$$

In order to solve the resultant equations, we will use the approach described above. Indeed, differentiating equation (15a), with respect to v, taking into account equation (15b), and using parameters (16), we obtain

$$2kb\partial u/\partial v + (v/\langle v_1 \rangle)u(z-y)f(v) = 0, \quad (17)$$

where u is the new function defined as

$$u = [(z^2-1)(1-y^2)]^{1/2}/(z^2-y^2). \quad (18)$$

Assuming (as supported by the calculation results) that $u \longrightarrow 1/z$ and $z \gg y$, we readily find the solution

$$u = -\int_0^\infty vf(v)dv/2bk(R)\langle v_1 \rangle. \quad (19)$$

By virtue of rapid convergence of the integral, the upper limit of integration is taken equal to infinity. Let, for example, the normalized distribution function obey Poisson's law,

$$f(v) = (v/v_0)^m \exp\{-v/v_0\}/\langle v_1 \rangle \Gamma(m+1),$$

where $\Gamma(m)$ is the gamma function, $v = 4\pi R^3/3$, and v_0 is the distribution parameter.

Because $k = k_0 R = k_0(3v/4\pi)^{1/3}$ (where $k_0 = \beta_1 M_1/3dM_0$), we obtain from (19)

$$u = -(2bk)^{-1}(v_0/\langle v_1 \rangle)^2, \quad (20)$$

where $k = k_0(3v/4\pi)^{1/3}$.

The parameter z, as expected, is $z = -2bk(v_0/\langle v_1 \rangle)$ (see (18)). If we assume that an average value $\langle v_1 \rangle$ of the characteristic volume of particles of the finely dispersed phase coincides with the average value of $\langle v \rangle$ calculated by the distribution function $f\langle v \rangle$, then $\langle v_1 \rangle = (m+1)v_0$. Therefore, one can see that an allowance of the size distribution of particles affects very strongly the geometry of arrangement of the equilibrium magnetization in both phases. Therefore, this factor must be included in treating any dynamic effects in such structures (see [6]).

In the presence of P different additional impurity phases, the minimizing equations in this case will apparently contain one more additional index (g) characterizing the new phase. For this case, we obtain the following set instead of equations (6):

$$\begin{cases} (1-x)\beta_0 M_0 \sin 2\theta_0 \\ \quad - (3/V)\sum_{g=1}^{P} M_g \sum_{j=1}^{\nu_g} (d_j^{(g)} v_{1j}^{(g)}/R_j^{(g)})\sin(\theta_0 - \theta_{1j}^{(g)}) = 0, \\ \beta_g M_g R_j^{(g)} \sin 2(\theta_{1j}^{(g)} - \alpha_j^{(g)}) \\ \quad + 3M_0 d_j^{(g)} \sin(\theta_0 - \theta_{1j}^{(g)}) = 0. \end{cases}$$

This set of equations is quite analogous to equations (8).

In conclusion, note the following most important aspects:

1. We have determined a geometry of the orientation of spins in a composite at $T = 0$ in a system where both phases are ferromagnetic.

2. It is demonstrated that, from the energy standpoint, this orientation is not optimum as compared to a homogeneous (one-component) substance in which the corresponding energy is lower (see formula (14) at $x = 0$).

3. It is proved that an allowance for the scatter in the size of particles of a finely dispersed phase is important, because this factor may very strongly affect the ground state of the magnetic subsystem.

ACKNOWLEDGMENTS

This study was supported in part by the Russian Foundation for Basic Research (project no. 99-01-00011).

REFERENCES

1. A. I. Akhiezer, V. G. Bar'yakhtar, and S. V. Peletminskiĭ, *Spin Waves* (Nauka, Moscow, 1967).
2. S. V. Tyablikov, *Methods of Statistical Physics in the Theory of Magnetism* (Nauka, Moscow, 1974).
3. S. O. Gladkov, Phys. Rep. **182**, 211 (1989).
4. S. O. Gladkov, Zh. Éksp. Teor. Fiz. **83**, 806 (1982) [Sov. Phys. JETP **56**, 452 (1982)].
5. S. O. Gladkov, Fiz. Tverd. Tela **25**, 3502 (1983) [Sov. Phys. Solid State **25**, 2018 (1983)].
6. S. O. Gladkov, Fiz. Tverd. Tela **39**, 1622 (1997) [Phys. Solid State **39**, 1446 (1997)].

Translated by H. Bronsteĭn

Technical Physics Letters, Vol. 26, No. 2, 2000, pp. 119–121. Translated from Pis'ma v Zhurnal Tekhnicheskoĭ Fiziki, Vol. 26, No. 3, 2000, pp. 60–66.

Formation of Multiple Longitudinal High-Absorption Kinks under the Action of Collimated Gaussian Light Beams

A. V. Vysloukh and V. A. Trofimov

Moscow State University, Moscow, 119899 Russia

Received September 29, 1999

Abstract—The possibility of formation of several longitudinal kinks under the action of a collimated Gaussian light beam in a medium with absorptive cavityless optical bistability is demonstrated to be possible. The beam is essentially affected by diffraction. The domain formation is caused by the focusing of an annular beam into which the Gaussian beam is transformed due to nonlinear light absorption at small depths. © *2000 MAIK "Nauka/Interperiodica".*

Cavityless optical bistability has been studied most extensively in the case where the aperture of the light beam is so wide that diffraction can be neglected [1, 2]. However, the miniaturization of bistable elements calls for narrower beams, for which diffraction is considerable. Another reason for taking diffraction into account is that the characteristic size of a Gaussian incident beam is changed at the depths where a high-absorption domain is formed, since the intensity becomes, under certain conditions, smaller near the axis than in the peripheral region. The beam thus acquires an annular intensity profile, whose width must be regarded as the characteristic size of the beam. The diffraction length may therefore decrease several times against its input value. In addition, the intensity of an annular beam may rise in near-axial region. It should be pointed out that this property may cause the formation of additional high-absorption domains. However, this phenomenon has not been examined as yet. This study addresses the formation of multiple high-absorption domains in a semiconductor element possessing optical bistability. The bistability stems from increased absorption as a result of energy-gap renormalization due to the generation of free electrons. Note that similar effects may be common in optical media for data storage (three-dimensional memory).

Written in a dimensionless form, the underlying equations are as follows:

$$\frac{\partial A}{\partial z} + iD\Delta_\perp A + \frac{\delta_0}{2}\delta(n)A + i\alpha nA = 0, \quad 0 < z < L_z,$$
$$\frac{\partial n}{\partial t} = D_\perp\Delta_\perp n + D_\parallel\frac{\partial^2 n}{\partial z^2} + q|A|^2\delta(n) - n, \tag{1}$$

with the initial and the boundary conditions

$$n|_{t=0} = A|_{t=0} = r\frac{\partial A}{\partial r}\bigg|_{r=0} = A(z, t, r = R) = \frac{\partial n}{\partial z}\bigg|_{z=0, L_z} = \frac{\partial n}{\partial r}\bigg|_{r=0} = \frac{\partial n}{\partial r}\bigg|_{r=R} = 0, \tag{2}$$

and

$$A(z = 0, t, r) = \exp(-r^2/2)(1 - \exp(-10t)). \tag{3}$$

Here, A is the beam complex amplitude normalized to its input value; n is the density of free electrons in the conduction band, normalized to its maximum possible value (under the specified conditions); L_z is the length of the propagation path; r is the transverse coordinate normalized to the characteristic radius of the input beam profile; R is the maximum value of r; δ_0 characterizes the amount of light absorption over the diffraction length; $\delta(n)$ is the absorption coefficient as a nonlinear function of the free-electron density; α is the ratio of the input beam power to the characteristic self-action power; $\Delta_\perp = \frac{1}{r}\frac{\partial}{\partial r}\left(r\frac{\partial}{\partial r}\right)$ is the transverse Laplace operator, written in polar coordinates for an axially symmetric beam; q characterizes the rate of free-electron generation due to light absorption by the semiconductor; $D_\perp$ and $D_\parallel$ respectively characterize the transverse- and the longitudinal diffusion coefficients of charged particles; and t is time normalized to the relaxation time. The z coordinate is normalized to the diffraction length. Although $D = 1$ in this case, the parameter is left in equation (1) for the sake of convenience when conducting numerical experiments. Also note that we assume the excitation of the donor levels to be so weak that the relaxation time does not depend on the free-electron density.

1063-7850/00/2602-0119$20.00 © 2000 MAIK "Nauka/Interperiodica"

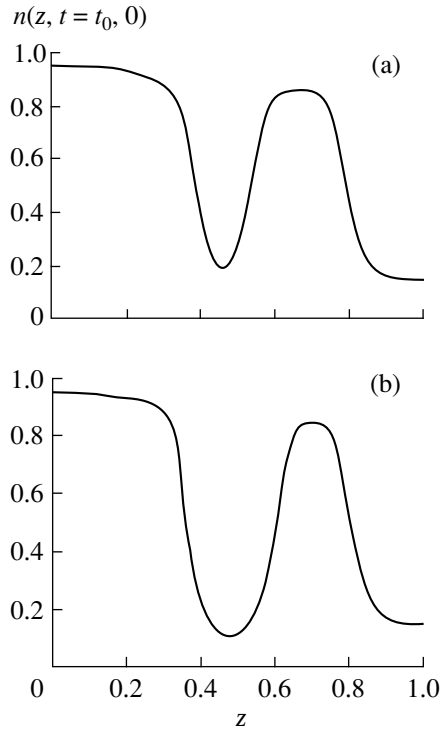

Fig. 1. The free-electron density distribution on the beam axis for (a) $D = 0.3$ or (b) $D = 0.27$ at $q = 2.25$, $D_{\|} = 0.001$, $D_{\perp} = 0.001$, $\delta_0 = 5.0$, $\alpha = 0$, and $t_0 = 75$.

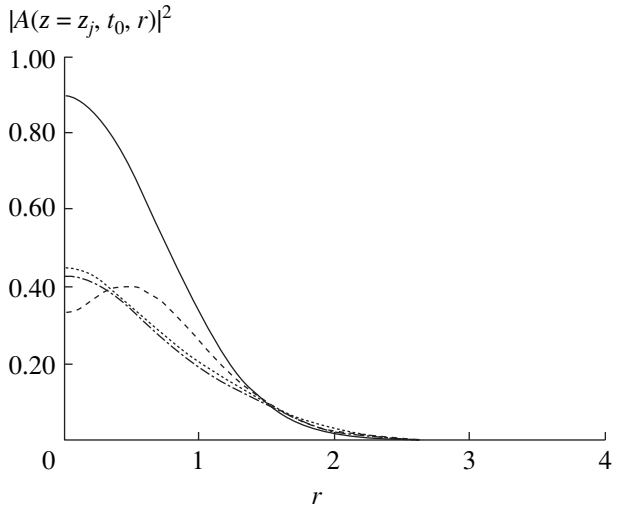

Fig. 2. Transverse intensity distribution at $z_j = 0$ (solid curve), $z_j = 0.44$ (dashed curve), $z_j = 0.78$ (dotted curve), or $z_j = 0.89$ (dot-and-dash curve). The values of parameters correspond to Fig. 1.

Let the absorption coefficient be approximated as

$$\delta(n) = (1 - n)\exp(-\gamma(1 - \beta n)) \qquad (4)$$

where $\alpha = 2.553$ and $\gamma\beta = 5$. Recall that, in the context of a lumped-parameter model, free-electron density as a function of input beam intensity is bistable if $\gamma\beta > 4$.

Figure 1 shows the steady-state distribution of n on the beam axis at two values of D. The curves are plotted for the case where longitudinal and transverse diffusion processes are developed only slightly (which is implemented, e.g., by an appropriate setting of the longitudinal size of the medium and the input beam size) and where amplitude-only gratings are dealt with (zero self-action). Note the existence of two domains, which can be attributed to the profile transformation with growing z. Figure 2 confirms the explanation by presenting beam-intensity profiles at various values of z.

Looking at Fig. 2, let us trace how the profile is transformed as z increases. At $z = 0$, we have a collimated Gaussian beam. Then the high-absorption domain near the beam axis produces a valley around $r = 0$ (see the dashed curve) so that the profile becomes annular. At a larger z, the Gaussian shape is recovered, owing to diffraction. The intensity now exceeds the switching threshold and the system goes to the upper state, where absorption is high (see the dotted curve). The increased absorption reduces the intensity, and the system returns to the lower state at a certain z. The flip-flop transition may occur again at larger z. Note that the position and the extent of the second domain (Fig. 1) can be controlled by varying the input radius of the beam (specifically, the D parameter)

The presence of self-action caused by phase gratings is indicated by the condition $\alpha \neq 0$. (Self-action can be implemented by detuning the frequency of the laser radiation from that of the transition.) The effect transforms the multidomain structure, but does not destroy it if the conditions are favorable. Figure 3 shows the distributions of n along the z-axis for three values of α. The nonzero values correspond to the case of amplitude–phase gratings (see the dashed and the dotted curve). The distribution for $\alpha = 0$ (the solid curve) is depicted for comparison. The figure indicates that self-focusing (represented by the dotted curve) changes the z value at which the system switches to the lower state, for the second domain, but does not affect the z value at which the transition to the upper state occurs. This testifies to the fact that intensity growth in the bulk of the medium primarily stems from the focusing governed by the annular profile of the beam. The defocusing of the beam lowers its maximum intensity, thus reducing the length of the domain. It also makes the annular property less pronounced so that the second transition to the upper state occurs at a larger z as compared to the case of zero self-action. It should be pointed out that the formation of a high-absorption domain causes a rapid variation of n along the r-axis in a certain region of z values. Furthermore, the lateral size of the second domain is much smaller than the beam radius, which leads to a strong lens effect if α is nonzero. This consideration determined the choice of the α values for Fig. 3.

To sum up, this study showed that diffraction fundamentally changes the formation of high-absorption

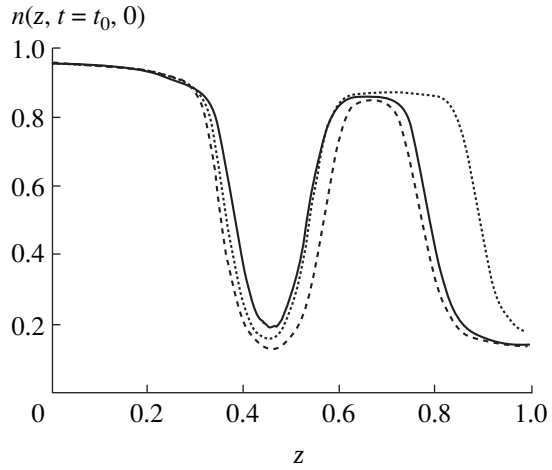

Fig. 3. Free-electron density distribution on the beam axis for $\alpha = 0.0$ (solid curve), $\alpha = -0.05$ (dashed curve), or $\alpha = 0.2$ (dotted curve) at $q = 2.25$, $D_{\|} = 0.001$, $D_{\perp} = 0.001$, $D = 0.3$, $\delta_0 = 5.0$, and $t_0 = 125$.

domains under cavityless optical bistability, in line with [3–5]. It reinforced the previously drawn conclusions [3–5] that an inverse kink may be created, that diffraction instability may arise when crossing the nonuniform distributed boundary of a high-absorption domain, etc. Additionally, it has been demonstrated that diffraction may essentially cause the formation of multiple high-absorption domains (stationary or dynamic ones) in the longitudinal direction.

It should be emphasized that similar effects may occur in three-dimensional optical memory. They will manifest themselves as interstate switchings occurring behind the layer to which radiation is focused.

REFERENCES

1. H. M. Gibbs, *Optical Bistability: Controlling Light with Light* (Academic Press, Orlando, Fla., 1985; Mir, Moscow, 1988).
2. N. N. Rozanov, *Optical Bistability and Hysteresis in Distributed Nonlinear Systems* (Nauka, Moscow, 1997).
3. V. A. Trofimov, in *Proceedings of the Society of Photo-Optical Instrumentation Engineers* (SPIE, Bellingham, Washington, 1999), Vol. 3733, pp. 281–295.
4. I. G. Zakharova and V. A. Trofimov, Pis'ma Zh. Tekh. Fiz. **21**, 43 (1995).
5. O. A. Gunaze and V. A. Trofimov, Pis'ma Zh. Tekh. Fiz. **23**, 69 (1997).

Translated by A. A. Sharshakov

Technical Physics Letters, Vol. 26, No. 2, 2000, pp. 122–124. Translated from Pis'ma v Zhurnal Tekhnicheskoĭ Fiziki, Vol. 26, No. 3, 2000, pp. 67–72.

Periodic Breakdown of a Gas Layer in the Metal–Gaseous Dielectric–Insulating Semiconductor–Metal Structure under Stationary Illumination Conditions

A. D. Bondarev, P. G. Kasherininov, A. N. Lodygin, S. S. Martynov, and V. S. Khrunov

Ioffe Physicotechnical Institute, Russian Academy of Sciences, St. Petersburg, 194021 Russia

Institute of Physicotechnical Problems, Dubna, Russia

Received August 6, 1999

Abstract—The size and location of the area of gas breakdown at the surface of an M(GD)SM structure based on a bismuth silicate crystal was studied under uniform illumination conditions. The amount of energy absorbed in the crystal that leads to breakdown of the gas layer is determined. *© 2000 MAIK "Nauka/Interperiodica".*

Semiconductor dosimeters based on M(GD)SM structures, which do not exhibit polarization under irradiation, were described in [1, 2]. The absence of polarization under stationary irradiation in such dosimeters is explained by periodic breakdown of a gas layer due to formation of a polarization charge of a fixed value inside the semiconductor crystal. The initial (dark) distribution of the electric field strength is restored inside the structure after each breakdown, which prevents the polarization of dosimeters with time.

In this work, we have studied the size and location of the area of the gas breakdown at the surface of an M(GD)SM structure and determine the amount of energy absorbed in the crystal that leads to breakdown of the gas layer.

Figures 1a and 1b show variation of the repetition rate of the current pulses of the gas breakdown in the outer circuit of an M(GD)SM structure based on insulating bismuth silicate crystal ($Bi_{12}SiO_{20}$) for different values of the illuminated area of the structure. It is seen that the repetition rate of the gas breakdown pulses in the structure depends linearly on the size of the illuminated area. This linearity is indicative of the fact that the breakdown of the structure takes place not over all the illuminated area but only within certain fragments. The size of the breakdown area at the illuminated surface of the structure and the location of this area at its surface were determined by means of the polarization–optical method in M(GD)SM structures based on the insulating electrooptical crystals ($Bi_{12}SiO_{20}$).

The structure was placed between crossed polarizers and illuminated through pinholes of a fixed size by a parallel beam of monochromatic light ($\lambda = 0.63$ μm) exhibiting partial photoactive absorption inside the crystal (Fig. 2a). A constant bias voltage of $V_0 = 1500$ V applied to the structure was distributed between the gas layer and the electrooptical crystal according to their capacitances [2]. During irradiation of the structure, a part of the light absorbed inside the crystal induces polarization charge, which causes redistribution of the electric field strength between layers of the structure and leads to breakdown of the gas layer [1, 2]. The unabsorbed (transmitted) part of this polarized beam is modulated by this charge inside the structure (longitudinal Pockels effect), thus carrying information on the size of the gas discharge area and its location at the surface. This information is registered by a TV camera (Figs. 2a and 2c). At the same time, the current pulses of the gas discharge are recorded in the outer circuit of the structure (Fig. 2b). The appearance of the image of the area of gas breakdown at the surface of the structure can be explained as follows. In the absence of the external voltage ($V_0 = 0$), the light beam is stopped by the second polarizer. An image of the illuminated area appears at the TV screen immediately after application of the voltage V_0 due to the field applied to the electrooptical crystal (Fig. 2c). Under the action of the charge induced by the light beam inside the crystal, the electric field is pushed out from the crystal into the gas layer. Gas discharge occurs when the electric field strength in the gas layer reaches a critical value. The resistance of the gas layer in the breakdown area falls down virtually to zero and all the voltage applied to this fragment of the structure appears to be applied to the electrooptical crystal. As a result, the brightness of the image in this area sharply increases (Fig. 2c). The breakdown of the gas layer is accompanied by an avalanche of ionized charge carriers, representing electrons and positively charged ions [3]. The charge of these carriers diminishes the polarization electric charge formed at the plate of the air capacitor to such a

1063-7850/00/2602-0122$20.00

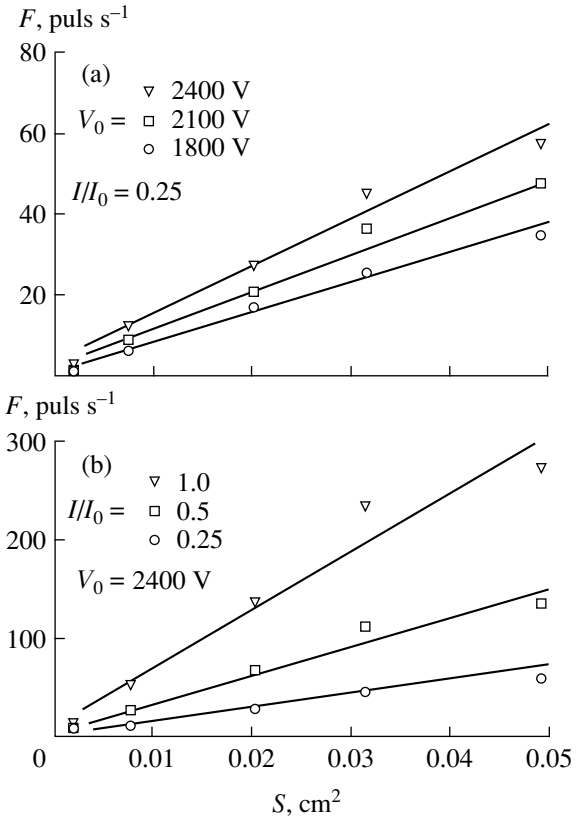

Fig. 1. Plots of the repetition rate of the current pulses in the outer circuit of M(GD)SM structure (F) vs. the illuminated surface area S, $F(S)$: (a) for a constant homogeneous illumination intensity I (incandescence lamp with green–blue color glass and neutral attenuation filters) and different applied voltages V_0; (b) for a constant applied voltage (V_0 = 2400 V) and different light intensities I at the surface of the structure I_0 is the maximal light intensity ($I_0 = 2.1 \times 10^{-7}$ W cm^2), I is the intensity of light at the illuminated surface of the structure.

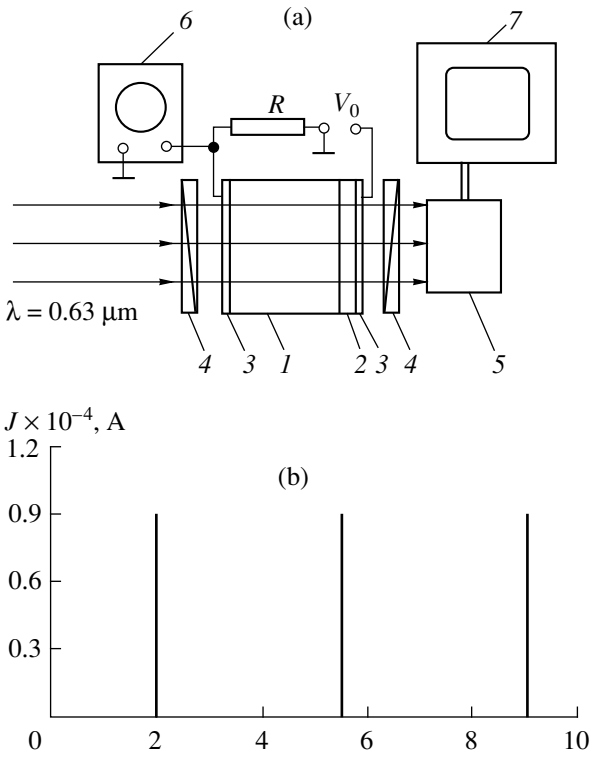

Fig. 2. The size and location of the area of gas breakdown at the surface of uniformly illuminated structure (λ = 0.63 μm, diameter of the beam d = 0.3 cm, intensity of light at the surface of the structure $I = 10^{-4}$ W m^{-2}). (a) Experimental layout: (*1*) insulating bismuth silicate crystal (thickness d = 0.15 cm); (*2*) a layer of gaseous dielectric (thickness $d_0 = 10^{-2}$ cm); (*3*) optically transparent electrodes; (*4*) crossed polarizers; (*5*, *7*) TV setup; (*6*) oscilloscope. (b) Time pattern of the current pulses in the outer circuit of the structure (applied voltage is V_0 = 1500 V). (c) Photographs of the area of gas breakdown at the surface of the structure taken from TV screen.

value that the electric field strength inside the gas layer becomes lower than the critical level. The gas discharge terminates and the gas layer returns to low-conducting state. The electric field strength distribution in the structure goes back to the initial state.

In the case of constant irradiation of the structure, the gas breakdown becomes cyclic. The image of the gas breakdown area appears on the TV screen simultaneously with the current pulse appearing in the outer circuit of the structure (Fig. 2b, 2c). It is seen from Fig. 2c that the spot of the gas breakdown at the illuminated surface of the structure has a diameter of 6×10^{-2} cm (the light beam diameter is 0.3 cm). The size of this spot weakly depends on the size of the illuminated area, intensity of light (I), and the applied voltage (V_0). In the case of stationary irradiation of the structure, each breakdown of the gas layer occurs in a new fragment of the structure surface (Fig. 2c, *1–3*). The energy of radiation absorbed inside the crystal, which is sufficient to induce breakdown of the gas layer (A), can be estimated using the following relationship:

$$A = IkdSt = 4.5 \times 10^{-7}\ \text{J},$$

where I is the intensity of the incident light, $I = 10^{-4}$ W cm^{-2}, λ = 0.63 μm, k is the absorption coefficient, $k = 10^{-1}$ cm^{-1}, d is the thickness of the crystal, $d = 1.5 \times 10^{-1}$ cm ($kd < 1$), S is the illuminated area of the crystal surface, $S = 7.2 \times 10^{-2}$ cm^2, t is the time interval between two sequential pulses of the gas discharge in the structure (t = 4.5 s (Fig. 2b)).

During the gas breakdown, the light-induced polarization charge accumulates from all surface of the structure to the area of breakdown, where the main change of the electric field strength takes place. An

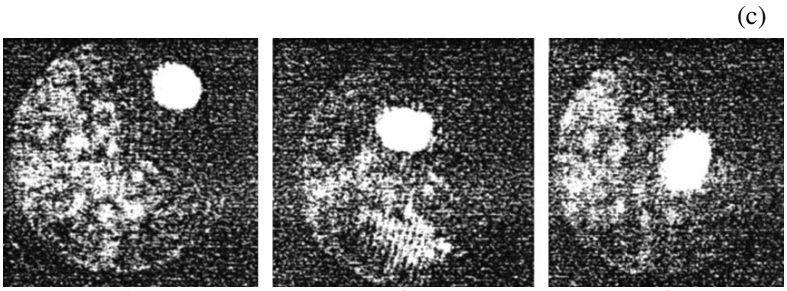

Fig. 2. (Contd.)

increase of the illuminated surface area in the structure results in increase only of the repetition rate of the current pulses. The size of the breakdown area and the energy absorbed during the time interval between two sequential pulses of the gas breakdown remain constant.

ACKNOWLEDGMENTS

This work was supported by the International Scientific–Technological Center.

REFERENCES

1. P. G. Kasherininov and A. N. Lodygin, Pis'ma Zh. Tekh. Fiz. **23**, 23 (1997).
2. P. G. Kasherininov and A. N. Lodygin, Pis'ma Zh. Tekh. Fiz. **24**, 64 (1998).
3. N. P. Bogoroditskiĭ and V. V. Pasynkov, *Materials in Radioelectronics* (Gosénergoizdat, Moscow, 1961).

Translated by A. Chikishev

Technical Physics Letters, Vol. 26, No. 2, 2000, pp. 125–127. Translated from Pis'ma v Zhurnal Tekhnicheskoĭ Fiziki, Vol. 26, No. 3, 2000, pp. 73–79.

Peculiarities of the Angular Selectivity of 3D Holograms in the Direction of Nondispersive Angular Mismatch

A. I. Khizhnyak and V. B. Markov

Institute of Applied Optics, National Academy of Sciences of Ukraine, Kiev, Ukraine
MetroLaser Inc., Skypark Circle 18010, Suite 100, Irvine, 92614 California

Received September 23, 1999

Abstract—Influence of the angular mismatch between the hologram and the reconstructing beam in the direction perpendicular to the plane of dispersion on the efficiency of diffraction was studied. It is demonstrated that angular detuning in this direction can lead to substantial increase of the intensity of the diffracted beam if the Bragg conditions are met. The results of calculation of the "anomalous" behavior of the diffraction efficiency are in good agreement with the experimental data for holograms recorded in the layers of a photopolymer. © *2000 MAIK "Nauka/Interperiodica".*

The phenomenon of angular (and spectral) selectivity of 3D phase gratings is well known and widely used for the construction of holographic optical elements [1], in the systems of holographic memory [2, 3], etc. It was demonstrated [4] that the angular mismatch $\delta\theta_1$ between grating and reconstructing beam in the dispersion plane results in a decrease of the diffracted beam intensity I_D, provided the phase shift in the grating is not greater than $\pi/2$. It is believed that the angular selectivity $\delta\theta_2$ in the direction perpendicular to the dispersion plane (tangential) is similar to (albeit less pronounced than) $\delta\theta_1$, which implies that the value I_D must also decrease on tilting the grating in this direction [5, 6].

In this paper we demonstrate that, in the case of a tangential tilt of the grating relative to the reconstructing beam, the value of I_D can substantially increase depending on the initial value of the diffraction efficiency $\eta^{(0)}$ (in the absence of the tangential tilt).

Consider a 3D holographic phase grating (Fig. 1), the wave vector of which $|K| = 2\pi/\Lambda$ belongs to the plane X–Z ($\Lambda = \lambda/2\sin\theta_0$ is the period of the grating, λ is the wavelength, and θ_0 is the angle of the beam convergence in the symmetric recording geometry). If such a hologram is reconstructed by a beam with $s(\eta_\perp)$ and $p(\eta_\parallel)$ polarization, the diffraction efficiency is given by expressions [4]:

$$\eta_\perp = \Delta\varepsilon^2 \frac{\sin^2\left(\frac{2\pi\xi}{\lambda}\sqrt{\Delta\varepsilon^2+\delta^2}\right)}{\Delta\varepsilon^2+\delta^2},$$
$$\eta_\parallel = \Delta\varepsilon^2 \frac{\sin^2\left(\frac{2\pi\xi\cos(\theta_R+\theta_S)}{\lambda}\sqrt{\Delta\varepsilon^2+\delta^2}\right)}{\Delta\varepsilon^2+\delta^2}, \quad (1)$$

where $\delta = [\cos\theta_R - \cos\theta_R] \times \sqrt{\cos\theta_R\cos\theta_S}$, θ_R^0, θ_R, and θ_S are the angles of incidence of the recording, reconstructing, and diffracted beams, respectively, $\Delta\varepsilon = 2n_G \times \Delta n$, $\xi = d/\sqrt{\cos\theta_R\cos\theta_S}$; d is the thickness and Δn is the modulation depth of the refractive index of the recording medium, and n_G is the mean refractive index.

In the case under consideration, the grating rotates around the X axis by an angle φ (Fig. 1). The Bragg condition is met if the readout angle θ_R meets the condition:

$$\theta_R = \arccos[\cos\theta_R^0\cos\varphi]. \quad (2)$$

If the refractive indices of the recording material and the surrounding medium are equal (grating in the

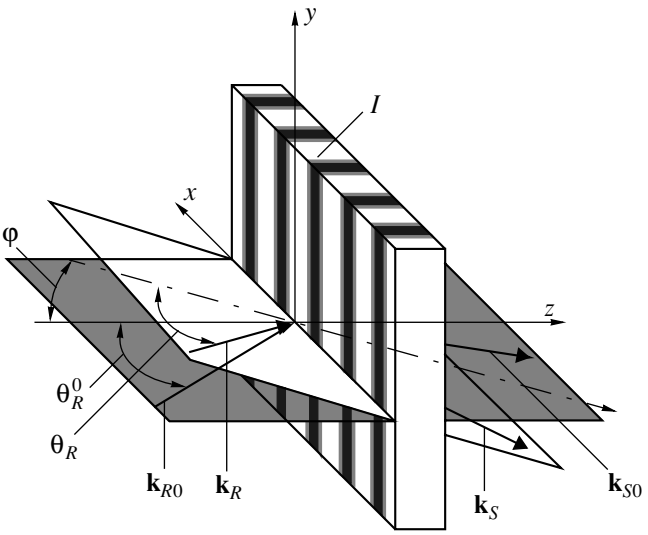

Fig. 1. Geometry of hologram reconstruction in the case of angular tilt in the tangential direction (I is a 3D grating).

1063-7850/00/2602-0125$20.00 © 2000 MAIK "Nauka/Interperiodica"

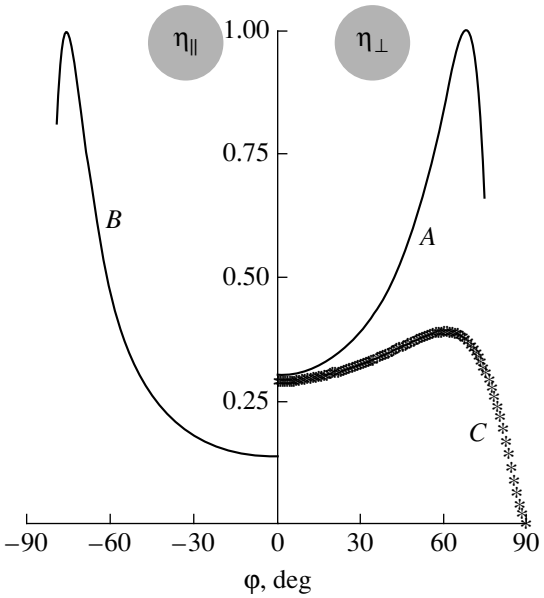

Fig. 2. Calculated diffraction efficiency $\eta_{\perp,\parallel}(\varphi)$ for $\Phi_0 = 0.6$ and the beams with (*A*) *s* and (*B*) *p* polarizations in an immersion medium and (*C*) in the free space, $n_G = 1.51$.

immersion medium), the incidence is symmetric $\theta_R^0 = \theta_S^0$ and the incidence angle is equal to the Bragg angle (the grating vector is parallel to the *X* axis), expression (1) can be rewritten as:

$$\eta_\perp(\varphi) = \sin^2[\Phi_0/\cos\varphi];$$
$$\eta_\parallel(\varphi) = \sin^2[\Phi_0\cos(2\theta_R)/\cos\varphi], \quad (3)$$

where φ is the angle of tangential detuning and $\Phi_0 = 2\pi\Delta\varepsilon^2\xi/\lambda$ is the "strength" of the grating.

Calculated curves of the diffraction efficiency $\eta_\perp(\varphi)$ and $\eta_\parallel(\varphi)$ obtained with the use of (3) are demonstrated in Fig. 2 ($\Phi_0 = 0.6$, curves *A* and *B* correspond to *s* and *p* polarizations of the beams, respectively). These data indicate that the angular detuning in the tangential direction is accompanied by substantial growth in intensity of the diffracted signal. A real increase of the intensity I_D for the given geometry is determined by the polarization of the reconstructing beam and the initial strength of the grating Φ_0. The smaller Φ_0, the more pronounced is the increase.

The situation becomes more complicated in the case of the beam diffraction on a hologram in the absence of immersion at the interface of the recording medium. In this case, the tilt by an angle φ is accompanied by a change of the reflection coefficients for the reconstructing and diffracted beams R_s and R_p at the medium interface. In addition, the increase of the angle φ changes the optical path lengths of these beams in the medium. The maximum value of this angle is limited by the angle of the total internal reflection. The corresponding expressions for $\eta_j(\varphi)$ become more complex. For example, a formula for the *s*-polarized reconstructing beam is as follows:

$$\eta_s(\varphi) = \eta_\perp^0\frac{[T_s\cos^2\varphi\sin^2\theta_B + T_p\sin^2\varphi]}{\cos^2\theta_B[\tan^2\theta_B + \sin^2\varphi]} \times\left[\sqrt{T_s} + \frac{(\sqrt{T_p} - \sqrt{T_s})\sin^2\varphi}{1 - \cos^2\varphi\sin^2\theta_B}\right], \quad (4)$$

where $T_s(\varphi, \theta)$ and $T_p(\varphi, \theta)$ are the φ- and θ-dependent transmission coefficients for the interface between two substances for *s* and *p* polarizations, respectively. The dependence $\eta_s(\varphi)$ given by (4) is also shown in Fig. 2 (curve *C*). The comparison of two $\eta_\perp(\varphi)$ curves presented in Fig. 2 shows that the absence of immersion between hologram and surrounding medium substantially lowers the intensity of the diffracted beam under tangential detuning conditions.

Experimental studies of the above-described anomalous behavior of the angular selectivity of gratings under tangential angular detuning conditions were carried out for 3D phase transmission holograms recorded in a photopolymer (DuPont HRF-150X001-38 film with a thickness of $d = 38$ μm on a glass substrate with a thickness of about 1 mm). The hologram was placed on a rotating stage with the angular resolution of 15′ in the dispersion plane and 1° in the perpendicular direction. The recording was performed in a symmetrical geometry ($\theta_S^0 = \theta_R^0 = 20°$, $\Lambda \approx 0.8$ μm) using the second harmonic radiation ($\lambda = 532$ nm) of an ADLAS-325II Nd:YAG laser ($P = 200$ mW). A He–Ne laser ($\lambda = 633$ nm) was used for readout. A half-lambda plate in this channel made it possible to rotate the polarization plane with an accuracy of about 2°.

In the major part of experiments, the initial value of the diffraction efficiency $\eta_{\perp,\parallel}^{(0)}$ did not exceed 20% for $\lambda = 630$ nm. The accuracy of determination of the diffracted beam intensity was not worse than 0.4% within the entire range of measurements. Measurements of the $\eta_{\perp,\parallel}(\varphi)$ curves were performed for the grating in the immersion medium ($n_{im} = 1.475$ for glycerol, $n_G \approx 1.49$–1.51 for the photopolymer [7]) and in the free space.

Figure 3 (dots *A*) presents the angular dependence of the normalized diffraction efficiency $\eta_\perp^{(N)}(\varphi) = \eta_\perp(\varphi)/\eta_\perp^{(0)}$ for an *s*-polarized beam. It follows from these data that the angular detuning in the tangential direction allows one to achieve virtually three-fold increase of $\eta_\perp^{(N)}$ (for $\eta_\perp^{(0)} \approx 7\%$) in the absence of reflection at the interfaces (grating in the immersion medium). The $\eta_\parallel^{(N)}(\varphi)$ curve for the *p*-polarized beam measured under given experimental conditions (inci-

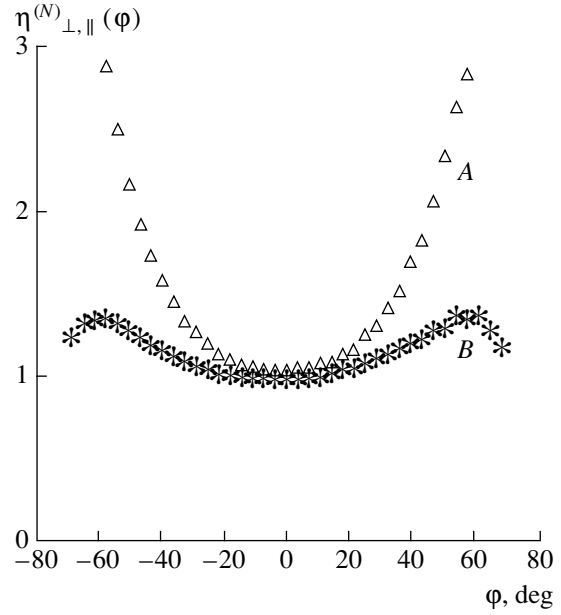

Fig. 3. Experimental curves of the normalized diffraction efficiency $\eta_\perp^N(\varphi) = \eta_\perp(\varphi)/\eta_\perp^{(0)}$ for the beams with *s* polarization: (*A*) $\Phi_0 = 0.22$, immersion medium and (*B*) $\Phi_0 = 0.6$, free space.

dence angle θ_0 and phase shift Φ_0) is virtually identical to the $\eta_\perp^{(N)}(\varphi)$ curve.

Figure 3 (curve *B*) also presents the experimental results obtained for the tangential angular selectivity of the hologram in the free space (for $\eta_\perp^{(0)} \approx 20\%$) reconstructed by the *s*-polarized beam. A comparison of curves *A* and *B* shows that the hologram–surrounding medium interface substantially limits the maximum possible value of $\eta_\perp^{(N)}(\varphi)$. For the substances with high refractive index (e.g., $LiNbO_3$ crystals) the $\eta_\perp^{(N)}(\varphi)$ curve has a decaying character. This factor accounts for the experimental behavior of $\eta(\varphi)$ reported in [5, 6].

The increase of the intensity I_D upon tangential tilt of the grating is determined by the increase of the effective phase shift Φ. Indeed, detuning by an angle φ in the tangential direction, provided that the Bragg conditions are retained, does not break (according to (1)) the matching of the wave vectors of the grating and the reconstructing and diffracted beams ($k_{R0} - k_{S0} = k_R - k_S = K$, see Fig. 1). At the same time, the detuning in this direction leads to an increase of the optical path length inside the grating, which results in the growth of the value of Φ and, as a consequence, in the variation of I_D.

In conclusion, note that the anomalous character of the dependence of the diffracted beam intensity on the tangential tilt of the 3D phase grating demonstrated in this work is typical not only of 3D gratings but of the relief ones as well. In the case of thin gratings, this results in redistribution of the intensity between the diffraction orders.

REFERENCES

1. A. P. Rambottom and S. A. Sergeant, Proc. SPIE **1667**, 146 (1992).
2. F. Mok, Opt. Lett. **18**, 915 (1993).
3. J. Rosen, M. Segev, and A. Yarive, Opt. Lett. **18**, 744 (1993).
4. H. Kogelnik, Bell Syst. Tech. J. **48**, 2909 (1969).
5. V. Markov, A. Khizhnyak, and V. Shishkov, Ukr. Phys. J. **30**, 508 (1985).
6. E. A. Sander, V. V. Shkunov, and S. A. Shoydin, Sov. Phys. JETP **61**, 68 (1985).
7. A. M. Weber, W. K. Smothers, *et al.*, Proc. SPIE **1212**, 30 (1990).

Translated by A. Chikishev

Technical Physics Letters, Vol. 26, No. 2, 2000, pp. 128–130. Translated from Pis'ma v Zhurnal Tekhnicheskoĭ Fiziki, Vol. 26, No. 3, 2000, pp. 80–85.

Autooscillation Instability of the Free Surface of a Viscoelastic Medium

D. F. Belonozhko and A. I. Grigor'ev

Demidov State University, Yaroslavl', Russia

Received September 24, 1999

Abstract—Oscillation instability of a layer of viscoelastic liquid is revealed on the basis of the numerical analysis of the dispersion equation. The instability is observed in the case of time-independent uniform external force action on the free surface of the liquid and may lead to the formation of a regular wavelike relief of a finite amplitude. © *2000 MAIK "Nauka/Interperiodica".*

Theoretical analysis of the laws of formation of a wavelike relief on the initially flat surface of a viscoelastic material under the action of external forces is one of the important problems in modern physics. This external force action causes normal and tangential surface tensions (explosion welding [1], formation of the regular wavelike relief on a silicon surface bombarded by a high-energy ion beam [2]). Below we will consider this phenomenon within the framework of a simplest hydrodynamic model.

1. Assume that a flat layer of a viscoelastic liquid (density ρ, kinematic viscosity ν_0, time of viscosity relaxation τ, and thickness d) on a solid substrate in the field of gravity $\mathbf{g}$ experiences continuous force action. This action is provided by oblique incidence of a momentum flux (e.g., of a material beam). The task is to determine a spectrum of the capillary motions and to study their stability in time.

Let $\Pi_{jk} = \delta V_j V_k$ be the tensor of the external momentum flux density over the surface of the layer (V_j are the components of the beam velocity, β is the angle of incidence, and δ is the volume density) [3]. Consider a 2D problem in the Cartesian coordinates XOZ with the vertical OZ axis ($\mathbf{n}_z \| -\mathbf{g}$). The coordinate of the solid bottom is $z = -d$ and the equation of the disturbed free boundary of the layer can be presented as $z = \xi(x, t)$, $|\xi| \ll d$. We neglect the phenomena related with the inflow of substance into the liquid. Under the approximation of the waves of infinitely small amplitude, the mathematical formulation of the problem can be presented as:

$$\frac{\partial \mathbf{U}}{\partial t} + [\nabla \times \mathbf{U}] \times \mathbf{U} = -\frac{1}{\rho}\nabla\left(P + \frac{U^2}{2}\right) + \nu\Delta\mathbf{U} + \mathbf{g},$$

$$\operatorname{div}\mathbf{U} = 0,$$

$$z = \xi: \frac{\partial \xi}{\partial t} = U_z - U_x\frac{\partial \xi}{\partial x},$$

$$\sigma_{jk}n_k^* + \Pi_{jk}n_k = P_\gamma n_j,$$

$$P_\gamma = -\gamma\frac{\partial^2 \xi}{\partial x^2}, \quad n_j = \begin{bmatrix} -\dfrac{\partial \xi}{\partial x} \\ 1 \end{bmatrix},$$

$$n_j^* = \begin{bmatrix} \dfrac{\partial \xi}{\partial x} \\ -1 \end{bmatrix}, \quad \Pi_{jk} = \begin{bmatrix} \delta V_x^2 & \delta V_x V_z \\ \delta V_x V_z & \delta V_z^2 \end{bmatrix},$$

$$\sigma_{jk} = \begin{bmatrix} \rho U_x^2 + P - 2\rho\nu\dfrac{\partial U_x}{\partial x} & \rho U_x U_z - \rho\nu\left(\dfrac{\partial U_x}{\partial z} + \dfrac{\partial U_z}{\partial x}\right) \\ \rho U_x U_z - \rho\nu\left(\dfrac{\partial U_x}{\partial z} + \dfrac{\partial U_z}{\partial x}\right) & \rho U_z^2 + P - 2\rho\nu\dfrac{\partial U_z}{\partial z} \end{bmatrix},$$

$$z = -d: \mathbf{U} = 0.$$

Here P_γ is the Laplace pressure under the curved surface of the liquid [3]; γ is the coefficient of the surface tension, n_j is the column of coordinates of the external normal to the surface of the liquid, n_j^* is the vector–column of the internal normal, Π_{jk} and σ_{jk} are square

1063-7850/00/2602-0128$20.00 © 2000 MAIK "Nauka/Interperiodica"

matrices composed of the components of tensors of the momentum flux density above and below the disturbed surface [3]. Let us assume that the disturbance of the initially flat surface $\xi(x, t)$ has the shape of a traveling wave with the wave vector k and the complex frequency s:

$$\xi = \xi_0 \exp(st - ikx).$$

Following [3–5], we also assume that the frequency dependence of the viscosity ν is given by the Maxwell formula:

$$\nu = \frac{\nu_0}{1 + s\tau}.$$

It can be easily demonstrated that, provided the viscosity is sufficiently high, the velocity of the stationary flow of liquid under the influence of the given force action along the horizontal axis is of the first order of smallness with respect to ξ (the same as the velocity wave motions in the liquid). The corresponding condition can be presented as follows:

$$\frac{\delta}{\rho}\frac{V^2|\sin(2\beta)|}{2\nu|s|}kd = \frac{\delta}{\rho}\frac{V^2}{|u_k u_\nu|}\frac{|\sin(2\beta)|}{2}$$

$$= \frac{\delta}{\rho}\frac{V^2|\sin(2\beta)|}{2|u_k|^2}kd|\alpha| \lesssim 1,$$

$$u_k = \frac{s}{k}, \quad u_\nu = \frac{\nu}{d}, \quad \alpha = \frac{s}{\nu k^2}.$$

Using dimensionless variables for which $\rho = \gamma = g = 1$, one can rewrite the dispersion equation of this problem in the following way:

$$k^2 q\left(4s(k^2 + q^2) - (3k + q)\frac{W}{\nu}\right)$$

$$+ \frac{s\omega_0^2}{\nu^2}(k\cosh(kd)\sinh(qd) - q\sinh(kd)\cosh(qd))$$

$$- 2k^3 q\left(2s - \frac{W}{\nu}\right)$$

$$\times (k\cosh(kd)\cosh(qd) - q\sinh(kd)\sinh(qd))$$

$$+ (k^2 + q^2)\left(s(k^2 + q^2) - k^2\frac{W}{\nu}\right)$$

$$\times (k\sinh(kd)\sinh(qd) - q\cosh(kd)\cosh(qd)) = 0,$$

$$q^2 \equiv k^2 + s/\nu, \quad \omega_0^2 \equiv k(1 + k^2),$$

$$W \equiv -(\delta/\rho)\sqrt{\rho/(g\gamma)}V^2\cos(2\beta).$$

The laws of the behavior of different solutions of this equation were analyzed numerically. If $\tau = 0$, one deals with normal viscous liquid and the dispersion equation has a complex solution describing the properties of the capillary waves and an infinite family of real solutions that corresponds to decrements of the aperiodic motions caused by reflection of the capillary motions from the bottom [6]. The latter will be called the (*a*)-solutions of the dispersion equation. Another infinite family of aperiodic solutions, related to the reflection of viscoelastic capillary motions from the bottom, appears if the liquid possesses elastic properties. These will be referred to as the (*b*) solutions of the dispersion equation. If the relaxation time τ is large enough, (*a*) and (*b*) solutions interact in pairs, which is seen in Fig. 1 presenting plots of the real and imaginary components of the complex frequency s versus the characteristic relaxation time of the elastic stresses τ calculated for $k = 1$, $W = 0$, and $\nu = 0.5$. The branches of the viscoelastic wave motions *1*, *2*, and *3* formed in the case of these pair interactions are characterized, in the case of small τ, by rather high values of decay decrements and frequencies. (Note that in Fig. 1 the branch of capillary motions coincides with the abscissa axis.) The values of decrements and frequencies of these motions decrease rapidly with increasing τ. The physi-

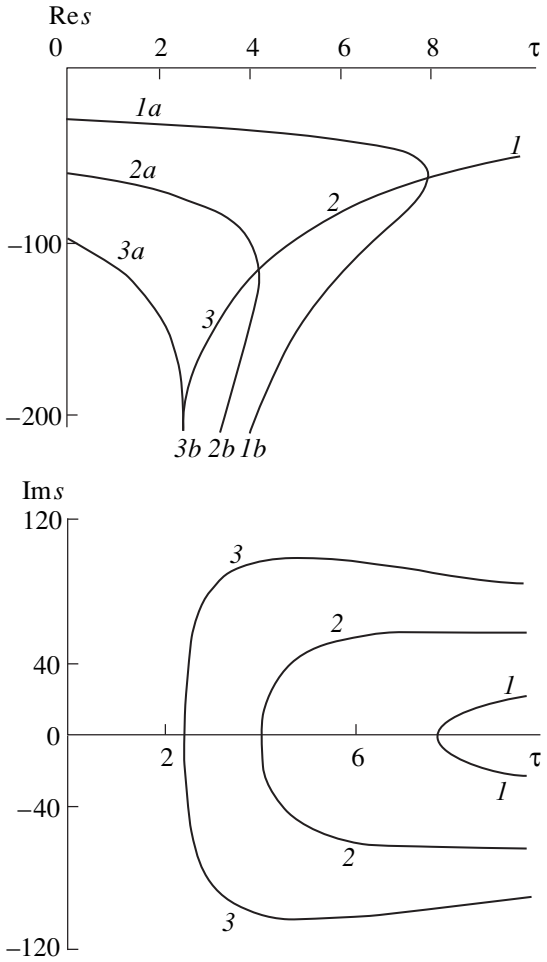

Fig. 1. Plots of the real $\mathrm{Re}s = \mathrm{Re}s(\tau)$ and imaginary $\mathrm{Im}s = \mathrm{Im}s(\tau)$ components of the complex frequency versus the characteristic relaxation time of the elastic stresses τ calculated for $k = 1$, $kd = 1$, $\nu = 0.5$, and $W = 0$.

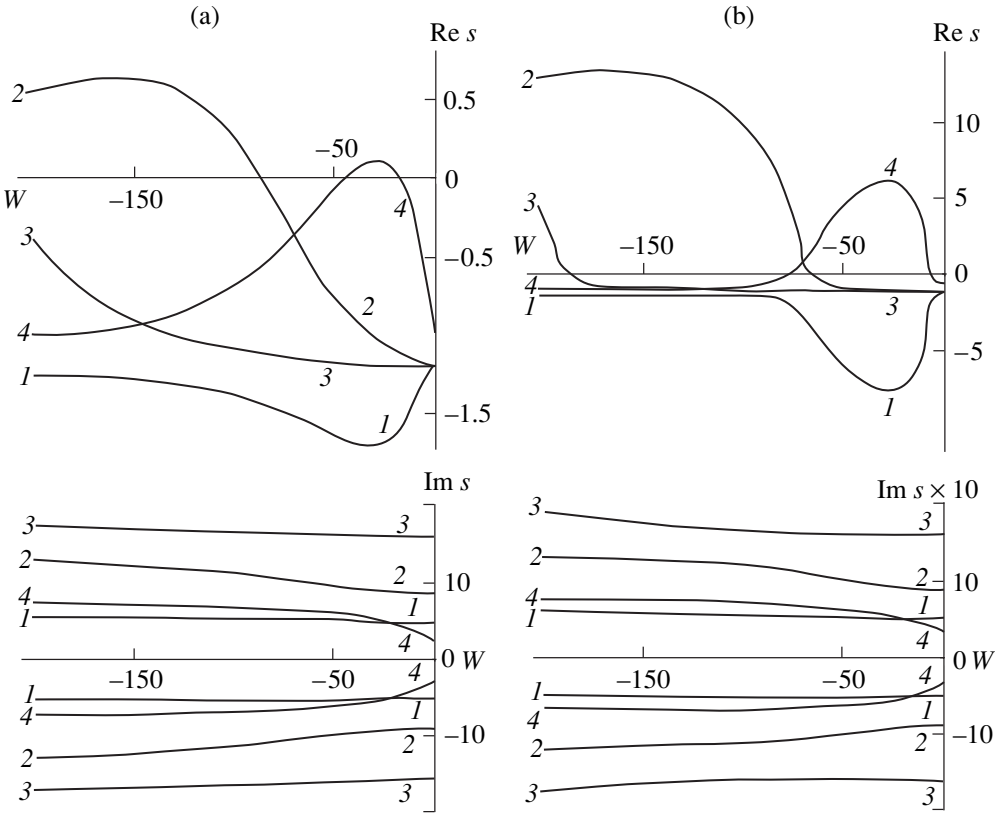

Fig. 2. Plots of the real Res = Res(W) and imaginary Ims = Ims(W) components of the complex frequency versus the dimensionless parameter W calculated for (a) $\tau = 0.1$ and (b) $\tau = 0.4$. The other parameters are the same as in Fig. 1.

cal parameters of viscoelastic and capillary waves become comparable if τ is about several tenths.

In Fig. 2a we demonstrate the same solutions of equation (1) as in Fig. 1, as functions of the parameter W for $\tau = 0.4$. Additionally we present the branch of the capillary waves (curve *4*). To avoid overload of the figure, we do not show other branches of the dispersion solution that are not related directly to the subject of this paper. It is seen that the real components of the capillary–wave branch *4* can be positive (Res > 0). The same holds for the branch of the viscoelastic waves *2* with large absolute values of negative W. These positive real components determine the increments of the oscillation instability of the corresponding motions in this region. The calculations show that an increase of the wavenumber k and the characteristic time of relaxation of the elastic stresses τ results in the increase of the increments of the corresponding instabilities. Figure 2b shows the same plots as Figure 2a but calculated for $k = 10$. It is seen that the increase of k by an order of magnitude is accompanied by a comparable increase of the value of the increment of instability, a substantial widening of the range of instability, and a shift of the right boundary of this range to $W = 0$. No oscillation instability is observed for $W \geq 0$.

Conclusion. It follows from Fig. 2 and the results of calculations that various types of wave motions can be realized in a layer of viscoelastic medium. These motions can be unstable relative to the external force action on the free surface. It is most probable that the oscillation instability of the branch of the capillary waves is detected in experiments. The capillary waves are unstable under smaller values of W than are the viscoelastic motions. Increments of the unstable wave motions grow with increasing wavenumber.

REFERENCES

1. A. N. Dermin and A. N. Mikhaĭlov, in *Proceedings of IV International Symposium on Processing of Metals by Explosion, Gotvaldov, Czechoslovakia, 1979*, p. 29.
2. V. K. Smirnov, D. S. Kibakov, S. A. Krivelevich, *et al.*, Nucl. Instrum. Methods Phys. Res., Sect. B **147**, 310 (1999).
3. L. D. Landau and E. M. Lifshitz, *Mechanics of Continuous Media* (Nauka, Moscow, 1953).
4. S. O. Shiryaeva, O. A. Grigor'ev, M. I. Munichev, *et al.*, Zh. Tekh. Fiz. **66**, 47 (1996).
5. O. A. Grigor'ev and S. O. Shiryaeva, Izv. Ross. Akad. Nauk, No. 1, 98 (1996).
6. A. I. Grigor'ev, S. O. Shiryaeva, V. A. Koromyslov, *et al.*, Zh. Tekh. Fiz. **67**, 27 (1997).

Translated by A. Chikishev

Technical Physics Letters, Vol. 26, No. 2, 2000, pp. 131–134. Translated from Pis'ma v Zhurnal Tekhnicheskoĭ Fiziki, Vol. 26, No. 3, 2000, pp. 86–94.

The Temperature Dependence of Heat Capacity and Relaxation Time for a Second-Order Ferroelectric Phase Transition

S. A. Romanchuk

Moscow State University, Moscow, 119899 Russia

Received September 29, 1999

Abstract—The simplest ferroelectric model is used to calculate the temperature dependence of heat capacity and relaxation time for all values of temperature including the critical point. The description of a second-order phase transition is based on a kinetic equation for the distribution function of an internal parameter suggested by Klimontovich [1–3]. A comparison is made between the results of the heat capacity calculation by the Landau theory and that based on the Boltzmann distribution, which is an equilibrium solution of the kinetic equation. The heat capacity and relaxation time are continuous functions in the entire temperature range including the critical point. Both analytical and numerical calculations are performed, and a comparison is made with the estimates previously obtained by Klimontovich using the same approach. © *2000 MAIK "Nauka/Interperiodica"*.

1. INTRODUCTION

Klimontovich [1–3] suggested to use the following kinetic equation for the distribution function of an internal parameter x to describe a second-order phase transition in a ferroelectric:

$$\frac{\partial f(x, R, t)}{\partial t} = \frac{\partial}{\partial x}\left[D_x\frac{\partial f}{\partial x} + \frac{1}{m\gamma}\frac{\partial h_{\text{eff}}(x, a_f)}{\partial x}f\right] + D\frac{\partial^2 f}{\partial R^2}, \quad (1)$$

where the following notation is introduced for the effective potential energy of a nonlinear oscillator:

$$h_{\text{eff}} = \frac{m\omega_0^2 x^2}{2}\left[1 - a_f + \frac{bx^2}{2}\right]. \quad (2)$$

Equation (1) describes behavior of the medium of oscillators distributed in a space (variable R) where their positions are described by an internal parameter x, which has, for example, the meaning of distance between ions in a one-ion model of crystal [4]. The dipole interaction between oscillators is described in terms of the effective Lorentz field (parameter a_f in equation (2)). The phase transition is described by a phenomenological dependence of the parameter a_f on the temperature:

$$1 - a_f = \frac{T - T_c}{T_c}. \quad (3)$$

An equilibrium solution of equation (1) is given by the Boltzmann distribution

$$f(x) = \exp\left(\frac{\phi - h_{\text{eff}}(x)}{kT}\right). \quad (4)$$

Because the interaction between various oscillators is described only in terms of the parameter a_f representing the effective Lorentz field, the calculation of thermodynamic quantities presents no difficulties: the total free energy of a crystal is given as

$$F = N\phi. \quad (5)$$

Based on these considerations, Klimontovich [2, 3] estimated the temperature behavior of heat capacity. In this study, the heat capacity is calculated on the basis of equation (5) in exact form for the entire temperature range.

By solving kinetic equation (1), we can find the quantities characterizing the kinetics of phase transition, in addition to analysis of the equilibrium state. We have solved this equation numerically and obtained a temperature dependence of the relaxation time, which can be compared with the estimates made in [3].

2. CALCULATION OF THERMODYNAMIC FUNCTIONS

First, let us write the expression for h_{eff} into a more convenient form by introducing the following parameters:

$$a = 1 - a_f; \quad \xi = \frac{x}{x_T}; \quad x_T^2 = \frac{kT}{m\omega_0^2};$$
$$x_T = x_{T_c}\sqrt{T/T_c}; \quad \varepsilon = x_T^2 b. \quad (6)$$

1063-7850/00/2602-0131$20.00 © 2000 MAIK "Nauka/Interperiodica"

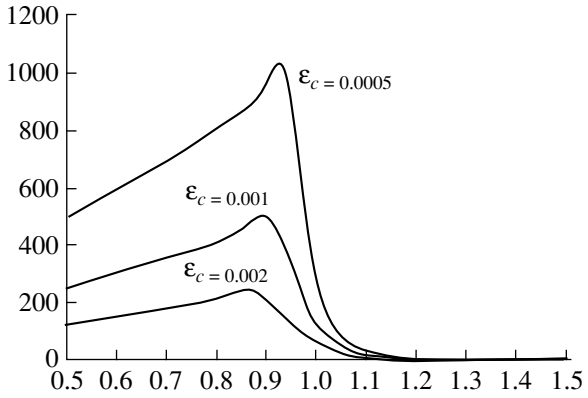

Fig. 1. The plots of heat capacity versus temperature in the vicinity of the critical point ($T/T_c = 1$).

Then, the expression for h_{eff} takes the form

$$h_{\text{eff}} = kT\frac{\xi^2}{2}\left(a + \frac{\varepsilon}{2}\xi^2\right). \quad (7)$$

The free energy of a system of oscillators is written as

$$F = -kTN\ln z, \quad (8)$$

where

$$z = x_T\int \exp\left(-\frac{\xi^2}{2}\left(a + \frac{\varepsilon}{2}\xi^2\right)\right)d\xi. \quad (9)$$

Therefore, given the partition function (9), we can find all thermodynamic functions of the system. In particular, the heat capacity is

$$C = -T\frac{\partial^2 F}{\partial T^2}. \quad (10)$$

The integral in equation (9) is expressed in terms of the Weber functions:

$$z = x_{T_c}\Gamma\left(\frac{1}{2}\right)\left(\frac{2T}{\varepsilon_c T_c}\right)^{1/4}\exp\left(\frac{a^2 T_c}{8\varepsilon_c T}\right)u\left(0, a\sqrt{\frac{T_c}{2\varepsilon_c T}}\right). \quad (11)$$

We perform differentiation of (11) to derive, according to (10), the heat capacity as a function of the temperature. Without writing the relevant formula, we will present the calculation results graphically for different values of the nonlinearity parameter ε_c (Fig. 1).

One can see that the behavior of heat capacity is regular in the entire temperature range and is a combination of the classical Landau "step," emerging upon the transition of temperature across T_c, and a peak in this region. The heat capacity maximum exhibits a shift from T_c toward lower temperatures, as may be demonstrated by direct differentiation of (11) at $T = T_c$.

This result is due to the fact that we took into account fluctuations of the microscopic dipole moment (which is the order parameter in the Landau theory), because the dispersion of the introduced distribution function is independent of the number of particles and gives a contribution to the partition function at any temperature, in contrast to the Landau theory where all calculations are based on the maximum probable values of the order parameter.

3. SOLUTION OF KINETIC EQUATION

In order to obtain all characteristics of a phase transition described by the kinetic equation, one has to obtain a solution (i.e., a distribution function) which, in the case of a nonequilibrium initial distribution, is a time-dependent function. Because it is impossible to derive an analytical solution of this equation in the general form, the problem was solved numerically. Attempts at constructing a stable difference scheme for this equation were unsuccessful. It was decided to take an unconventional step by recourse to considering a system of points described by some Langevin's equations. For the distribution function of these points to be the required distribution function, it is necessary and sufficient that the kinetic equation would be the Fokker–Planck equation for a model system of points. Therefore, the problem arises of constructing Langevin's equations using the Fokker–Planck equation. On writing kinetic equation (1) in a divergent form,

$$\frac{\partial f}{\partial t} = -\text{div}(\mathbf{J}), \quad (12)$$

where

$$J_x = -D_x\frac{\partial f}{\partial x} - \frac{1}{m\gamma}\frac{\partial h_{\text{eff}}}{\partial x}f, \quad J_R = -D_R\frac{\partial f}{\partial R},$$

one can write Langevin's equations corresponding to (12),

$$\begin{cases}\dfrac{dx}{dt} = -\dfrac{1}{m\gamma}\dfrac{\partial h}{\partial x} + \dfrac{dw_x}{dt} \\ \dfrac{dR}{dt} = \dfrac{dw_R}{dt},\end{cases}$$

where w_x and w_R are Gaussian processes,

$$E((w_\alpha(t) - w_\alpha(t_0))^2) = 2D_\alpha(t - t_0). \quad (13)$$

Nor is it difficult to numerically solve the set of Langevin's equations for two coordinates. According to these equations, one can obtain the coordinates of all points on the plane after a short period of time by finding the respective increments of coordinates (determined at each step using Langevin's equations). In so doing, a random number generator was used obeying Gaussian distribution with desired dispersion.

This method is advantageous in that the stability problems are eliminated: the algorithm remains correct at practically any step (i.e., is absolutely stable). A disadvantage of the method consists in that the motion of a large number of points must be followed in order to

obtain a sufficiently smooth distribution function, which is a rather labor-consuming computational procedure. The accuracy of calculation of the distribution function is proportional to the square root of the number of points, while the calculation time is directly proportional to this number, which is a serious drawback. However, the first factor is decisive: the method enables one to solve the equation, and insufficient smoothness of the distribution function is not a significant factor for the calculation of most parameters (for example, the mean energy or dispersion).

4. CALCULATION OF RELAXATION TIME

Once it is possible to solve equation (1), we can find a relaxation time for the system described by this equation. We will define the relaxation time as a characteristic time during which an initial nonequilibrium distribution changes to the equilibrium one (at a small initial deviation). We select the second moment as a parameter characterizing the distribution. Then, the dispersion of distribution as a function of time is well approximated by an exponential function, with the exponent being the inverse relaxation time.

For theoretical estimation of the relaxation time, we will use a self-consistent approximation for the second moment of the distribution function, suggested by Klimontovich in [3]. For this purpose, we will multiply (1) by x^2 and integrate with respect to dx. Integration by parts yields the following equation for $E = \langle x^2 \rangle$ (in view of the approximation $\langle x^4 \rangle \Rightarrow E^2$):

$$\frac{\partial E(R, f)}{\partial t} = 2D_x - 2\Gamma(1 - a_f + bE)E + D_R\frac{\partial^2 E}{\partial R^2}. \quad (14)$$

A stationary uniform solution is found from the equation

$$E^2 + \frac{1 - a_f}{b}E = \frac{D_x}{\Gamma b}. \quad (15)$$

Using equation (15) with an appropriate Langevin source $\delta y_E(k, t)$, we obtain, in a linear approximation, an equation for the Fourier fluctuation components $\delta E(k, t)$,

$$\frac{\partial \delta E(k, t)}{\partial t} + \frac{\delta E(k, t)}{\tau_E} = \delta y_E(k, t), \quad (16)$$

where the relaxation time τ_E is determined by the formula

$$\frac{1}{\tau_E} = 2\Gamma\left(\frac{T - T_c}{T_c} + 2bE\right) + D_R k^2 \quad (17)$$

with E given by the solution of equation (15).

The results of direct numerical calculations of the relaxation time, performed in accordance with this algorithm, are in good agreement with the theoretical estimates given above. In order to derive the function $\delta E(t)$, a uniform steady state (corresponding to $k = 0$ in (17)) was taken as a basis and subjected to perturbation by varying the temperature $T \longrightarrow T + \delta T$. Therefore, the former equilibrium state was no longer equilibrium and evolved with time to a new steady state corresponding to the temperature $T + \delta T$. The calculation results are plotted in Fig. 2. As is seen, the peak of relaxation time is shifted from T_c toward lower temperatures and, away from the critical point, the relaxation time drops by the Curie law.

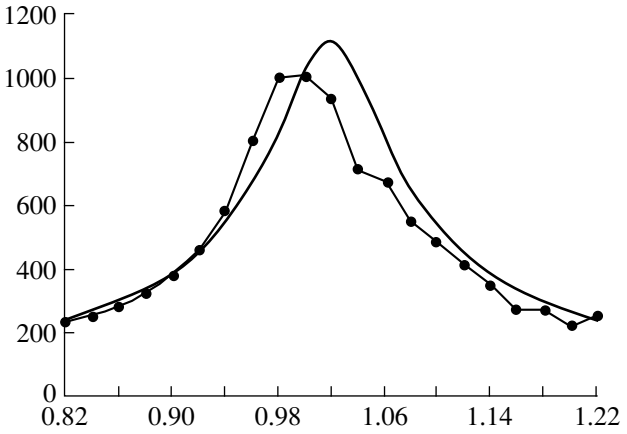

Fig. 2. The relaxation time of $\langle x^2 \rangle$ as function of the temperature ($\varepsilon_c = 0.0005$).

5. CONCLUSION

In this study, an exact calculation of the temperature behavior of heat capacity is performed using the approach suggested by Klimontovich. In so doing, the form of effective Hamiltonian (which is the reason for the presence of phase transition in the system) remained essentially the same as in the Landau theory [5], which allows this model to be applied to ferroelectrics and to be used as a basis for the general treatment of second-order phase transitions. For example, the temperature dependence of heat capacity, similar to that obtained above, was observed experimentally in magnetics (for example, in $Fe_{72}Pt_{28}$ Invar [6]) and calculated using a different model for Cr_2O_3 [7].

Within the given approach, the meaning of the order parameter varies: in our treatment, it is the distance between maxima of the distribution function. The order parameter still characterizes variation of the symmetry of the system (the distribution function acquires two maxima instead of one upon transition through the critical point); however, the system need not experience spontaneous polarization (or magnetization for magnetics) – the first moment of the stationary distribution function remains zero as before.

The use of kinetic equation (1) enables one to describe the kinetic properties of the phase transition as well. By numerically solving this equation, we

obtained a temperature dependence of the relaxation time. The relaxation time in a system actually obeys the Curie law at some distance away from the critical point and has a finite value at $T = T_c$.

The obtained results point to the possibility of describing the properties of phase transition in the entire temperature range including the critical point.

REFERENCES

1. Yu. L. Klimontovich, *Statistical Theory of Open Systems* (Yanus, Moscow, 1995; Kluwer Academic, Dordrecht, 1995).
2. Yu. L. Klimontovich, Phys. Lett. A **210**, 65 (1996).
3. Yu. L. Klimontovich, Int. J. Bifurc. Chaos **8**, 661 (1998).
4. B. A. Strukov and A. P. Livanyuk, *Physical Principles of Ferroelectric Phenomena in Crystals* (Nauka, Moscow, 1995).
5. L. D. Landau and E. M. Lifshits, *Statistical Physics* (Nauka, Moscow, 1995; Pergamon, Oxford, 1980), Part 1.
6. B. J. Rellinghaus and E. F. Wassermann, Phys. Rev. B: Condens. Matter **51** (5), 2983 (1995).
7. N. K. Kamilov, A. K. Murtazaev, and Kh. K. Aliev, Usp. Fiz. Nauk **169**, 783 (1999) [Phys. Uspekhi **169**, 783 (1999)].

Translated by H. Bronsteĭn

Technical Physics Letters, Vol. 26, No. 2, 2000, pp. 135–136. Translated from Pis'ma v Zhurnal Tekhnicheskoĭ Fiziki, Vol. 26, No. 4, 2000, pp. 1–4.

The Effect of Phonon Heating on the Transverse Runaway of Hot Electrons

Z. S. Kachlishvili, N. K. Metreveli, and F. G. Chumburidze

Tbilisi State University, Tbilisi, Georgia

Received June 2, 1999

Abstract—A study is made of the influence of phonon heating on the transverse runaway of hot electrons. Under standard conditions, in which the runaway effect is realized, the equilibrium phonon distribution may be disturbed: it is demonstrated that the phonon heating delays the transverse runaway of hot electrons. © *2000 MAIK "Nauka/Interperiodica".*

It was demonstrated in [1, 2] that, for some combination of mechanisms of scattering of energy and momentum of hot electrons and a certain threshold value of applied electric (magnetic) field, the Hall field (and, consequently, the internal field) tends to infinity. Hence the prospects are obvious for using this effect, which came to be known as transverse runaway (TR) [1]. As was shown in [3], the TR effect is not associated with any approximation. However, the investigation in [1–3] was performed under conditions of an equilibrium phonon subsystem. It is obvious that, under standard conditions of TR experiments (or in the case of practical utilization of this effect), the thermodynamic equilibrium of phonons may be disturbed if no appropriate measures are taken. Therefore, a question naturally arises as to what effect may the phonon heating produce on the TR. We have treated this problem within the framework of the electron temperature approximation in accordance with the procedure described in [3].

Let us consider a homogeneous semiconductor in crossed strong electric and magnetic fields **E** and **H**, respectively. In order to find the nonequilibrium distribution functions for hot electrons and phonons, one must solve the set of kinetic Boltzmann equations for electrons and phonons. This rather complex problem is simplified considerably in an approximation in which the distribution functions for the electron and phonon subsystems are of the Maxwell and Planck types, respectively, with the same effective temperature equal to the electron temperature T_e. In this case, one equation is available for determining T_e [4] instead of a set of energy balance equations, i.e.,

$$(\mathbf{jE}) = P(\theta), \tag{1}$$

where

$$P(\theta) = P_{f1}(T)\theta^{\alpha}(\theta - 1) \tag{2}$$

is the energy transferred from long-wavelength phonons (LWP) to a heat sink (to short-wavelength phonons, $l = f$ and $\alpha = 2$) or to the sample boundaries ($l = h$ and $\alpha = 3/2$), and $\theta = T_e/T$. The current density is conventionally expressed as

$$\mathbf{j} = -en\left\{\mu_1\mathbf{E} + \mu_2\frac{[\mathbf{EH}]}{H}\right\}. \tag{3}$$

Therefore, we assume that the energy of hot electrons is transferred to heated LWPs and the momentum is scattered by lattice defects. Then, the free path of electrons with respect to momentum may be written as [5]

$$l(y) = l_0 y^{\frac{1+t}{2}}\theta^r, \tag{4}$$

where $y = \varepsilon/k_0T_e$ and the values of the parameters t and r for all known mechanisms of scattering are given in [5].

In view of (4), the mobilities μ_1 and μ_2 may be written as

$$\frac{\mu_1}{\mu_0} = \frac{\theta^{\frac{2r-1}{2}}}{\Gamma\left(\frac{t+5}{2}\right)}\mathcal{J}_1, \quad \frac{\mu_2}{\mu_0} = \frac{\theta^{2r-1}}{\Gamma\left(\frac{t+5}{2}\right)}\sqrt{\eta}\,\mathcal{J}_2, \tag{5}$$

where

$$\mathcal{J}_1 = \int_0^\infty \frac{e^{-y}y^{\frac{t+3}{2}}dy}{1+\eta y^t\theta^{2r-1}}, \quad \mathcal{J}_2 = \int_0^\infty \frac{e^{-y}y^{\frac{2t+3}{2}}dy}{1+\eta y^t\theta^{2r-1}}, \tag{6}$$

$\eta = (H/H_0)^2$, $H_0 \equiv (2mk_0T)^{1/2}c/el_0$, c is the velocity of light, and μ_0 is the mobility in a weak electric field.

Let an electric field E_x be applied and a current J_x flow along the X axis, and let a magnetic field be directed along the Z axis. With the Hall field defined

under no-load conditions ($J_y = 0$), the equation of energy balance (1) takes the form

$$\frac{en\mu_0}{\Gamma\left(\frac{t+5}{2}\right)}\theta^{\frac{2r-1}{2}}\mathcal{J}_1\left\{1+\eta\theta^{2r-1}\left(\frac{\mathcal{J}_2}{\mathcal{J}_1}\right)^2\right\} = P_{f1}(T)\theta^{\alpha}(\theta-1). \quad (7)$$

It is of interest to clarify the question whether a combination of scattering mechanisms exists for which the solution of equation (7) goes to infinity as a function of one of the parameters E_x and H. Note that, with $\theta \longrightarrow \infty$, the distribution function cannot be normalized; i.e., a runaway of hot electrons occurs.

An analytical solution of (7) is possible only in the approximation of strong ($\eta y^t \theta^{2r-1} \gg 1$) and weak ($\eta y^t \theta^{2r-1} \ll 1$) magnetic fields.

Calculating the integrals $\mathcal{J}_1$ and $\mathcal{J}_2$ in the foregoing approximations and taking into account the conditions of the runaway onset with respect to the applied electric field (with $\mathbf{H}$ = const) $\partial\theta/\partial E_x \longrightarrow \infty$, we obtain an equation for the asymptotic values of θ. It follows from this equation that θ goes to infinity for some finite values of E_x. The respective scattering mechanisms are found. We have separately treated the presence of heat sink ($\alpha = 2$) and sample boundary ($\alpha = 3/2$). The resultant expressions show that, in all cases with a strong magnetic field, solutions of the asymptotic equation exist only for nonrealistic mechanisms of scattering. As to a weak magnetic field, no solution exists in one case. In the other case, a solution exists; however, the runaway conditions are not valid for real mechanisms of scattering.

Based on the obtained results, we conclude that the heating of phonons delays the transverse runaway of hot electrons.

REFERENCES

1. Z. S. Kachlishvili, Zh. Éksp. Teor. Fiz. **78**, 1955 (1980) [Sov. Phys. JETP **51**, 982 (1980)].
2. Z. S. Kachlishvili and F. G. Chumburidze, Zh. Éksp. Teor. Fiz. **87**, 1834 (1987) [Sov. Phys. JETP **87**, 1029 (1987)].
3. Z. S. Kachlishvili and F. G. Chumburidze, Zh. Éksp. Teor. Fiz. **113**, 688 (1998) [JETP **86**, 380 (1980)].
4. T. M. Gasymov and L. É. Gurevich, Fiz. Tverd. Tela (Leningrad) **9**, 106 (1967) [Sov. Phys. Solid State **9**, 78 (1967)].
5. T. O. Gegechkori and Z. S. Kachlishvili, Phys. Status Solidi A **43**, 513 (1977).

Translated by H. Bronsteĭn

Technical Physics Letters, Vol. 26, No. 2, 2000, pp. 137–138. Translated from Pis'ma v Zhurnal Tekhnicheskoĭ Fiziki, Vol. 26, No. 4, 2000, pp. 5–8.

Characteristic Time of Instability Development in a Strongly Charged Low-Viscosity Droplet

S. O. Shiryaeva

Yaroslavl State University, Yaroslavl, 150000 Russia

Received October 11, 1999

Abstract—A nonlinear integral equation is derived and solved, which describes the time evolution of spheroidal deformations of a low-viscosity droplet unstable with respect to intrinsic charge. © *2000 MAIK "Nauka/Interperiodica".*

The question of the possibility of theoretical estimation of the characteristic time of instability development in a strongly charged droplet is of interest in view of numerous applications of this phenomenon in various fields of engineering physics and geophysics, as well as in view of the complexity of direct observation of the process of instability development under experimental conditions. In numerous experiments devoted to verification of the Rayleigh criterion of stability of a strongly charged droplet (see the references cited in [1]), the observers register only the initial and final states of the droplet. Theoretical estimates of the time of instability development in a strongly charged droplet of the ideal liquid were made in [2–4], when the characteristic time scale of the process of instability development was defined only by the features of interaction between the magnitude of deformation of the unstable droplet and the degree of supercritical droplet charging depending on the magnitude of deformation. The use of the same calculation technique and the same physical premises as in [2, 3], but with additional inclusion of the decrease (due to the effect of viscous decay) of the increment of instability of capillary motions of liquid in spherical and spheroidal droplets according to [5, 6], enables one to estimate the effect of viscosity as well.

1. The spectrum of capillary vibrations of an isolated droplet of a conducting liquid with radius R, charge Q, and surface tension σ is defined by the expression [7]

$$\frac{\omega^2}{n} = \frac{\sigma}{\rho R^3} n(n-1)[(n+2) - W], \qquad W = \frac{Q^2}{4\pi\sigma R^3}, \tag{1}$$

where n is the number of the capillary vibration mode and ρ is the liquid density. One can readily see from (1) that, at $W > 4$, the fundamental mode ($n = 2$) of capillary vibrations becomes unstable and the vibration amplitude ζ starts increasing with time as $\zeta \sim \exp(\gamma t)$, where

$$\gamma = \left\{ \frac{2\sigma}{\rho R^3}(W-4) \right\}^{1/2}.$$

If the liquid is not ideal and possesses a kinematic viscosity ν_0, and the droplet radius R, the liquid density ρ, and its surface tension σ are such that $\nu_0(\rho^{-1}\sigma^{-1}R)^{1/2} \ll 1$ (i.e., the droplet may be considered as possessing low viscosity), the capillary motions of the fundamental mode of the droplet likewise decay exponentially with the decrement

$$\eta_s = \nu\gamma k(W), \qquad k(W) \equiv \left[1 + \frac{4}{W+1} + \frac{1}{2(W-4)} \right]. \tag{2}$$

This formula, derived by approximating the results of numerical analysis of the dispersion equation obtained in [5], is valid at $\nu k(W) < 1$. Note that, at $W = 4$, the droplet is already unstable with respect to infinitely small surface deformations of the type $\zeta = \zeta_0 P_2(\cos\theta)$, which correspond to virtual excitation of the fundamental mode of capillary vibrations. The excitation of such capillary vibrations may be due to, for example, the thermal motion of molecules in the liquid. In this case, the amplitude of ζ_0 is defined by the expression $\zeta_0 = (\sigma/kT)^{1/2}$, where k is the Boltzmann constant and T is the absolute temperature of the liquid. The thermal excitation of a capillary wave $\sim P_2(\cos\theta)$ corresponds to virtual drawing of a droplet into a spheroid of eccentricity $e_0 = (3\zeta_0/R)^{1/2}$. However, for a spheroid, the value of the parameter W that is critical for realizing the instability of the droplet with respect to the intrinsic charge is a decreasing function of eccentricity [8]. In a linear (with respect to the square

of eccentricity e^2) approximation, this function has the form [8]

$$W = W_* = 4(1 - \alpha e^2). \quad (3)$$

Therefore, with $W = 4$ for a droplet that experienced a virtual (thermal) distortion of the form $\zeta = \zeta_0 P_2(\cos\theta)$, the amplitude of this perturbation will start increasing in time by the exponential law with the increment

$$\alpha_0 = \left\{\frac{8\sigma}{\rho R^3}\alpha e_0^2\right\}^{1/2}.$$

But the rise of the perturbation amplitude $\sim P_2(\cos\theta)$ corresponds to further drawing of the droplet, an increase in its eccentricity, and a decrease according to (3) in the critical value of instability and, consequently, leads to an increase in the instability increment.

At the same time, the presence of spheroidal deformation in the droplet results in dependence of the decrement of the fundamental mode decay on the magnitude of this deformation (on the square of eccentricity e^2), which has the following form according to the approximation of the results of numerical calculations performed in [6]:

$$\eta_{sd} = \eta_s\left[1 - \frac{2}{1 + 0.8\nu}e^2\right],$$

where η_s is defined by relation (2).

One can write the sequence of amplitudes of growing perturbations at close moments of time to derive a nonlinear integral equation describing the rise of dimensionless amplitude $X \equiv \zeta/R$ in time,

$$X(t) = X_0 \exp\left\{\lambda\int_0^t X(t)^{-1/2}\{aX(t)^2 + bX(t) - c\}dt\right\},$$

$$\lambda \equiv \left\{\frac{24\alpha\sigma}{\rho R^3}\right\}^{1/2}, \quad a \equiv 3\kappa(\nu)\nu, \quad (4)$$

$$b \equiv 1 - 3\nu + \frac{\kappa(\nu)\nu}{24\alpha}, \quad c \equiv \frac{\nu}{24\alpha}, \quad \kappa(\nu) \equiv \frac{6}{1 + 0.8\nu}.$$

A solution to this equation has the following form in the low viscosity approximation employed:

$$X(t) = X_0\left\{1 - \frac{1}{2}\lambda\delta(\nu)t\right\}^{-2}; \quad (5)$$

$$\delta(\nu) \equiv 1 - \nu\left[3 - \frac{1}{4\alpha(1 + 0.8\nu)}\right].$$

The obtained function $X(t)$, which describes the increase in time of the amplitude of spheroidal deformation of an unstable low-viscosity droplet, has qualitatively the same form as that for a droplet of the ideal liquid [2]. The only difference is the presence, in the viscous droplet case, of the factor $\delta(\nu) < 1$ for any permissible values of viscosity (which must be small, i.e., $\nu \ll 1$, because this fact was used in deriving expression (4)). For $\nu = 0$, we derive $\delta(\nu) = 1$, and relation (5) changes to the expression derived in [2] for the increase in time of spheroidal deformation of a droplet of the ideal liquid.

One can see that allowance for the viscosity leads to an increase by a factor of $\delta(\nu)$ in the characteristic time scale of the instability development as compared to the case of a droplet of nonviscous (ideal) liquid. Assuming for the dimensionless viscosity that $\nu = 0.1$ and taking that $\alpha = 1/3$ [2, 8], we obtain $\delta \approx 1.3$.

CONCLUSION

The obtained result is fairly obvious from the qualitative standpoint: it is *a priori* clear that the effect of viscosity must be manifested as an increase in the characteristic time of the instability development. But it is now possible for the first time to quantitatively estimate this phenomenon under conditions of a substantially nonlinear process of the rise in time of a very small thermal deformation of the shape of a droplet at the stability threshold.

REFERENCES

1. A. I. Grigor'ev and S. O. Shiryaeva, Zh. Tekh. Fiz. **61**, 19 (1991) [Sov. Phys. Tech. Phys. **36**, 258 (1991)].
2. S. O. Shiryaeva and I. D. Grigor'eva, Pis'ma Zh. Tekh. Fiz. **20**, 1 (1994) [Tech. Phys. Lett. **20**, 214 (1994)].
3. S. O. Shiryaeva, A. I. Grigor'ev, and I. D. Grigor'eva, Zh. Tekh. Fiz. **65**, 39 (1995) [Tech. Phys. **40**, 885 (1995)].
4. D. F. Belonozhko and A. I. Grigor'ev, Pis'ma Zh. Tekh. Fiz. **25**, 41 (1999) [Tech. Phys. Lett. **25**, 1 (1999)].
5. S. O. Shiryaeva, M. I. Munichev, and A. I. Grigor'ev, Zh. Tekh. Fiz. **66**, 1 (1996) [Tech. Phys. **41**, 635 (1996)].
6. S. O. Shiryaeva, Zh. Tekh. Fiz. **68**, 20 (1998) [Tech. Phys. **68**, 1 (1998)].
7. J. W. S. Rayleigh, Philos. Mag. **14**, 184 (1882).
8. A. I. Grigor'ev, Zh. Tekh. Fiz. **55**, 1272 (1985) [Sov. Phys. Tech. Phys. **30**, 736 (1985)].

Translated by H. Bronsteĭn

Technical Physics Letters, Vol. 26, No. 2, 2000, pp. 139–140. Translated from Pis'ma v Zhurnal Tekhnicheskoĭ Fiziki, Vol. 26, No. 4, 2000, pp. 9–13.

Nonlinear Hologram Recording on an Optically Controlled Transparency of the Glassy Chalcogenide Semiconductor–Liquid Crystal Type

A. N. Chaĭka and F. L. Vladimirov

Research and Technological Institute of Optical Materials Science, Vavilov State Optical Institute, All-Russia Research Center, St. Petersburg, 193171 Russia

Received October 5, 1999

Abstract—Realization of an optically controlled transparency possessing a nonlinear holographic modulation characteristic containing region with positive and negative slope is demonstrated to be feasible. The transparency filter is based on a glassy chalcogenide photoconductor–nematic liquid crystal structure. A tenfold drop in the diffraction efficiency over the negative-slope region was obtained in the experiment. © *2000 MAIK "Nauka/Interperiodica".*

Optically controlled transparency (OCT) based on a photoconductor–liquid crystal (PC–LC) structure is a key element of holographic data processing systems [1]. It is normally required that the modulation characteristic of an OCT (i.e., the diffraction efficiency η as a function of the recording light intensity I) contain a sufficiently long linear segment. However, holographic processors implementing fuzzy logic [2], which have been attracting serious attention lately, call for a nonlinear modulation characteristic. In some cases, the modulation characteristic must contain regions with positive and negative slopes.

This paper demonstrates that OCT modulation characteristics with both rising and pronounced falling regions can be realized.

We have studied the properties of a PC–LC based OCT representing a multilayer structure sandwiched between two glass substrates. Each substrate has a transparent conducting coating on the inner side, and one substrate also carries a photoconductive layer. Bounded by alignment coatings, the liquid-crystal layer is situated between the photoconductive layer and the other substrate. A spatial pattern or an image is projected onto the photoconductive layer. If a voltage is applied between the transparent conducting coatings, the PC layer transforms the illumination-intensity distribution into a potential distribution on the LC layer, which locally modifies the LC birefringence. This in turn results in a phase modulation of the readout light [3].

The photoconductor is a glassy chalcogenide semiconductor of the As–Se type with a thickness d_{PC} of 1 μm. The liquid crystal, which serves as a modulator, is a nematic liquid crystal of the ZhKM-1630B type with $\Delta n = 0.13$, $\Delta\varepsilon = +4.4$, $\Delta t = -20\ldots+90$°C, and a planar initial alignment. The thickness of the liquid-crystal layer is $d_{LC} = 10$ μm. The photoconductor had a sufficiently high specific dark resistance ($\rho_d = 10^{13}$ Ω cm) to match the conductances of the PC and LC layers of the structure (in view of the difference between their thicknesses) upon application of a dc voltage. The maximum phase modulation amplitude achieved is 4π.

Within the framework of the thin-phase-hologram model [4], the diffraction efficiency of the structure as a function of the phase modulation amplitude can be expressed using the Bessel function of an appropriate order:

$$\eta_m = J_m^2\left(\frac{\Delta\Phi}{2}\right),$$

where $\Delta\Phi = \Delta\Phi_{max}(I) - \Delta\Phi_0$ is the phase modulation amplitude, $\Delta\Phi_{max}(I)$ is the maximum phase delay for the recording light intensity I, and $\Delta\Phi_0$ is the phase delay at $I = 0$.

For a sufficiently large phase modulation amplitude ($\Delta\Phi > 2\pi$), the first-order diffraction efficiency, defined as the ratio of the intensity for first-order diffracted light to that for readout light, $\eta_1 = I_1/I_0$, and plotted as the function $\eta_1(\Delta\Phi)$, is nonlinear and has a rising and a falling region. The phase modulation amplitude is a complicated function of the parameters of the PC and LC layers, control voltage, the spatial frequency ν of the recorded grating, and the recording light intensity. Note that $\Delta\Phi$ is a monotonic function of I; therefore, the modulation characteristic can have a nonmonotonic shape with rising and falling segment regions, provided that the PC–LC structure parameters are appropriately selected.

Holograms were recorded at a wavelength of 633 nm. Readout was performed using a semiconductor laser operated at 814 nm. The effect of recording and optical control conditions on the first-order dif-

1063-7850/00/2602-0139$20.00

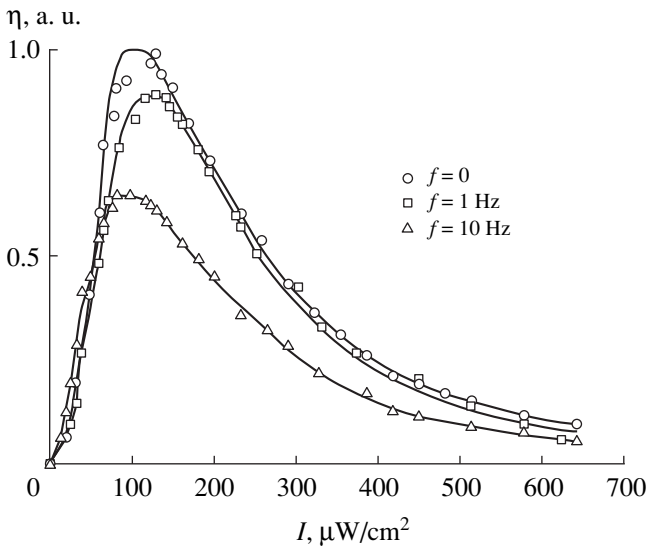

Fig. 1. Modulation characteristics of an As–Se based OCT with nematic LC powered with a dc or a pulsed voltage at a repetition frequency of 1 or 10 Hz.

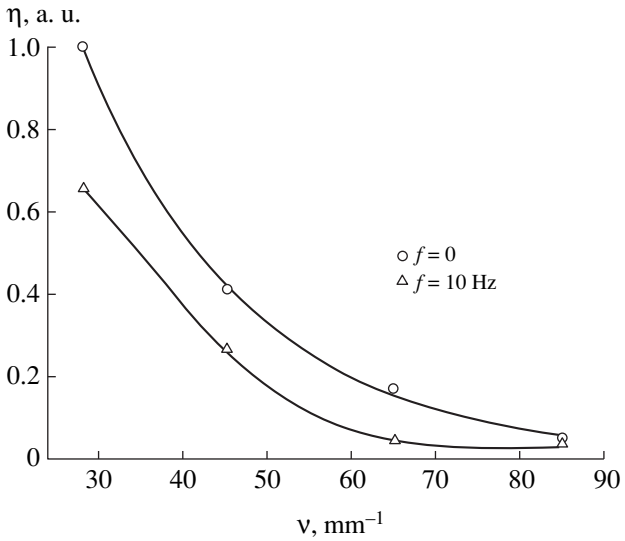

Fig. 2. Resolution of an As–Se based OCT with a nematic LC powered with a dc or a pulsed voltage.

fracted light intensity was investigated. The diffracted light intensity was measured with a photomultiplier having a pinhole aperture situated in the focal plane of an integrating objective lens. The diffraction efficiency was determined as the ratio of the light intensity in the first order of diffraction to that of the readout beam: $\eta = I_1/I_0$.

Figure 1 shows the modulation characteristics measured for an OCT powered with a dc or a pulsed voltage with repetition rate of 1 or 10 Hz. The spatial frequency of the recorded grating was 45 mm^{-1}. The curves exhibit a rising region 1–100 $\mu W/cm^2$ and a falling region extending from 100 to 700 $\mu W/cm^2$, in which the diffraction efficiency drops by more than one order of magnitude. The slope of the curve in both regions depends on the control voltage and can be varied over a wide range. This feature is important for implementation of the forward and inverse operators in the holographic processor.

Figure 2 depicts the plot of maximum diffraction efficiency versus spatial frequency of the grating. The measurement was carried out for the spatial frequencies $\nu = 28$–85 mm^{-1}. Note that $\eta \approx 16\%$ at $\nu = 28$ mm^{-1} and $\eta = 0.7\%$ at $\nu = 85$ mm^{-1}.

The operation speed of the structure is determined by the electrooptical response time of the liquid crystal and the time constant of the whole PC–LC structure [1]. Since the photoconductor has a large specific resistance, the time constant is as high as 200–500 ms. The experimental operation speed was usually 2–5 Hz when the structure was powered with a dc voltage and 10–15 Hz with a pulsed voltage.

ACKNOWLEDGMENTS

We are grateful to A.V. Pavlov for helpful discussions.

This study was funded by the Russian Foundation for Basic Research, project no. 98-02-18189.

REFERENCES

1. F. L. Vladimirov, A. N. Chaĭka, I. E. Morichev, *et al*., Opt. Zh., No. 7, 53 (1993).
2. A. V. Pavlov, in *Proceedings of International Conference on Soft Computing and Measurement, SCM'99* (St. Petersburg, 1999), Vol. 1, p. 218.
3. F. L. Vladimirov, A. N. Chaĭka, N. I. Pletneva, *et al*., Proc. SPIE **3490**, 432 (1998).
4. N. Mukohzaka, N. Yoshida, H. Toyoda, *et al*., Appl. Opt. **33**, 2804 (1994).

Translated by A. A. Sharshakov

Technical Physics Letters, Vol. 26, No. 2, 2000, pp. 141–142. Translated from Pis'ma v Zhurnal Tekhnicheskoĭ Fiziki, Vol. 26, No. 4, 2000, pp. 14–18.

Relativistic Resonance Traveling-Wave Tube with Tunable Oscillation Frequency

É. B. Abubakirov, A. N. Denisenko, A. V. Savel'ev, E. I. Soluyanov, and V. V. Yastrebov

Institute of Applied Physics, Russian Academy of Sciences, Nizhni Novgorod, 603600 Russia

Received August 5, 1999

Abstract—A high-power microwave oscillator is realized experimentally, employing a relativistic traveling-wave tube with a feedback circuit closed by tunable Bragg waveguide reflectors. A gigawatt-pulse power level is attained in the oscillator in the 3-cm wavelength range, which is maintained when the carrier frequency is tuned in a range of about 5%. *© 2000 MAIK "Nauka/Interperiodica".*

The search for the possibilities of tuning the carrier frequency of an output signal appears to be one of the most promising directions of investigation of microwave radiation sources employing relativistic electron beams [1–3]. Under conditions of pulsed operation of the radiation source, one possible way of such tuning is by varying the frequency from pulse to pulse, which may be accomplished by mechanical adjustment of the electrodynamic system of the oscillator. One of the versions of a device that permits mechanical tuning of the oscillation frequency may be based on the use of a relativistic resonance traveling-wave tube (TWT). The relativistic resonance TWT [4] is an oversize corrugated waveguide channeling a slow electromagnetic wave synchronous with the electron beam, and positive feedback is accomplished by Bragg-type resonant reflectors [5] mounted at the ends of this waveguide. The oversize dimension of the waveguide makes for a lower probability of its high-frequency breakdown with a high power of electromagnetic radiation. As to the coherence of the radiation, it is ensured by the reflectors, which are selective with respect to the wave frequency and type. In the case under treatment, the relativistic TWT, which operates in the slow wave mode of the oversize waveguide, has a sufficiently wide band; therefore, the tuning of the oscillator frequency may be achieved by shifting the operating frequency of the reflectors.

For the Bragg-type reflectors employed, the shift of the reflection band is realized when a controllable nonuniformity, for example, a phase jump of the side wall corrugation, is introduced in the reflector design. Note that, if the waveguide is round and the incident and reflected waves have different azimuth indexes (m_1 and m_2), the coupling reflector has a helical corrugation with the number of threads

$$\bar{m} = m_1 - m_2, \qquad (1)$$

and the phase jump in this corrugation is varied by simply turning one part of the reflector relative to another.

The operation of such a reflector may be analyzed, as for a regular version, using the coupled wave model. This analysis reveals that introduction of an irregularity in the corrugation in the middle of the reflector leads to the emergence in the reflection band of a frequency at which the waves reflected by two parts of the reflector fully compensate each other, so that the total reflection coefficient becomes zero. As the phase jump varies in the interval (0.2π), the compensation point travels from one boundary of the reflection band to the other, thereby deforming the band and varying the frequency position of maximum of the reflection coefficient (Fig. 1). For moderate values of the reflection coefficient (80–90%), the shift of the maximum is of the order of the undisturbed working band of the reflector.

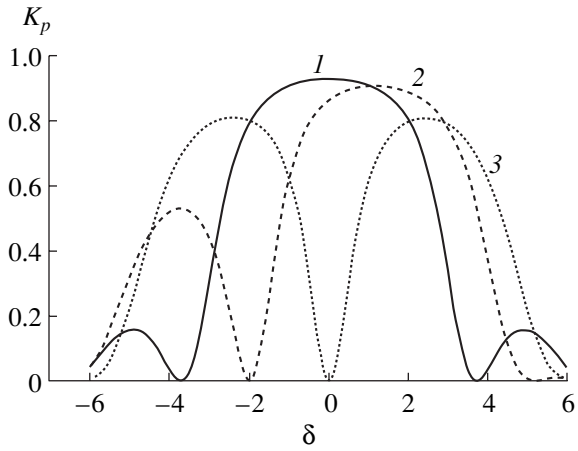

Fig. 1. Calculated values of the reflection coefficient K_p of a Bragg reflector as a function of the wave numbers h_1 and h_2 of interacting waves with $\delta = (2\pi/d - h_1 - h_2)/2$ (where d is the spatial period of the reflector) for different values of the corrugation phase shift: (*1*) 0°, (*2*) 90°, (*3*) 180°.

1063-7850/00/2602-0141$20.00 © 2000 MAIK "Nauka/Interperiodica"

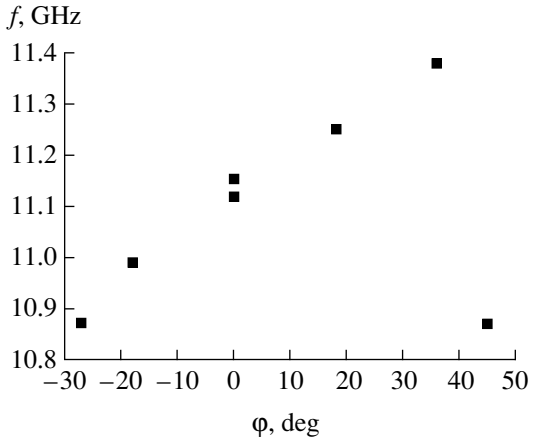

Fig. 2. The center oscillation frequency of a resonance TWT as function of the corrugation phase jump of the cathode reflector.

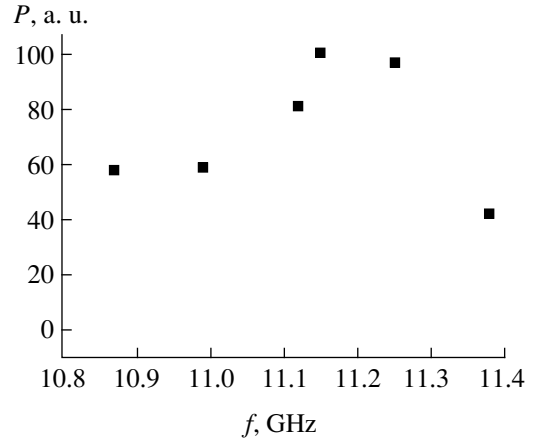

Fig. 3. The variation of the peak power of a resonance TWT during retuning of the carrier frequency.

The above-described possibility of controlling the operating frequency of a relativistic microwave oscillator was investigated experimentally. The experimental setup was based on the use of a resonance TWT with HE_{11} hybrid mode of a round corrugated waveguide and a feedback circuit closed by a TE_{41} wave. The coupling of waves was provided by two reflectors made in the form of waveguide segments with a five-thread helical corrugation. The cathode reflector was divided lengthwise into two equal parts capable of rotating relative to each other. The maximum coefficient of transformation of the cathode reflector was 90%; and that of the collector reflector, 10%. The operating modes had rotatory polarization, with the fundamental mode and the feedback mode having opposite directions of rotation of their spatial structures. The choice of the types of modes and their polarization was defined by the need to provide for a single-mode oscillation.

The oscillator power supply was provided by a high-current electron accelerator with a particle energy of 1–1.2 MeV, beam current of about 7 kA, and an accelerating pulse duration of 150 ns at the 0.8 amplitude level. The accelerator shaped a tubular electron beam 38 mm in diameter, which was transported by a uniform magnetic field of 2 T. The output radiation was extracted by diffraction using an oversize horn antenna via a polyethylene window 440 mm in diameter. The output microwave radiation diagnostics involved the use of a set of calibrated microwave sensors placed at a distance of 4 m from the outlet window. The gain factor of the "outlet window–receiving horn of microwave sensor" line was determined in preliminary experiments using standard measuring equipment. The radiation frequency was measured by a waveguide bandpass filter with mechanical tuning of the center frequency of the transmission band.

In a regular version, a resonance TWT of this type generated microwave radiation with a peak power of about 1.5 GW, a duration of 30–40 ns, and a carrier frequency of 11.1 GHz [4].

In tuning the cathode reflector by varying the relative phasing of its parts, the center frequency of oscillations shifted within 10.9–11.4 GHz (Fig. 2) when the output power varied by a factor of not more than two (Fig. 3).

Therefore, the proposed method enables one to perform mechanical tuning of the frequency of high-power microwave oscillators to within several percent, with the basic performance of the instrument remaining unaffected.

REFERENCES

1. G. Nusinovich, B. Levush, T. Antonsen, *et al.*, in *Proceedings of Second International Workshop on Strong Microwaves in Plasmas, Nizhni Novgorod, Russia, 1994* (Institute of Applied Physics, Nizhni Novgorod, 1994), Vol. 2, p. 712.
2. L. Brown, A. Maitland, and D. M. Parkes, in *Abstracts of EUROEM 94 International Symposium, Bordeaux, France, 1994*, p. TUa-01-10.
3. L. D. Moreland, E. Shamiloglu, S. D. Korovin, *et al.*, IEEE Trans. Plasma Sci. **24**, 852 (1996).
4. É. B. Abubakirov, M. I. Fuchs, V. A. Gintsburg, *et al.*, in *Proceedings of Eighth International Conference on High-Power Particle Beams* (World Scientific, 1991), Vol. 2, p. 1105.
5. G. G. Denisov and M. G. Reznikov, Izv. Vyssh. Uchebn. Zaved. Radiofiz. **25**, 562 (1982).

Translated by H. Bronsteĭn

Technical Physics Letters, Vol. 26, No. 2, 2000, pp. 143–145. Translated from Pis'ma v Zhurnal Tekhnicheskoĭ Fiziki, Vol. 26, No. 4, 2000, pp. 19–24.

The Acoustic Properties of TiNiMoFe-Based Alloys

V. É. Gyunter, V. I. Chernyshev, and T. L. Chekalkin

Research Institute of Medical Materials and Implants with Plastic Memory, Tomsk, Russia

Received October 8, 1999

Abstract—A study is made of the laws of variation of the acoustic properties of TiNi-based alloys depending on the alloy composition and the temperature. It is demonstrated that, in the temperature range of existence of the *B*2 phase and the possible strain-induced martensite formation, the vibrations of TiNiMoFe differ from those of conventional materials. Upon excitation of spontaneous vibrations in the $M_f \le T \le M_d$ range, there appears a region of long-term, small-amplitude low-frequency sound vibrations. It is found that free low-frequency vibrations of a sample of TN-10 alloy [1] are characterized by a low level of decrement in the above-indicated temperature range. © *2000 MAIK "Nauka/Interperiodica".*

Alloys with plastic (shape) memory find extensive application for solving numerous problems in medicine and engineering.

When used in medicine as materials and structures implanted into the human organism, TiNi-based alloys are subjected to an alternating-sign action of both the organism and environment. The effect of the environment causes the excitation of vibrations of a wide spectrum of waves inside the tissues of the organism and in the implant material [1]. Phase transitions in the TiNi-based alloys have a considerable effect on their physical and mechanical properties in a wide temperature range. Depending on the alloy composition and its thermomechanical treatment, the acoustic properties of TiNi alloys exhibit a spectrum of unusual phenomena. This follows from the literature describing the studies of the acoustic properties of these alloys [2–4]. We have investigated the laws of variation of the acoustic properties of TiNi-based alloys in the vicinity of the temperature range of martensite transformations.

Investigations were performed using samples of a TN-10 titanium nickelide-based alloy shaped like a tuning fork. The vibrations arising in a sample after excitation were registered by a high-sensitivity microphone whose frequency range coincided with the frequency range of sample oscillations defined experimentally using an oscillograph. The analog signal was applied to the input of an amplifier. After amplification, the signal was delivered to the input of an ADC (analog-to-digital converter) of a PC. The digitized signal was processed according to a Fourier transform based on the behavior of the entropy maximum in accordance with the procedure of Sarychev [5]. The Origin® application software was used to graphically treat the data.

Figure 1 shows a time variation of the amplitude of free vibrations of a tuning fork made of the TN-10 alloy. In the initial period, the vibrations are quasi-harmonic, with the vibration amplitude varying approximately logarithmically. From certain moment of time, the vibration amplitude remains almost constant, while the period of vibrations decreases. Characteristic beats may be observed in the entire course of the vibration process. The vibrational system behaves as if a driving force that sustains vibrations over a long period of time is present.

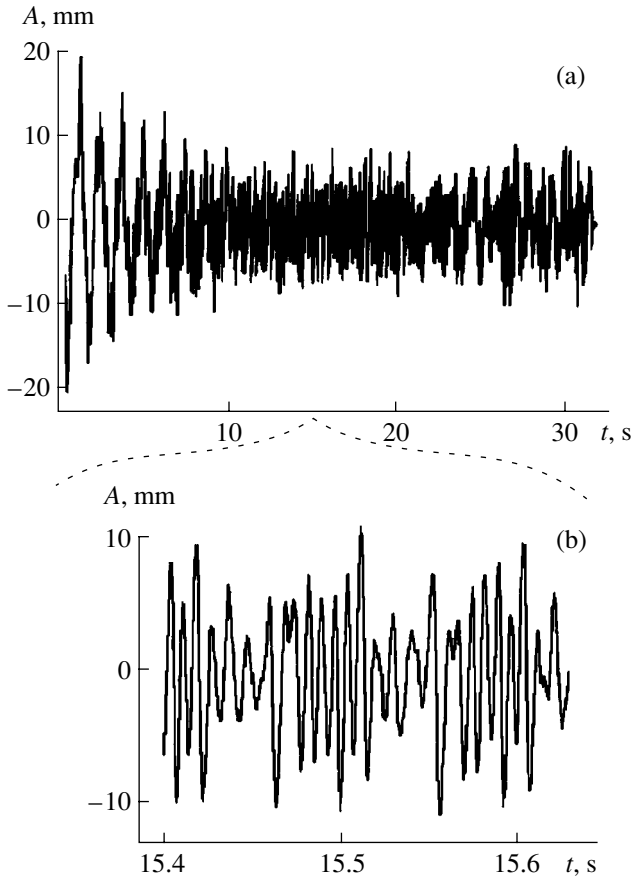

Fig. 1. Time diagram of free vibrations in a sample of TN-10 alloy.

1063-7850/00/2602-0143$20.00 © 2000 MAIK "Nauka/Interperiodica"

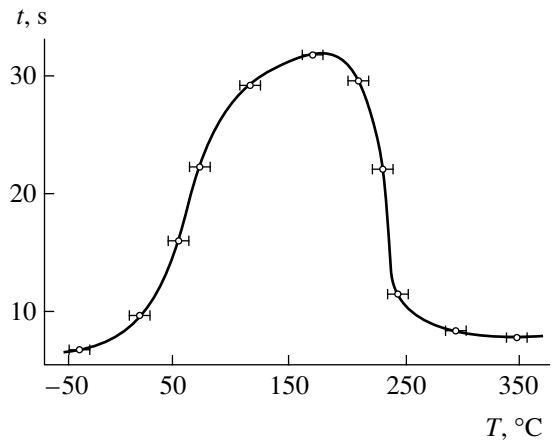

Fig. 2. The temperature dependence of the duration of vibrations in a sample of TN-10 alloy.

The stability of the vibration amplitude and the presence of beats indicate that the driving force frequency is in the vicinity of one of the lower harmonics displaced in phase through a small angle.

The phenomenon may be explained in view of the fact that this alloy occurs in a premartensite state. A vibrational system displaced from the state of equilibrium and allowed to move freely must return to the state of equilibrium or to a different state if several stable states correspond to the preset conditions. The transition of the TiNi system from the pretransition state *B*2 to the state *B*19' and back makes up a complete vibrational cycle. In so doing, the dissipation of vibrational energy is defined by the entire combination of relaxation processes occurring during periodic deformation of crystals of the *B*2 phase and martensite and, therefore, it does not appear possible to mathematically describe this dissipation process in the general form [6]. However, it is to be taken into account that heat release is one of the determining factors of the martensite reaction. According to some data [1], the amount of heat released during the $B2 \longrightarrow B19'$ transition exceeds 8.3 kJ/mol. The same amount of heat is absorbed by the system during the inverse transition $B19' \longrightarrow B2$. Under conditions of a system in which the thermal conductivity of TiNi is extremely low and amounts to 1 W/(m K) [1], thermal processes play an important part in the course of vibrations, in particular, if the vibrations occur under adiabatic conditions (when the heat is released upon the formation of martensite and absorbed with the appearance of the *B*2 phase, so that no excess heat is removed to the ambient medium).

The formation of martensite at a temperature above M_S under load is described [7] by the following relationship: $\Delta\sigma = \Delta H \Delta T / T_0 \varepsilon_m$, where $\Delta\sigma$ is the applied stress, ΔT is the temperature variation, $T_0 = (M_S - M_d)/2$ is the temperature of phase equilibrium, ΔH is the latent heat of transition, and ε_m is the deformation due to the martensite reaction.

For the individual *i*th martensite plate or the microdomain of a high-temperature phase, the equation will have the form [7]

$$\Delta\sigma_i = \pm\frac{\Delta H_i \Delta T_i}{T_{0i}\varepsilon_{M_i}}, \quad (1)$$

where the sign ± is taken with due regard for the release or absorption of heat.

However, if the formation of the individual *i*th martensite plate is associated with the application of load $\Delta\sigma$, an increase in the temperature by $\Delta T_i'$ leads to the emergence of stress of opposite sign,

$$\Delta\sigma_i = \frac{\Delta T_i' c \varepsilon_{M_i} \Delta T_i'}{T_{0i}\varepsilon_{M_i}}, \quad (2)$$

where *c* is the specific heat.

Equating (2) and (1), we may derive the conditions for a continuously vibrating system (disregarding other relaxation processes),

$$\frac{(\Delta T_i')^2 c}{T_{0i}\varepsilon_{M_i}} = \frac{\Delta H_i \Delta T_i}{T_{0i}\varepsilon_{M_i}}, \quad (\Delta T_i')^2 = \frac{\Delta H_i \Delta T_i}{c}.$$

With the proviso that $\Delta T_i' = \Delta T_i$, we derive

$$\Delta T_i' = \pm\frac{\Delta H_i}{c}.$$

An analysis of the latter expression reveals the condition of equilibrium of the system under adiabatic conditions, when the release of the latent heat of transition due to the formation of martensite plates leads to local heating, i.e., to the emergence of a thermal front that is the driving force of the inverse transition. One can expect that, upon initiation of low-frequency spontaneous vibrations in TiNi-based alloys (sound frequency range) in the temperature range in which the strain-induced martensite formation is possible (i.e., in the $M_f \le T \le M_d$ range), the vibrations in a TiNi-based system will be characterized by a longer decay time.

We have investigated time variation of free vibrations in the alloy (Fig. 1) and obtained results supporting the above conclusion. An unusual behavior of alloy samples is observed in the M_f–M_d temperature range, which consists in an anomalous increase in the time of system vibration. On the contrary, in the martensite state the vibrations are almost fully suppressed. A distinguishing feature of these correlations is the existence of a region of long-term low-frequency sound vibrations with small amplitude [8]. The appearance of such a region or "plateau" in the time diagram is associated with the alternating-sign effect of martensite reactions in a two-phase state on the initiation of oscillations by external stress. Figure 2 gives the temperature dependence of the duration of vibrations for the TN-10 alloy studied.

We may ascertain that a vibrational system manufactured from TN-10 alloy is characterized by an anomalously high duration of vibrations in the M_f–M_d temperature range, that is, in the region of initiation of a two-phase state.

The low level of decrement in titanium nickelide-based alloys is mainly due to a high mobility of interfaces (between the martensite and high-temperature phases) and to a high value of the enthalpy of transformation providing for the presence of a thermal front at a low specific thermal conductivity of the alloy.

It is for the first time that the effect of an "undamped" region of low-frequency sound vibrations of small amplitude was observed in metal systems; this effect opens unexpected possibilities for the development of devices with new properties.

REFERENCES

1. V. É. Gyunter, G. Ts. Dombaev, *et al.*, *Medical Materials and Implants with Plastic Memory* (Tomsk State University, Tomsk, 1998).
2. W. J. Buchler and R. C. Wiley, NOLTR 61-75 Report (AD 266607) (US Naval Ordnance Laboratory, 1961).
3. R. R. Hasiguti and K. Iwasaki, NOLTR 68-16 (US Naval Ordnance Laboratory, 1968), p. 401.
4. D. Bradley, J. Acoust. Soc. Am. **37**, 700 (1975).
5. V. T. Sarychev, *Spectral Estimation Using the Maximum Entropy Methods* (Tomsk State University, Tomsk, 1994), p. 225.
6. V. É. Gyunter, A. N. Matyunin, and L. A. Monasevich, Implant Pamyat'yu Formy, No. 1, 42 (1993).
7. V. É. Gyunter, V. V. Kotenko, N. Z. Mirgazizov, *et al.*, *Alloys with Plastic Memory in Medicine* (Tomsk State University, Tomsk, 1986).
8. V. É. Gyunter, V. I. Chernyshev, and T. L. Chekalin, in *Proceedings of International Conference on Superelastic Materials and Implants with Plastic Memory in Medicine* (Tomsk State University, Tomsk, 1998), p. 411.

Translated by H. Bronsteĭn

Technical Physics Letters, Vol. 26, No. 2, 2000, pp. 146–149. Translated from Pis'ma v Zhurnal Tekhnicheskoĭ Fiziki, Vol. 26, No. 4, 2000, pp. 25–30.

The Magnetic and Magnetooptical Properties of Fe/Ti, Zr, Pt and Fe/Ti, Zr, Pt/Fe Thin-Film Magnetic Structures

E. E. Shalygina, M. A. Karsanova, and L. V. Kozlovskiĭ

Moscow State University, Moscow, 119899 Russia

Received October 8, 1999

Abstract—The results of investigation of the magnetic and magnetooptical properties of two-layer Fe/Ti, Zr, Pt and three-layer Fe/Ti, Zr, Pt/Fe thin-film magnetic structures are presented. The nonmagnetic layer exhibits a strong effect on the magnetic properties of samples. The magnitude of the saturation field of three-layer magnetic structures oscillates as a function of thickness of the nonmagnetic layer; the period of this oscillation depends on the thickness of the Fe layer. The Pt layer strongly affects the spectral dependences of the equatorial Kerr effect in the structures investigated. © *2000 MAIK "Nauka/Interperiodica".*

Investigation of the magnetic anisotropy, processes of magnetization reversal, and magnetooptical properties of thin-film magnetic structures is important from both the scientific and practical standpoints. The data obtained from investigations of the effect of the thickness and composition of magnetic and nonmagnetic layers on the magnetic and magnetooptical properties of two- and three-layer magnetic structures may be used in developing new thin-film systems for modern spin microelectronics. The objective of this work was to investigate the magnetic and magnetooptical properties of Fe/Ti, Zr, Pt and Fe/Ti, Zr, Pt/Fe thin-film structures.

The samples were prepared by magnetron sputtering. After adhesion at a temperature T = 150°C, the base pressure in the vacuum chamber was 10^{-9} Torr. The pressure of the working gas (argon) was ~10^{-4} Torr. In two-layer structures, the magnetic layer thickness t_{Fe} varied from 2 to 100 nm and that of the nonmagnetic layer (NML) applied between the magnetic film and the substrate, t_1, varied from 0 to 20 nm. In three-layer structures, t_{Fe} and t_1 varied from 2.5 to 10 nm and from 0.5 to 4 nm, respectively. In order to avoid oxidation, the samples were coated with a 10-nm layer of carbon.

The magnetic and magnetooptical properties of the samples were studied by measuring the equatorial Kerr effect (EKE) δ using a magnetooptical magnetometer and a spectral magnetooptical facility described in [1, 2]. Here, $\delta = (I - I_0)/I_0$, where I and I_0 denote the intensity of light reflected from magnetized and nonmagnetized samples, respectively. The external magnetic field was applied in the film plane in the direction normal to the plane of light incidence. The dispersion dependences of EKE were measured in the region of energies of the incident light quanta of $1.5 < \hbar\omega < 4.2$ eV. The angle of light incidence on the sample was 65°. All measurements were performed at room temperature.

As revealed by preliminary measurements, all samples are characterized by planar magnetic anisotropy; i.e., the axis of easy magnetization (AEM) lies in their plane. The hysteresis loops along the AEM for two-layer samples were almost rectangular in shape. The remanent-to-saturation magnetization ratio (M_R/M_S) varied from 0.95 to 0.98. The value of M_R/M_S increased as the iron layer thickness decreased.

Figure 1 shows the saturation field H_S of the two-layer samples as a function of the thickness of (a) the Fe film and (b) the nonmagnetic layer for a fixed value of t_1 and t_{Fe}, respectively. Figures 1c and 1d present typical dependences of the saturation field H_S on the thickness of the nonmagnetic layer for Fe/NML/Fe three-layer structures with fixed values of the thickness of iron film.

One can see in Fig. 1a that, with a fixed value of t_1, the value of H_S grows when t_{Fe} increases up to 35 nm and then drops as t_{Fe} varies from 40 to 100 nm. With a fixed value of t_{Fe}, the saturation field has a maximum at $t_{Zr} \approx 3$ nm and $t_{Ti,\,Pt} \approx 10$ nm (Fig. 1b). The value of H_S for samples with a Ti layer exceeds that for samples with Zr and Pt layers (Figs. 1a, 1b). Note that the behavior of coercive force H_C as a function of t_{Fe} and t_1 in two-layer samples coincides with $H_S(t_{Fe})$ and $H_S(t_1)$. The obtained results may be interpreted using the data of the structure analysis of samples. X-ray diffraction analysis reveals that the two-layer samples studied possess a polycrystalline structure with preferred {111} texture parallel to the sample surface. The degree of texturization of samples depended on the thickness of the Fe film, as well as on the thickness and composition of the NML. It is known [3] that more textured samples are characterized by a higher saturation field and a higher coercive force. It was this very correlation that we observed between the magnetic and structural properties in the two-layer samples studied.

1063-7850/00/2602-0146$20.00 © 2000 MAIK "Nauka/Interperiodica"

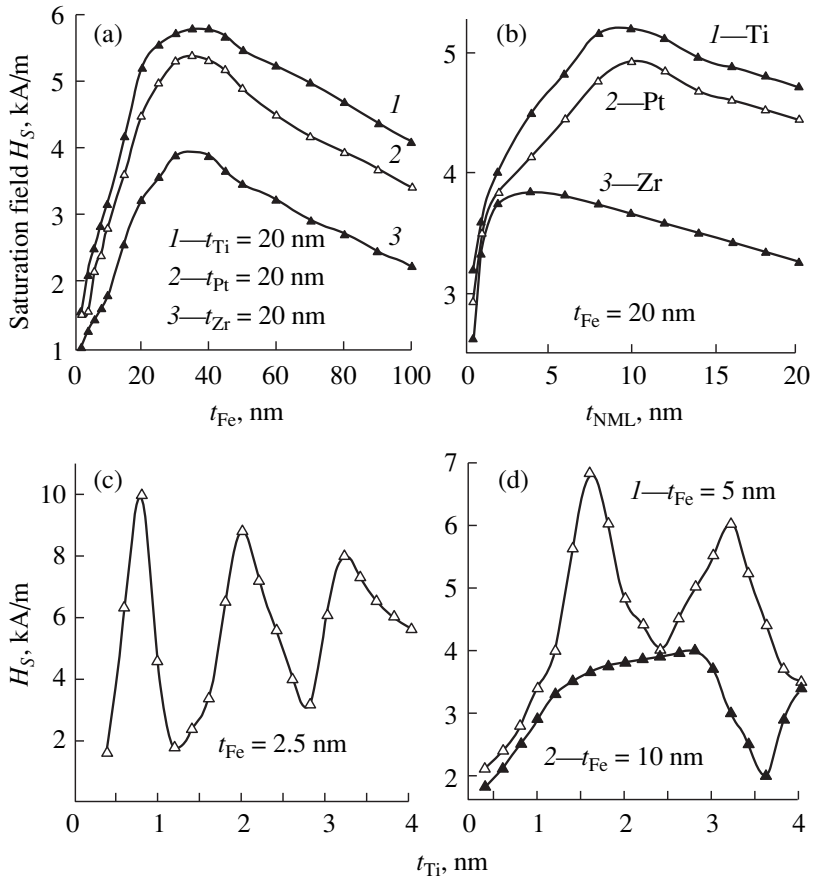

Fig. 1. Plots of the saturation field H_S of (a, b) two-layer Fe/Ti, Pt, Zr and (c, d) three-layer Fe/Ti/Fe samples versus the thickness of Fe film and nonmagnetic layer (for fixed values of the thickness of nonmagnetic and magnetic layers, respectively): (a) $H_S(t_{Fe})$ at t_1 = 20 nm, (b) $H_S(t_1)$ at t_{Fe} = 20 nm, (c) $H_S(t_{Ti})$ at t_{Fe} = 2.5 nm, and (d) $H_S(t_{Ti})$ at t_{Fe} = 5 and 10 nm (curves *1* and *2*, respectively).

Figures 1c and 1d show that the saturation field of Fe/Ti/Fe three-layer samples oscillates as a function of t_1, and the period of this oscillation Λ depends on t_{Fe}. In particular, Λ is equal to ~1.2 and 2 nm at t_{Fe} = 2.5 and 5 nm, respectively. Analogous measurements for other three-layer structures demonstrated that in samples with a Zr layer the value of Λ almost coincides with the values given above, while for samples with a Pt layer, Λ is equal to 0.8, 1.2, and 2 nm at t_{Fe} = 2.5, 5, and 10 nm, respectively. These results may be attributed to the existence of exchange interaction between ferromagnetic layers through the nonmagnetic layer and to its oscillatory behavior due to variation of t_1 [4, 5]. Moreover, the results of calculations performed by Nordström *et al.* [6] demonstrated that the value of Λ must increase with the magnetic layer thickness. We did observe experimentally such a variation of Λ.

Figure 2a gives a typical dispersion curve for the EKE in two-layer samples with different values of iron film thickness and with a fixed value of t_1 measured at $H = H_S$. These data were used to derive the dependence of the EKE on t_{Fe} for fixed values of $\hbar\omega$ (Fig. 2b). One can see in Figs. 2a and 2b that the value of EKE depends on the thickness of the Fe film. The EKE increases linearly with t_{Fe} up to ~20 nm and, at t_{Fe} > 20–25 nm, the EKE has a constant value. Therefore, the EKE is defined by magnetization of the surface layer of some critical thickness t_{cr}. The value of t_{cr}, starting with which the EKE has a constant value, is usually referred to as the information depth of the magnetooptical signal t_{inf} [7]. For samples with Ti and Zr layers, it was found that $t_{inf} \approx 21$ and 23 nm for $\hbar\omega$ = 3.4 and 1.7 eV, respectively.

Analogous measurements were performed for two- and three-layer magnetic structures with a Pt layer. In this case, the correlation between $\delta(\hbar\omega)$ and t_{Pt} proved to be more complex (Figs. 2c, 2d). An analysis of these data reveals that, as t_{Pt} increases, the peak in the region of the energy of incident light quanta of 1.8–1.9 eV, characteristic of the spectral dependence of the EKE of bulk iron, decreases and a new peak emerges in the ultraviolet region. By analogy with [8], this behavior may be attributed to spin polarization and exchange splitting of the 5*d*-levels of platinum. Because of a high spin-orbital energy of the 5*d*-states of platinum, the band structure of Fe varies: excited states arise, which

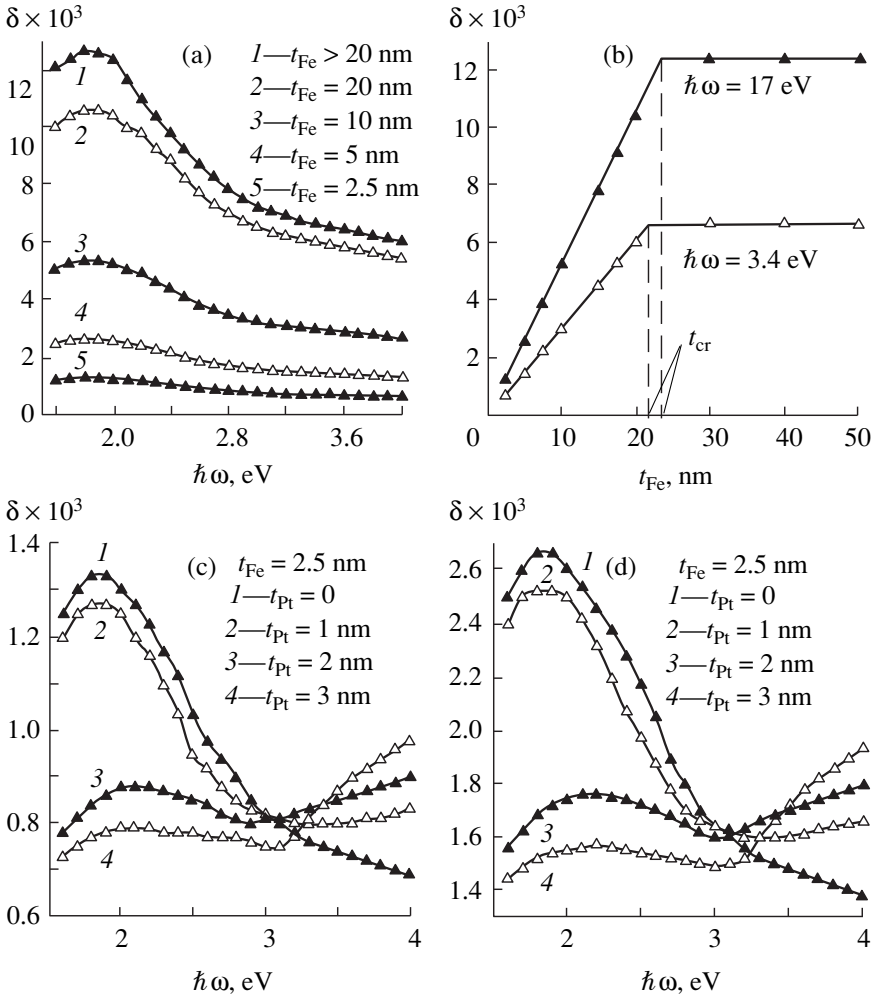

Fig. 2. The dispersion curves of the EKE for two-layer and three-layer structures: (a) for Fe/20-nm Ti structures with different thicknesses of the Fe layer; (c) for Fe/Pt; (d) for Fe/Pt/Fe structures with fixed thickness of the Fe layer and different thicknesses of the Pt layer; (b) the plot of the EKE versus the Fe film thickness for fixed values of the energy of incident light quanta.

are due to overlap of the 3*d*- and 5*d*-electron wave functions in the neighboring Fe and Pt layers. As a result, the dispersion curves of the EKE in these samples are modified. Evidently, this electron interface effect must depend on the thickness of both Fe and Pt layers. Moreover, according to the above data, the EKE may depend on the entire sample thickness t as well, if $t < t_{inf}$. Figures 2c and 2d demonstrate that, for the same thickness of the Fe layer, the value of EKE in three-layer structures exceeds (by a factor of approximately two) that in two-layer structures. The effect of a Pt layer on the EKE increases with its thickness. This increase continues until $t_{Pt} \approx 4$–4.5 nm. A quantitative comparison of the EKE values in two- and three-layer structures reveals that the effect of Pt on the EKE is higher in the case of three-layer structures, which is due to the presence of two Fe/Pt interfaces in these samples. It is found that the effect of Pt on the EKE in three-layer samples with t_{Fe} = 5 and 10 nm remains almost the same as in samples with t_{Fe} = 2.5 nm.

So, the magnetic and magnetooptical properties of Fe/Ti, Zr, Pt and Fe/Ti, Zr, Pt/Fe thin-film structures were investigated and dependences of the magnetic characteristics of the samples on the thickness and composition of nonmagnetic layer were determined. The obtained data were attributed to the structural features of two-layer samples and to the presence of exchange interaction between ferromagnetic layers via NML in three-layer systems. The dependence of the EKE on the thickness of the Fe film was found. A strong effect of the Pt layer on the EKE spectra of Fe/Pt and Fe/Pt/Fe thin-film structures was observed. This fact was attributed to exchange-induced polarization of the 5*d*-levels of platinum.

ACKNOWLEDGMENTS

This study was supported by the Russian Foundation for Basic Research, project no. 99-02-16595.

REFERENCES

1. G. S. Krinchik, E. E. Shalygina, O. P. Akhmatova, *et al.*, Fiz. Tverd. Tela (Leningrad) **28**, 2862 (1986) [Sov. Phys. Solid State **28**, 1605 (1986)].
2. G. S. Krinchik, E. E. Shalygina, and Sh. V. Égamov, Zh. Éksp. Teor. Fiz. **74**, 714 (1978) [Sov. Phys. JETP **47**, 375 (1978)].
3. C. J. Lin, G. L. Gorman, C. H. Lee, *et al.*, J. Magn. Magn. Mater. **93**, 194 (1991).
4. S. P. Parkin, R. Bhadra, and K. P. Roche, Phys. Rev. Lett. **66**, 2152 (1991).
5. P. Bruno, Phys. Rev. B: Condens. Matter **52**, 411 (1995).
6. L. Nordström, P. Lang, R. Zeller, *et al.*, Phys. Rev. B: Condens. Matter **50**, 13058 (1994).
7. G. Traeger, L. Wensel, and A. Hubert, Phys. Status Solidi **131**, 201 (1992).
8. D. Weller, W. Reim, and K. Spröl, J. Magn. Magn. Mater. **93**, 183 (1991).

Translated by H. Bronsteĭn

Technical Physics Letters, Vol. 26, No. 2, 2000, pp. 150–152. Translated from Pis'ma v Zhurnal Tekhnicheskoĭ Fiziki, Vol. 26, No. 4, 2000, pp. 31–36.

Calculation of the Surface Temperature of Liquid under Conditions of Combined Heat and Mass Transfer

A. R. Dorokhov and V. S. Loginov

Tomsk Polytechnical University, Tomsk, 634050 Russia

Received March 24, 1999; in final form, September 8, 1999

Abstract—A relationship is derived for the calculation of the surface temperature of a layer of liquid in the process of combined heat and mass transfer. It is demonstrated that, in the case of similarity of the laws of heat and mass transfer, this temperature is constant. The results of numerical and analytical calculations of the surface temperature of a layer of liquid are compared, and the conditions of validity of the calculation formulas based on the small contact time approximation are determined. *© 2000 MAIK "Nauka/Interperiodica".*

Calculations of the processes of combined heat and mass transfer are based on solving the energy and diffusion equations in a stationary [1, 2] and nonstationary [3] formulation. In so doing, the conditions of thermodynamic equilibrium and the balance of heat and mass fluxes are written for the liquid–gas interface. For definiteness, we will treat combined heat and mass transfer in a thin layer of an aqueous lithium bromide solution, on the surface of which the absorption of water vapor occurs. We will use a rough approximation of the equation of state for a solution in the form of a linear function (provided the pressure is constant, i.e., p = const),

$$C = dT + b, \tag{1}$$

where d and b are constant coefficients.

According to (1), the equality

$$C_n = dT_n + b \tag{2}$$

will be valid on the surface of the solution layer, where T_n and C_n respectively denote the absorbent temperature and concentration on the surface.

Consider the condition of balance for the heat and mass fluxes on the solution surface

$$q = r_a g_n, \tag{3}$$

where r_a is the specific heat of absorption.

We will define the fluxes of heat q and mass g_n by the relations

$$q = \alpha(T_n - T_o) \tag{4}$$

and

$$g_n = \rho\beta(C_n - C_o), \tag{5}$$

where α and β are the coefficients of heat and mass transfer and ρ is the density of liquid. The subscript "0" corresponds to the initial parameters of the solution.

According to the equation of state (1), the initial concentration of the solution defines the thermodynamically equilibrium temperature

$$T_s = \frac{C_o - b}{d} \tag{6}$$

and, accordingly, the concentration

$$C_s = dT_o + b. \tag{7}$$

Substituting expressions (5) and (4) into (3) and expressing the concentrations in accordance with the equation of state (1), we obtain

$$\alpha(T_n - T_o) = r_a\rho\beta d(T_n - T_s). \tag{8}$$

Let us write expression (8) in the form

$$\frac{T_n - T_s}{T_n - T_o} = \frac{\mathrm{Nu}}{\mathrm{Nu}_D}\frac{\mathrm{Lu}}{K_a}. \tag{9}$$

Here, dimensionless parameters are used: namely, $\mathrm{Nu} = \frac{\alpha L}{\lambda}$ is the Nusselt number for heat transfer; $\mathrm{Nu}_D = \frac{\beta L}{D}$ is the Nusselt diffusion number; $\mathrm{Lu} = \frac{a}{D}$ is the Lewis number; $K_a = \frac{rd}{c_p}$ is an analog of the criterion of phase transformation; a, D, λ, and c_p are the coefficients of thermal diffusivity, diffusion, thermal conductivity, and heat capacity of the liquid, respectively; and L is the characteristic linear dimension.

Denoting $\psi = \mathrm{NuLu}/(\mathrm{Nu}_D K_a)$ and resolving (9) relative to the surface temperature, we obtain

$$T_n = \frac{T_s - \psi T_o}{1 - \psi}. \tag{10}$$

According to (10), the surface temperature of liquid under conditions of combined heat and mass transfer is

defined by the values of thermodynamically equilibrium temperature T_s determined by the initial concentration c_o of the solution, initial temperature T_0 of the liquid, and by the ratio ($\mathrm{Nu}/\mathrm{Nu}_D$).

The value of the coefficient ψ is determined most easily at small values of the contact time, when the relations

$$\alpha = \frac{\lambda}{\delta_t}, \quad \beta = \frac{D}{\delta_D} \tag{11}$$

are valid for the calculation of the coefficients of heat and mass transfer, where $\delta_t = \sqrt{\pi a \tau}$ and $\delta_D = \sqrt{\pi D \tau}$ denote the "depth" of penetration of heat "wave" and concentration "wave," respectively, and τ is the current time.

In this case, we obtain that $\psi = \sqrt{\mathrm{Lu}}/K_a$ and, according to (10), the value of the surface temperature T_n does not depend on the process time. Here, the formula for the calculation of the surface temperature coincides with that obtained previously [1, 2]. We will treat the case of water vapor absorption by an aqueous lithium bromide solution at a water vapor pressure of 1 kPa. The values of parameters appearing in formula (10) are as follows: $d = -5.3 \times 10^{-3}$, $b = 0.6431$, $c_0 = 0.405$, $T_s = 44.9$°C, $K_a = 7.43$, $\mathrm{Lu} = 72.7$, and $\psi = 1.148$. For $T_0 = 32$°C, we obtain $T_n = 38.0$°C.

The very fact of establishing some constant value of the surface temperature is of great interest, because it is indicative of synchronization of the processes of heat and mass transfer. Consequently, in calculating the corresponding regularities of heat and mass transfer, it is sufficient to introduce constants that are readily derived by substituting (10) into (4). However, under conditions of a rapid drop of the surface temperature from the initial value corresponding to the thermodynamically equilibrium state of the solution (44.9°C) to a steady-state value (38°C in the treated example), this process may affect the values of the coefficients of heat and mass transfer. This effect was investigated in [4] during numerical analysis of the process of nonstationary film condensation.

In order to determine the conditions of applicability of the model of small contact time to the calculation of combined heat and mass transfer, a numerical calculation of the process of water vapor absorption by a layer of aqueous lithium bromide solution was performed. An implicit calculation scheme was employed, based on the method of trails [5]. The numerical calculation results were compared with those of the calculation of the heat transfer coefficient by the first formula in (11), which was given as

$$\mathrm{Nu} = 0.594\mathrm{Fo}^{-0.5}. \tag{12}$$

Here, $\mathrm{Fo} = \alpha\tau/L^2$ is the Fourier number.

As a result of substitution of the surface temperature (10) into (4) and some transformations, we derive

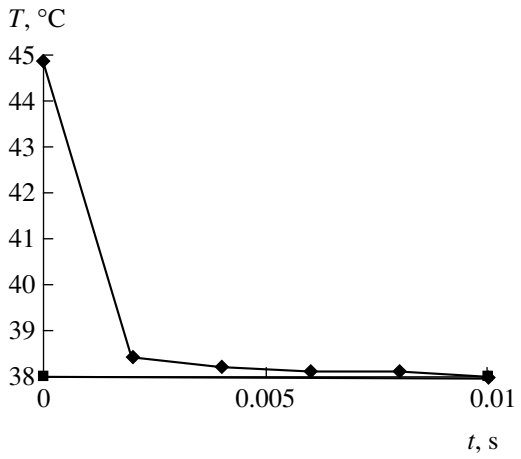

Fig. 1. The time variation of the surface temperature of a layer of solution (numerical calculation).

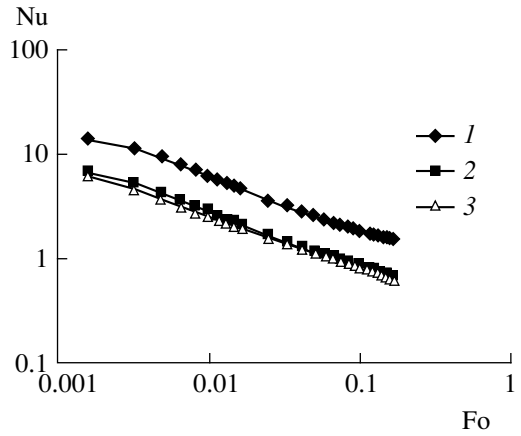

Fig. 2. The Nusselt number as a function of the Fourier number: (*1*, *2*) numerical calculation ((*1*) $\Delta T = T_n - T_o$, (*2*) $\Delta T = T_s - T_o$); (*3*) calculation by formula (13).

the law of heat transfer under conditions of combined heat and mass transfer,

$$\mathrm{Nu}^* = 0.594 M_1 \mathrm{Fo}^{-0.5}, \tag{13}$$

in which $\mathrm{Nu}^* = \alpha^* L/\lambda$ and $M_1 = 1(1 - \psi)$. Note that the appearance of the parameter M_1 in formula (13) is merely the result of overdetermination of the temperature head, because the heat transfer coefficient α^* in formula (13) is related to the heat transfer coefficient α by the simple relationship

$$\alpha^* = \frac{q}{T_s - T_o} = \frac{\alpha}{1 - \psi}. \tag{14}$$

Figure 1 demonstrates the time variation of the surface temperature of a solution as a function of time at the initial stage of the absorption process. One can see that, even at $\tau \approx 0.005$ s, the surface temperature reaches a value of $T_n \approx 38.0$°C, which agrees with the estimate given above. The surface temperature is

constant until $\tau \approx 0.14$ s, after which the value begins to decrease.

Figure 2 gives a comparison of the results of numerical calculation and calculation by formula (13). Here, points *1* were obtained in determining the temperature head as the difference between the surface temperature and the initial temperature of the solution. Points *2* were obtained in determining the difference between the equilibrium temperature of the solution, determined by its initial concentration, and the initial temperature of the solution.

Points *3* were obtained as a result of calculation by analytical expression (13). It is seen that the results of numerical calculation for the values of $10^{-3} < \mathrm{Fo} < 0.3$ agree well with those of the calculation by the analytical formula.

As a result of analysis and numerical calculations, time limits have been established, within which, first, it is permissible to make use of the laws of heat and mass transfer corresponding to small contact time and, second, expression (10) is derived for the calculation of the surface temperature of liquid layer with an arbitrary value of the contact time.

REFERENCES

1. V. E. Nakoryakov and N. I. Grigor'eva, Teor. Osn. Khim. Tekhnol. **14**, 483 (1980).
2. V. E. Nakoryakov, N. I. Grigor'eva, S. I. Lezhnin, and L. V. Potaturkina, Preprint No. 266-93 (Novosibirsk Institute of Thermophysics, Russian Academy of Sciences, 1993).
3. S. H. Chiang and H. L. Toor, Am. J. Chem. Eng. **10**, 398 (1964).
4. A. R. Dorokhov, V. S. Loginov, and E. E. Bul'ba, in *Collected Transactions of NII KT* (Khabarovsk State University, Khabarovsk, 1998), No. 4, p. 188.
5. V. M. Paskonov, V. I. Polezhaev, and L. A. Chudov, *Numerical Simulation of Processes of Heat and Mass Transfer* (Nauka, Moscow, 1984).

Translated by H. Bronsteĭn

Technical Physics Letters, Vol. 26, No. 2, 2000, pp. 153–155. Translated from Pis'ma v Zhurnal Tekhnicheskoĭ Fiziki, Vol. 26, No. 4, 2000, pp. 37–46.

Numerical Modeling of Magnetron Generators with Allowance for the Mode Competition

V. B. Baĭburin, V. P. Eremin, A. V. Sysuev, and A. A. Terent'ev

Saratov State Technical University, Saratov, 410016 Russia

Received July 12, 1999

Abstract—A numerical model of the magnetron generator is developed that makes it possible to investigate the effect of mode hopping. The performance of a magnetron in the presence of mode changing is evaluated. © *2000 MAIK "Nauka/Interperiodica".*

In magnetron generators, mode hopping is one of most frequently encountered and most dangerous types of failure. The phenomenon consists in the transition from a fundamental mode of oscillation to a different (spurious) mode as a result of a variation in supply voltage or some other parameter. Mode hopping involves a competition between oscillation modes, which ends in the domination of a single mode, as a rule, the one meeting the condition of synchronism between the electromagnetic wave and the electron stream.

Experimental investigation of the phenomenon of mode hopping encounters considerable difficulties, since the concomitant magnitudes of current and power dissipation in the anode circuit are very large and may cause damage to the device.

As regards the numerical modeling of mode hopping, including evaluation of the dynamic parameters, this kind of research was previously impossible to pursue, although the phenomenon has long been known. The fact is that the existing mathematical models, even rigorous ones, were based on the concept of an interaction space sector moving together with the wave, as originally reported in [1]. It was not until the introduction of the so-called multiperiod approach [2] that the process could be considered in the entire interaction space at a time, whereby the excitation and competition of multiple oscillation modes became accessible for detailed analysis.

This paper presents the main results of a quantitative investigation of the effect of mode hopping in terms of the multiperiod multiwave model [3].

The input data of the model are selected to the magnetron dimensions, the emission characteristics of the cathode, magnetic induction, and anode voltage. The magnetron dimensions include the radii of cathode and anode and the height of the anode unit. The emission parameters are the thermionic current density j, the maximum value σ_m of the secondary emission coefficient, etc. The anode voltage will be denoted as U_a. Each oscillation mode is specified by the "cold" electromagnetic parameters: the frequency f_i, the propagation constant γ_i, the wave impedance z_i, the loaded quality factor Q_i, and the intrinsic quality factor Q_{0i} at the frequency f_i. Also specified are ancillary parameters of the model: the initial number of charged particles and the initial mode amplitudes. The latter quantities were set equal for all of the modes, the value being an order of magnitude smaller than that expected for a fundamental regime. The initial number of charged particles randomly distributed over the electron column was 5% of the steady-state Brillouin charge. As demonstrated in [3], the values of the ancillary parameters determine only the transient required to attain the steady-state regime time and do not affect the final results of the investigation.

The modeling process involves solving the excitation equations for each mode. The equations of motion allow for the effect of the RF fields for all of the modes.

The magnetron was assumed to operate in the centimeter waveband region. Two modes were examined: a fundamental mode and a spurious mode due to elevated anode voltage. The fundamental mode parameters were f_1 = 2450 MHz, γ_1 = 7, z_1 = 6.4 Ω, Q_1 = 65, and Q_{01} =

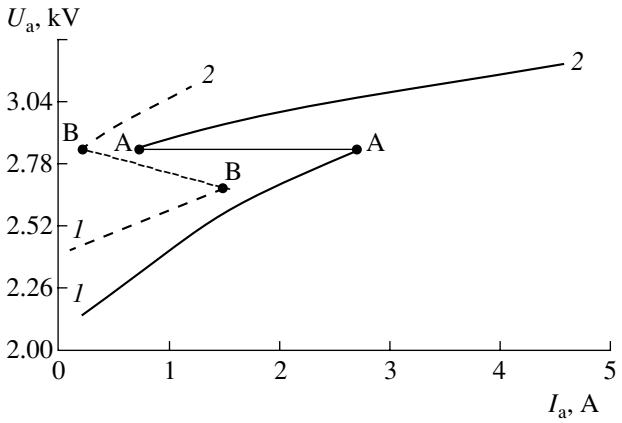

Fig. 1. Computed (–) and measured (- - -) voltage–current characteristic for the fundamental mode (segment *1*) and the spurious mode (segment *2*).

1063-7850/00/2602-0153$20.00 © 2000 MAIK "Nauka/Interperiodica"

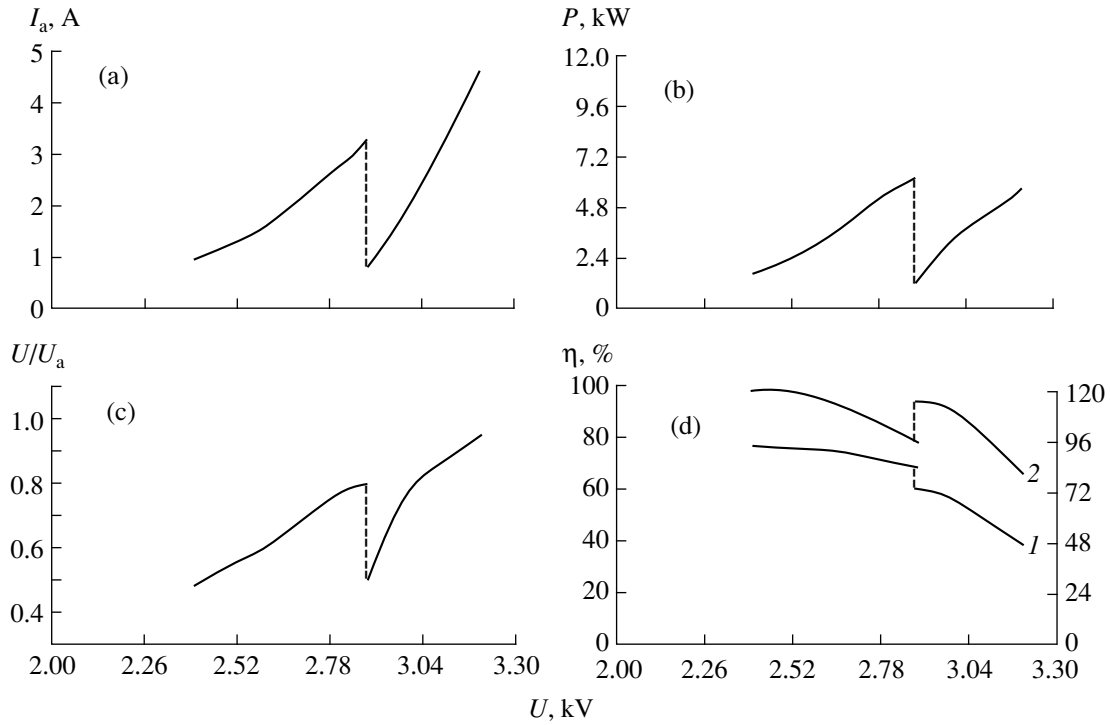

Fig. 2. Computed values of (a) anode current, (b) output power, (c) the ratio of RF amplitude to anode voltage, (d, *1*) efficiency, and (d, *2*) the ratio of space charge to the Brillouin charge vs. anode voltage.

945. The spurious mode had f_2 = 3430 MHz, γ_2 = 6, z_2 = 8.3 Ω, Q_2 = 100, and Q_{02} = 1000. The cathode emission parameters were j = 2.3 A/cm^2 and σ_m = 2.

Figure 1 indicates that an increase in the anode voltage results in quenching of the fundamental mode and switching to the spurious mode (see the *A*–*A* and the *B*–*B* segments for the computation and the experiment, respectively). The anode voltage U at which mode hopping occurs is about 2.875 kV.

Figure 2 depicts other computed characteristics as functions of the anode voltage with a jump resulting from mode hopping. Note similar trends in the behavior of characteristics for both nominal ($U_a < U$) and spurious ($U_a > U$) modes. As the anode voltage rises, the values of anode current, thermionic current, and output power increase, whereas the efficiency, back-bombardment current, and space charge decrease.

At the point of mode hopping, the amplitude and the output power of the fundamental mode are essentially larger than those of the spurious mode. However, the latter mode dominates, because it can more easily satisfy the condition of synchronism between the electron stream and RF wave in the near-cathode region (including the electron column), where electron spokes are formed. The spurious (high-voltage) mode is more competitive than the nominal (low-voltage) one, although the former mode cannot generate such powerful spokes, because the synchronism is violated near the anode.

Figure 3 shows the plots of dynamic parameters versus thermionic current density at the moment of the fundamental mode quenching. Note that the anode volt-

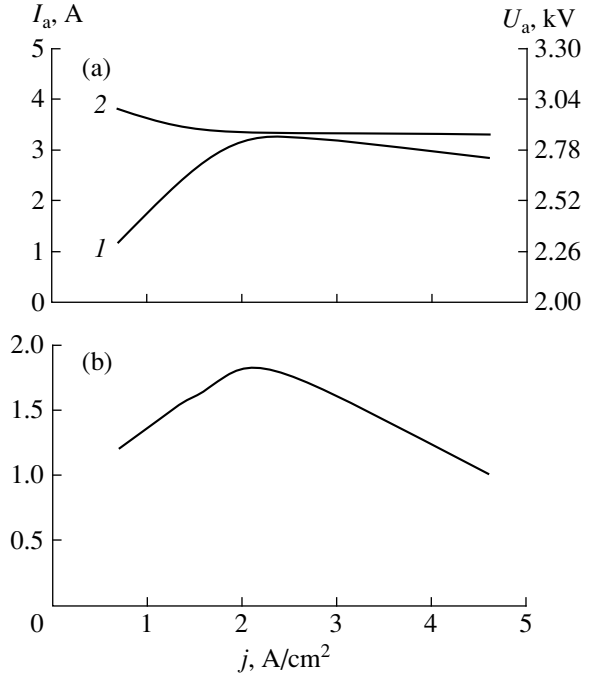

Fig. 3. Computed limiting values of (a, *1*) anode current, (a, *2*) anode voltage, and (b) secondary emission cathode current vs. thermionic current density at the moment of the fundamental mode hopping.

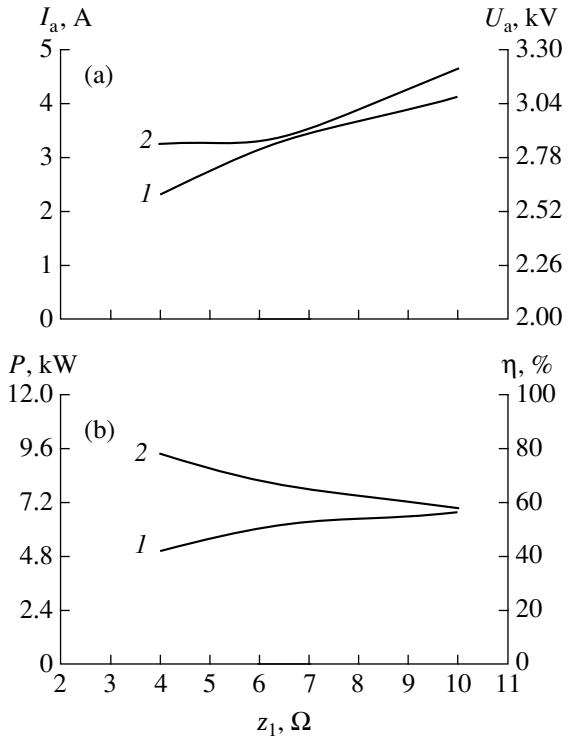

Fig. 4. Computed limiting values of (a, *1*) anode current, (a, *2*) anode voltage, (b, *1*) output power, and (b, *2*) efficiency vs. the fundamental wave impedance for the mode hopping.

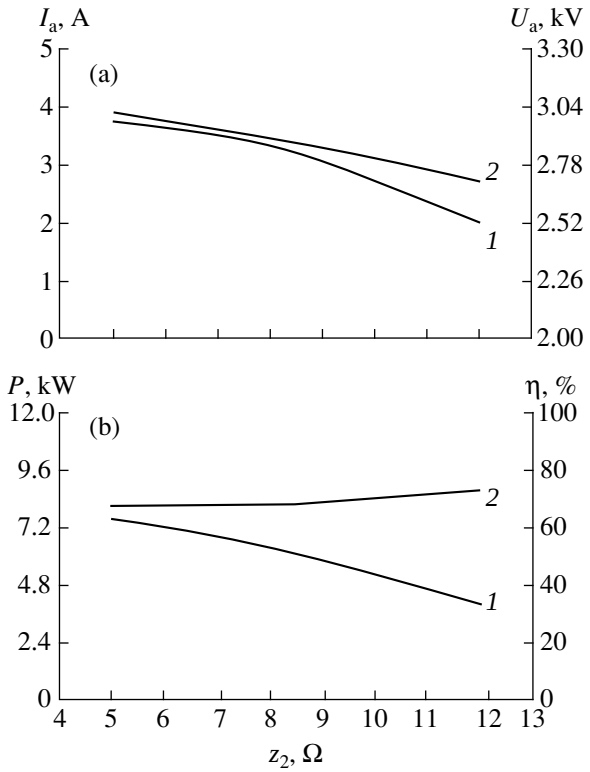

Fig. 5. Computed limiting values of (a, *1*) anode current, (a, *2*) anode voltage, (b, *1*) output power, and (b, *2*) efficiency vs. the spurious wave impedance for the mode hopping.

age rises steeply as the current falls and that the limit value of the fundamental-mode anode current exhibits a maximum.

The anode voltage at which mode hopping occurs, as well as the anode current and the output power, are virtually independent of the thermionic current density if this parameter is sufficiently large. This stems from the fact that, when the thermionic current density exceeds certain level, the space charge becomes constant and a further increase in emission exerts little or no influence on the interaction (increased back-bombardment current being the only effect).

Figures 4 and 5 show the plots of the mode hopping parameters vs. the wave impedance of the fundamental (z_1) and spurious (z_2) modes, respectively. Note that an increase in z_1 expands the range of the fundamental mode generation and increases the anode current I_a and output power P above the values obtained in the nominal regime. Accordingly, the efficiency and space charge fall. An increase in z_2 favors the interaction for the spurious mode, which results in the narrowing of the fundamental mode operating range and lowering of the I_a and U_a values for mode hopping.

Similar dependences were observed for the Q_1 and Q_2 values of both modes studied.

To sum up, the numerical modeling of a magnetron generator and the solving of test problems have demonstrated that the proposed multiwave model makes it possible to investigate the mode competition in magnetrons and to predict its outcome when optimizing the design with respect to a selected parameter. The model enables one to determine the operating range for a fundamental mode and to evaluate the conditions of mode hopping in qualitative agreement with experimental results and established physical notions.

The model can be useful for a thorough analysis of physical processes during mode hopping. In practical terms, it facilitates the optimization of output characteristics by providing both qualitative and quantitative design recommendations.

REFERENCES

1. S. P. Yu, G. P. Kooyers, and O. Buneman, J. Appl. Phys. **36**, 2550 (1965).
2. D. M. MacGregor, Appl. Surf. Sci. **8**, 213 (1981).
3. V. B. Baĭburin, A. A. Terent'ev, and S. B. Plastun, Radiotekh. Élektron. (Moscow) **41**, 236 (1996).

Translated by A. A. Sharshakov

Technical Physics Letters, Vol. 26, No. 2, 2000, pp. 156–158. Translated from Pis'ma v Zhurnal Tekhnicheskoĭ Fiziki, Vol. 26, No. 4, 2000, pp. 47–52.

Magnetodeformation Effect in a Ferroelastic Material

Yu. L. Raĭkher and O. V. Stolbov

Institute of Mechanics of Continua, Ural Division, Russian Academy of Sciences, Perm, 614061 Russia
Perm State Technical University, Perm, 614600 Russia

Received July 26, 1999

Abstract—The magnetodeformation effect in a uniform field of a ferroelastic material has been calculated under some simplifying assumptions about the properties of ferromagnetic particles. The results obtained are compared with the known experimental data. © *2000 MAIK "Nauka/Interperiodica".*

A ferroelastic material or a magnetic elastomer is a composition of a polymer matrix and a finely dispersed ferromagnetic substance. Hard-rubber-based ferroelastic materials are well known and widely used in various technologies [1]. Gel and plasticized rubber-based soft systems have been synthesized relatively recently [2, 3]. It has been established [3, 4] that magnetic fields **H** applied to these systems give rise to a pronounced magnetodeformation (magnetostriction) effect. One of the obvious factors contributing to this phenomenon is a ponderomotive force with the volume density $(\mathbf{M}\nabla)\mathbf{H}$ arising in any nonuniform magnetic field (here M is magnetization). The volume magnetodeformation effect was studied in [3]. The second contribution to the magnetodeformation effect comes from the demagnetizing fields induced in specimens and having a surface nature. The magnetodeformation effect proper is observed for an ellipsoidal specimen in a uniform magnetic field, where the volume magnetic force value becomes zero. This effect was recently observed and measured in a material comprising a siloxane rubber oligomer matrix filled with finely dispersed iron.

Let us estimate the surface magnetodeformation effect. Consider an isotropically elastic sphere of radius R in a uniform magnetic field. Being magnetized, the sphere becomes elongated in the direction of the applied field and transforms into an ellipsoid of rotation with the axes $b < R < a$ and the magnetostatic energy reduced by the value

$$\delta E_{\text{magn}} = 2\pi V \Delta N M^2,$$

where V is the specimen volume and ΔN is the increment in the demagnetizing factor. For a linear magnetization, we have $M = \chi H$, where χ is the magnetic susceptibility. At complete magnetization, $M = M_0$, where M_0 is the saturation magnetization of the material. For small elongations, we have $\Delta N = -(4/15)(a - b)/R$.

The above deformation increases the elastic energy of the specimen. In the approximation of small deformations (Hooke's law), this contribution has the form [5]

$$\delta E_{\text{el}} = (2\mu/3)V(a-b)^2/R^2,$$

where μ is the shear modulus. Minimizing the sum of the magnetic and the elastic contributions with respect to the relative strain, we obtain

$$\frac{a-b}{R} = \frac{2\pi}{5\mu}\begin{cases}\chi^2 H^2 & \text{at} \quad H \longrightarrow 0,\\ M_0^2 & \text{at} \quad H \longrightarrow \infty,\end{cases} \tag{1}$$

whence it is seen that the field dependence of the magnetodeformation effect is similar to the squared magnetization curve. The dielectric analog of estimate (1) in a weak field is well known [6]. In terms of magnetism, this estimate at $M = \chi H$ was used in [4] for a qualitative interpretation of the surface magnetodeformation effect. Below, we consider a quantitative model taking into account the saturation of magnetization and finite values of strain.

Let us assume that filling the matrix with microparticles produces no qualitative changes in the deformation behavior of the matrix, so that the ferroelastic composition is considered as an incompressible elastic material. The filler grains are monodisperse single-domain particles of a magnetically soft ferromagnetic material (iron). The particle shape is close to spherical; therefore, the magnetooptical anisotropy is small and, at the laboratory (room) temperature, the particles are superparamagnetic. As a result, there is no magnetization hysteresis and the magnetic state of the material is described by the Langevin law

$$\mathbf{M}(\mathbf{H}) = M_0 L(mH/k_BT)(\mathbf{H}/H). \tag{2}$$

Here $m = Iv$ is the magnetic moment of a single-domain particle, equal to the product of its volume by the magnetization I of the ferromagnetic material. In turn, the saturation magnetization of a ferroelastic material can be written as $M_0 = nm$, where n is the number density of magnetic particles. The argument of the Langevin function in equation (2) has the sense of the ratio of the characteristic orientational energy of the magnetic

moment of the particle in the applied field to the thermal energy k_BT.

According to equation (2), the spherical specimen is magnetized along the applied field, so that deformation reduces to elongation in the direction of **H** and contraction in the perpendicular plane. For an incompressible material, this is equivalent to pure shear [5]. We assume that this operation is characterized by affinity; in other words, the specimen retains the shape of an ellipsoid of rotation irrespective of the elongation value. The magnetic field inside an ellipsoid placed in a magnetic field is also uniform, and therefore the material deformation is uniform as well. In this case, the free energy functional is the product of the corresponding energy density and the specimen volume.

Consider an elastic energy. The measure of deformation for a sphere of radius R is the ratio $\lambda = a/R$, where a is the major semiaxis of the formed ellipsoid. Thus, for an "unperturbed" specimen, $\lambda = 1$. Elasticity of rubbers is well described by the Mooney–Rivlin potential, which for the uniaxial deformation has the form [7]

$$E_{\text{el}} = V[C_1(\lambda^2 + 2/\lambda - 3) + C_2(1/\lambda^2 + 2\lambda - 3)], \quad (3)$$

where the coefficient C_1 has the sense of the rubberlike elasticity modulus, whereas the initial shear modulus of the material is described by the formula $\mu = 2(C_1 + C_2)$.

Following [6], we can write the magnetic free energy of a body in a constant magnetic field (which is assumed to be uniform and a given ferroelastic material is assumed to exhibit isotropic magnetization) in the form

$$E_{\text{magn}} = V\left[\frac{1}{2}M(H - H_0) - \int_0^H MdH\right], \quad (4)$$

where H_0 is an external field and H is the field inside the specimen.

The external and internal fields for an ellipsoid are related as follows [6]:

$$H = H_0 - 4\pi NM(H). \quad (5)$$

For uniaxial deformations, the component of the tensor of demagnetization coefficients along the direction of the ellipsoid elongation is

$$N(\lambda) = \frac{\operatorname{arctanh}\sqrt{1-\lambda^{-3}} - \sqrt{1-\lambda^{-3}}}{(\lambda^3 - 1)\sqrt{1-\lambda^{-3}}}. \quad (6)$$

In the magnetic equation of state (2), integral (4) can be taken in quadratures. Summing the result of the integration and elastic potential (3), we arrive at the function

$$\begin{aligned} E_S(\lambda, H_0)/V &= [C_1(\lambda^2 + 2/\lambda - 3) + C_2(1/\lambda^2 + 2\lambda - 3)] \\ &- \frac{M_0}{p}\ln\frac{\sinh(pH)}{pH} - 2\pi M_0^2 N(\lambda)L^2(pH), \end{aligned} \quad (7)$$

whose arguments are the dimensionless elongation and the applied field strength. We also introduced the notation $p = m/k_BT$. Differentiating (7), we arrive at the equilibrium equation

$$\frac{\partial E_S}{\partial \lambda} = (C_1\lambda + C_2)\left(1 - \frac{1}{\lambda^3}\right) + \pi M_0^2 L^2(pH)\frac{\partial N}{\partial \lambda} = 0. \quad (8)$$

Relationships (8), (2), (5), and (6) determine the function $\lambda(H_0)$ characterizing the magnetodeformation effect. For small elongations ($\lambda - 1 \ll 1$), equation (8) yields

$$\lambda - 1 = (4\pi/15\mu)M_0^2 L^2(pH). \quad (9)$$

In fact, this expression is equivalent to the estimates given by (1). If $\lambda > 1$, the demagnetizing factor decreases, according to (6), by the law $N = (3/2\lambda^3)\ln\lambda$, and the equation for the magnetodeformation effect takes the form

$$\lambda^\alpha/\ln\lambda = (9\pi/\mu)M_0^2 L^2(pH), \quad (10)$$

where the exponent α ranges from 4 (at $C_1 \ll C_2$) to 5 (at $C_1 \gg C_2$).

For a typical magnetization value $M_0 \sim 100$ G, the difference between H and H_0 in fields with a strength of several kOe becomes insignificant and the Langevin function should exhibit saturation. Let us estimate a characteristic range of the values of the elastic moduli of ferroelastic materials. In a "hard" system, where the limiting value of the magnetodeformation effect is $\lambda - 1 \lesssim 10^{-2}$, equation (9) yields $\mu \gtrsim 10^6$ dyn/cm$^2 \approx 1$ at. In the "soft" system, where the elongation can reach $\lambda \gtrsim 2$, equation (10) yields $\mu \lesssim 5 \times 10^3$ dyn/cm$^2 \approx 5 \times 10^{-3}$ at.

To compare our calculated data (see figure) with experiment, we used the data on elongation $\lambda(H_0)$ of a silicon-based ferroelastic sphere with a diameter of 6 mm in a uniform field [4]. The theoretical curve was obtained by the numerical solution of equation (8) with due regard for relationships (5) and (6). The material parameters were obtained by fitting. In the first variant of the calculation (solid line in figure), we used the value $C_2 = 0$ (the empirical rule for swollen rubbers [7]) and obtained $M_0^2/C_1 = 57.6$ and $p = 3.5 \times 10^{-4}$ Oe^{-1}. At $M_0 \approx 100$ G, the initial shear modulus was determined as $\mu = 2C_1 \approx 3.5 \times 10^{-4}$ at. In the second variant, both C_1 and C_2 were varied; the corresponding curve of the magnetodeformation effect is shown by the dashed

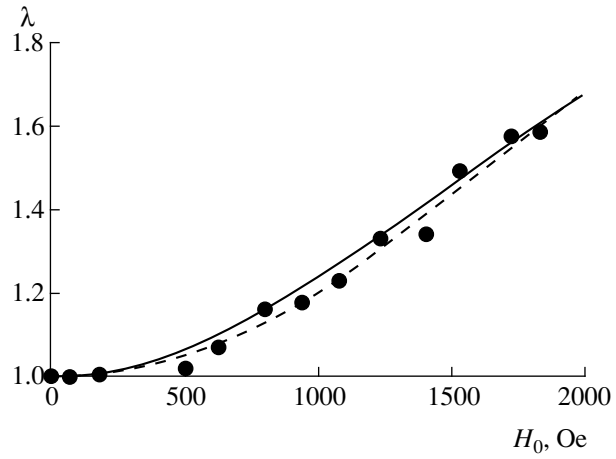

The plot of λ versus H_0: solid and dashed curves show the results of calculation by equation (8), and black symbols represent the experimental data from [4].

line. The numerical values are $M_0 = 102$ G, $C_1 = 68$ and $C_2 = 234$ dyn/cm^2, and $p = 3.8 \times 10^{-4}$ Oe^{-1}; the shear modulus is $\mu = 2(C_1 + C_2) \approx 6 \times 10^{-4}$ at. Thus, the values of elastic moduli agree in the order of magnitude. It should be emphasized that these values are lower by an order of magnitude than the corresponding values for poly(vinyl alcohol) ferrogels studied in [3].

Note that the calculated values of the parameter p are consistent with experimental data. Assuming that single-domain particles have a spherical shape, we can use these p values to estimate the average particle diameter d. By definition, $p = Iv/k_BT$, and we obtain $d \sim \sqrt[3]{6 p_{obs} k_B T/\pi I}$; for iron magnetization $I \sim 2 \times 10^3$ G, which yields $d \sim 2.4$ nm. However, it is hardly probable that the particles can be so small. Moreover, the result obtained is inconsistent with the value $d \gtrsim 10$ nm indicated in [4]. One of the possible explanations of this inconsistency is the existence of the size effect typical of disperse magnetic materials, where the nonsymmetric environment excludes the exchange interactions of surface spins. As a result, the ferromagnetic part proper ("core") occupies only a small part of the total volume of a solid particle.

ACKNOWLEDGMENTS

The authors are grateful to L.V. Nikitin and L.S. Mironova for fruitful discussions. The study was supported by the Russian Foundation for Basic Research, project no. 98-02-16453.

REFERENCES

1. A. G. Alekseev and A. E. Kornev, *Elastic Magnetic Materials* (Khimiya, Moscow, 1976); *Magnetic Elastomers* (Khimiya, Moscow, 1987).
2. J. Dumas and J.-C. Bacri, J. Phys. Lett. **41**, 279 (1980).
3. M. Zrinyĭ, L. Barsi, and A. Buki, J. Chem. Phys. **104**, 8750 (1996); M. Zrinyĭ, L. Barsi, D. Szabo, *et al.*, J. Chem. Phys. **106**, 5685 (1997); M. Zrinyĭ, D. Szabo, and H.-G. Kilian, Polym. Gels Networks **6**, 441 (1998).
4. K. G. Kornev, L. V. Nikishin, and L. S. Mironova, in *Proceedings of XVI International School–Seminar New Magnetic Materials for Microelectronics, Moscow, Russia, 1998*, Part 2, p. 387; *The VIII International Ples Conference on Magnetic Liquids, Ples, 1998*, p. 95.
5. L. D. Landau and E. M. Lifshitz, *Theory of Elasticity* (Nauka, Moscow, 1987; Oxford, Pergamon Press, 1980).
6. L. D. Landau and E. M. Lifshitz, *Electrodynamics of Continuous Media* (Nauka, Moscow, 1982; Oxford, Pergamon Press, 1981).
7. G. V. Vinogradov and A. Ya. Malkin, *Rheology of Polymers* (Khimiya, Moscow, 1977).

Translated by L. Man

Technical Physics Letters, Vol. 26, No. 2, 2000, pp. 159–160. Translated from Pis'ma v Zhurnal Tekhnicheskoĭ Fiziki, Vol. 26, No. 4, 2000, pp. 53–57.

Effect of Ultraviolet Irradiation on the Charge State of Ion-Implanted Silicon–Silicon Dioxide Structures

A. P. Baraban and L. V. Malyavka

Institute of Physics, St. Petersburg State University, Universitetskaya nab. 7/9, St. Petersburg, 199164 Russia

Received October 6, 1999

Abstract—The effect of irradiation with the light from a near-ultraviolet range (NUV irradiation) on the charge state of Si–SiO_2 structures with an argon-implanted silicon dioxide layer was studied. The method of depth profiling based on the measurement of high-frequency capacitance–voltage characteristics of an electrolyte–dielectric–semiconductor system in combination with etching of the dielectric layer was used. It was established that the NUV irradiation resulted in the recharge of positively charged amphoteric centers (formed due to ion implantation in the silicon dioxide layer of the Si–SiO_2 structures) into negatively charged ones. © *2000 MAIK "Nauka/Interperiodica".*

Various aspects of the effects caused by irradiation of Si–SiO_2 structures have been studied for many years. In particular, the ion implantation and the UV irradiation of such structures are of great interest for the study of fundamental laws governing the formation of defects in solids and for the use of these structures in microelectronics.

The purpose of this work was to study the effect of irradiation with the light from the near-ultraviolet range (NUV irradiation) on the state of electrically active centers induced by ion implantation in the silicon dioxide layer of Si–SiO_2 structures.

We studied the Si–SiO_2 structures obtained by thermal oxidation of KEF-5 (100) and KDB-10 (100) silicon wafers in wet oxygen at 950°C.[1] To avoid strong heating of the target, the 250- and 90-nm-thick SiO_2 layers were cooled and implanted with low-density argon ion beams at a dose of 10^{13} cm^{-2} and 10^{12}–10^{14} cm^{-2}, respectively, on an Eaton Nova 4206 setup. The ion energy was selected so as to provide the maximum concentration of implanted ions in the middle of the silicon dioxide layer and was equal to 130 and 43 eV for the Si–SiO_2 structures with a silicon dioxide layer thickness of 250 and 90 nm, respectively. The ion-implanted structures of the second type were subjected to rapid thermal annealing at 450°C by exposure for 10 s to the light of a halogen lamp in a nitrogen atmosphere. The NUV irradiation of the specimens was effected by the light of a DRL-250 mercury lamp ($h\nu$ = 4–6 eV). The charge state of the Si–SiO_2 structures was studied by the method of depth profiling based on the measurements of high-frequency capacitance–voltage characteristics in the electrolyte–dielectric–semiconductor system in combination with etching of the dielectric layers [1]. All the measurements were made at a temperature of 293 K.

The method of depth profiling employed allows the flat-band potential (V_{fb}) to be studied as a function of the silicon dioxide layer thickness (Figs. 1, 2). These curves provide information on the charge distribution in the silicon dioxide layer. The positions X of the charge centroids in the silicon dioxide layer were determined as the thicknesses of the silicon dioxide layers corresponding to intersection of the $V_{fb}(d_{ox})$ plots interpolated to zero thickness. The true values of charges formed in the ion-implanted silicon dioxide layers were determined from the slopes of these plots [1].

A comparison of the capacitance–voltage characteristics measured during etching of the silicon dioxide

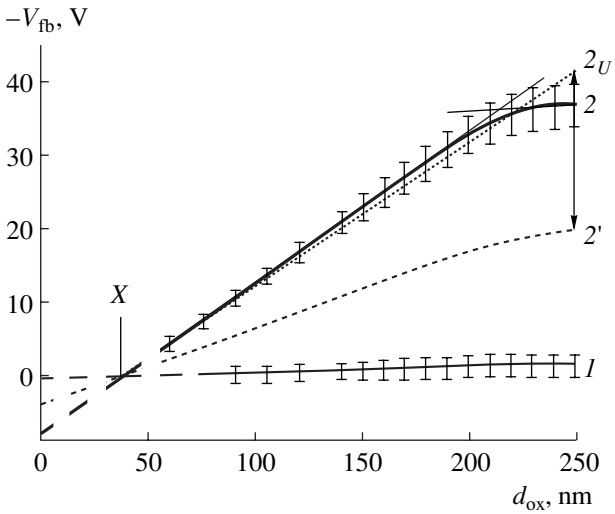

Fig. 1. Flat-band potential as a function of the thickness of a silicon dioxide layer in the (*1*) initial and (*2*) Ar-implanted 250-nm-thick Si–SiO_2 structures; (*2'*) upon 10-s-long NUV irradiation, (2_U) upon NUV irradiation in an applied electric field (negative bias at the field electrode).

[1] The Russian trademarks for phosphorus-doped *n*-type and boron-doped *p*-type silicon.

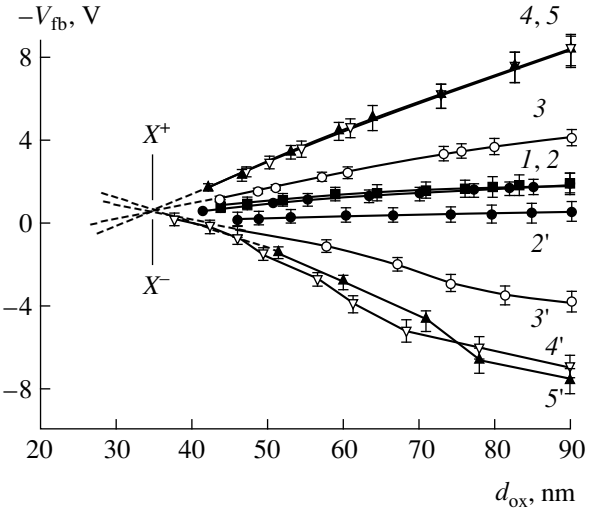

Fig. 2. Flat-band potential as a function of the thickness of the silicon dioxide layer in the (*1*) initial and (*2*–*5*) Ar-implanted 90-nm-thick Si–SiO_2 structures subjected to subsequent rapid thermal annealing at 450°C. The irradiation doses D (cm^{-2}) are (*2*) 10^{12}, (*3*) 10^{13}, (*4*) 10^{14}, (*5*) 10^{14} (at a low ion beam current); (*2*'–*5*') the same upon NUV irradiation.

layers of the initial and the ion-implanted Si–SiO_2 structures showed that ion implantation to a dose of $D = 10^{13}$ cm^{-2} resulted in the formation of a positive charge with the centroid position $X = (35 \pm 5)$ nm in the vicinity of the Si boundary in the 250-nm-thick Si–SiO_2 structures [2]. In the 90-nm-thick Si–SiO_2 structures, a positive charge in the vicinity of the Si boundary [with the centroid at $X = (34 \pm 5)$ nm] appeared beginning with the irradiation dose $D = 10^{13}$ cm^{-2} and increased with the implantation dose (Fig. 2).

The NUV irradiation of the initial (unimplanted) Si–SiO_2 structures produced no noticeable changes in the charge state of the silicon dioxide layer. The NUV irradiation of ion-implanted Si–SiO_2 structures without application of an external electric field resulted in the formation of a considerable negative charge in SiO_2 in the vicinity of the Si–SiO_2 boundary. The value of this negative charge exceeded the value of the positive charge induced by ion implantation and did not change upon half-a-year's storage of the irradiated specimens at room temperature. For the 250-nm-thick Si–SiO_2 structures, the total negative charge had a rather large value; but it was not determined, because no such measurements could be performed in the electrolyte–dielectric–semiconductor system at a positive bias on the field electrode. The negative-charge centroid formed in the silicon dioxide layer of the structures upon 10-s-long NUV irradiation coincided with the positive-charge centroid formed due to ion implantation (Fig. 1). In the NUV-irradiated 90-nm-thick Si–SiO_2 structures subjected to rapid thermal annealing at 450°C after ion implantation, a negative charge had the centroid coinciding with the positive-charge centroid, with the absolute charge value being about twice that of the positive charge (Fig. 2). The NUV irradiation at a negative bias on the field electrode (preventing the injection of electrons from Si into SiO_2) did not alter the charge state of the implanted structures.

Coincidence of the implantation-induced positive-charge centroid in SiO_2 with the negative-charge centroid formed due to NUV irradiation, as well as an approximately double value of the negative charge in comparison with the positive one, indicate that both charges are related to the same amphoteric centers. As a result of the ion implantation involving the interaction of Ar ions with the atomic subsystem of the SiO_2 matrix, two nonstoichiometric SiO_x regions are formed in the bulk of the silicon dioxide layer—those with $x > 2$ and $x < 2$ [2]. The oxygen-enriched region ($x > 2$) is located closer to the silicon surface (because of a greater displacement of oxygen atoms as compared to that of silicon atoms upon their interaction with argon). It is the formation of these nonstoichiometric regions and the corresponding defects that explains the appearance of electrically active centers during argon ion implantation. For the oxygen-depleted region (in which the positive-charge centroid is located upon ion implantation [2]), the most probable defects are of the types of a silicon atom coordinated with three oxygen atoms and/or an oxygen vacancy. The defects of both types are amphoteric centers and can be formed during ion implantation either directly in the positively charged state or in the neutral state with subsequent positive charging as a result of trapping of holes formed due to the interaction of Ar ions with the electron subsystem of the SiO_2 matrix. The absence of changes in the charge state of the ion-implanted structure during the NUV irradiation with applied electric field (with a negative bias on the field electrode) indicates that the recharge of positive amphoteric centers into negative ones during the NUV irradiation is related to the trapping of electrons optically excited from Si to the conduction band of SiO_2.

Thus, the NUV irradiation results in recharge of the positive amphoteric centers (formed during or due to implantation) into a negative state. This effect can be used to design sensors based on ion-implanted Si–SiO_2 structures for detecting the NUV radiation and determining the ion-implanted SiO_2 regions in Si–SiO_2 structures.

REFERENCES

1. A. P. Baraban, V. V. Bulavinov, and P. P. Konorov, *Electronics of SiO_2 Layers on Silicon* (LGU, Leningrad, 1988).
2. A. P. Baraban, A. A. Kuznetsov, A. A. Malyavka, *et al.*, Izv. Vyssh. Uchebn. Zaved., Élektronika, No. 4, 17 (1998).

Translated by L. Man

Technical Physics Letters, Vol. 26, No. 2, 2000, pp. 161–162. Translated from Pis'ma v Zhurnal Tekhnicheskoĭ Fiziki, Vol. 26, No. 4, 2000, pp. 58–61.

Rotational Moment in Thermal Vibrations of a Bound Charged Particle in a Constant Magnetic Field

Yu. A. Kartashov and I. V. Popov

Received September 16, 1999

Abstract—The effect of a constant magnetic field on thermal vibrations of a charged particle in a condensed medium was theoretically studied. It is shown that the particle and its surroundings in the constant magnetic field are subjected to a constant rotational moment, the direction of which is determined by the sign of the particle charge and the direction of the magnetic induction. The magnitude of mechanical stresses induced by this moment in the medium is found to change in a stepwise manner upon a "phase transition" of the particle from the bound to the free state. © *2000 MAIK "Nauka/Interperiodica".*

There are experimental indications of a pronounced effect of extremely weak constant magnetic fields (MFs) on the physical parameters of condensed media [1, 2]. Unfortunately, the theory of sensitivity to weak MFs is virtually undeveloped, because even a possible mechanism of the effect of MFs on a condensed medium is unknown.

In this work, we have theoretically studied the effect of a constant MF on the thermal vibrations of a charged particle. It is shown that the particle and its surroundings moving in the constant MF are subjected to a rotational moment. The magnitude of mechanical stresses induced by this moment in the medium is found to change in a stepwise manner when the particle exhibits a "phase transition" from bound to free state.

Let us consider a simplified model describing the dynamics of a point particle in a spherical potential well. In this model, the equation of vibrations has the following form:

$$m\frac{d^2\mathbf{r}}{dt^2} = -\kappa\mathbf{r} - \frac{m}{\tau}\frac{d\mathbf{r}}{dt} + q\frac{d\mathbf{r}}{dt}\times\mathbf{B}_0 + q\mathbf{E}, \qquad (1)$$

where $\mathbf{r}$ is the displacement from the equilibrium position of a particle with mass m and charge q, κ is the coefficient of elasticity, $\mathbf{B}_0$ is the induction of the constant MF, $\mathbf{E}$ is the electric field (EF) strength, and τ is the relaxation time. Experimental data presented in [1] demonstrate that τ depends on the MF strength.

We may seek a solution to equation (1) in the form of

$$\boldsymbol{\xi} = \alpha\mathbf{e} + \beta\mathbf{e}\times\mathbf{B}_0 + \gamma(\mathbf{e}\times\mathbf{B}_0)\times\mathbf{B}_0,$$

where α, β, and γ are constants, and $\mathbf{e}$ and the quantities $\boldsymbol{\xi}$ are the spectral amplitudes of $\mathbf{E}$ and $\mathbf{r}$, respectively, which satisfy the relations

$$\mathbf{E} = \int_{-\infty}^{\infty}\mathbf{e}\cdot\exp(i\omega t)d\omega,$$
$$\mathbf{r} = \int_{-\infty}^{\infty}\boldsymbol{\xi}_0\exp(i\omega t)d\omega. \qquad (2)$$

Substituting formulas (2) into equation (1) and taking into account that $(\mathbf{e}\times\mathbf{B}_0)\times\mathbf{B}_0 = \mathbf{B}_0(\mathbf{e}\cdot\mathbf{B}_0) - \mathbf{e}B_0^2$, we obtain the relationship

$$\boldsymbol{\xi}_0 = \frac{q}{m}\frac{a_0}{a_0^2 - \Omega_c^2\omega^2}\mathbf{e}$$
$$+ i\frac{q^2}{m^2}\frac{\omega}{a_0^2 - \Omega_c^2\omega^2}\left[\mathbf{e}\times\mathbf{B}_0 + i\frac{q}{m}\frac{\omega}{a_0}(\mathbf{e}\cdot\mathbf{B}_0)\mathbf{B}_0\right], \qquad (3)$$

where $Q_0 = \omega_0^2 - \omega^2 + i\omega/\tau$, $\omega_0^2 = \kappa/m$, and $\boldsymbol{\Omega}_c = (q/m)\mathbf{B}_0$ is the cyclotron frequency of the particle.

The field $\mathbf{E}$ appearing in formulas (1)–(3) is the internal fluctuational (in particular, thermal) EF that acts on the particle. Note that relationship (3) is essentially an equation of the particle dynamics in the spectral representation, which is more general than equation (1), because the relaxation time τ depends on the frequency; i.e., $1/\tau = F(\omega)$.

Let us find the ensemble-average value of the rotational moment $\mathbf{M}_0$ related to the Coulomb forces acting on the particle. To simplify the calculations, we will assume that $\mathbf{r}$ and $\mathbf{E}$ are taken at the time instants t and $t' < t$, respectively. In the final expression, we put

$\Delta t = t - t' - 0$. In this case, we have

$$\overline{\mathbf{M}_0} = \overline{\mathbf{r}(t) \times q\mathbf{E}^*(t')} = q\int\limits_{-\infty}^{\infty}\int\overline{\xi_0(\omega)\mathbf{e}^*(\omega')}\exp(i\omega t - i\omega' t')d\omega d\omega', \quad (4)$$

where * means the conjugation.

Substituting the value ξ_0 from (3) into expression (4) and assuming that the fluctuational EF is isotropic and stationary and there is no correlation between orthogonal components of the vector **e**, we obtain

$$\overline{\xi_0(\omega) \times \mathbf{e}^*(\omega')} = \frac{2}{3}i\frac{q^2}{m^2}\frac{\omega\mathbf{B}_0}{a_0^2 - \Omega_c^2\omega^2}g_e(\omega)\delta(\omega - \omega'), \quad (5)$$

where $g_e(\omega)$ is the spectral density of EF and $\delta(\omega)$ is the delta function.

Finally, expression (4) yields

$$\overline{\mathbf{M}_0} = \frac{2}{3}i\frac{q^3}{m^2}\mathbf{B}_0\int\limits_{-\infty}^{\infty}\frac{\omega\exp(i\omega\Delta t)}{a_0^2 - \Omega_c^2\omega^2}g_e(\omega)d\omega. \quad (6)$$

The spectral density $g_e(\omega)$ of EF entering into formulas (5) and (6) is determined by the microstructure of the medium and is one of its basic characteristics.

In the case of thermodynamic equilibrium, according to the fluctuation–dissipation theorem [3], the function $g_e(\omega)$ is related to the relaxation time as

$$g_e(\omega) = 3m\theta(\omega, T)/\pi q^2\tau, \quad (7)$$

where $\theta(\omega, T) = (\hbar\omega/2)\coth(\hbar\omega/2kT)$ is the average energy of the quantum oscillator; k and $\hbar$ are the Boltzmann and Planck constants, respectively; and T is the absolute temperature. In what follows, we will use the classical approximation $\theta(\omega, T) = kT$ valid under the condition $\hbar\omega_0 \ll kT$.

Thus, in the case of thermodynamic equilibrium, the rotational moment has the following form:

$$\overline{\mathbf{M}_0} = 2i\frac{kT}{\pi}\frac{q}{m}\mathbf{B}_0\int\limits_{-\infty}^{\infty}\frac{\omega\exp(i\omega\Delta t)}{a_0^2 - \Omega_c^2\omega^2}F(\omega)d\omega. \quad (8)$$

Calculating integral in (8) by the method of residues, we obtain

$$\overline{\mathbf{M}_0} = 2kT\boldsymbol{\Omega}_c\frac{1}{\omega_0}\frac{\partial F(\omega)}{\partial\omega}\bigg|_{\omega = \omega_0}. \quad (9)$$

In the case of $\omega_0 = 0$ (free particle), the integral in (8) must be calculated with allowance for the integrand singularity at the point $\omega = 0$. Taking this into account, we derive

$$\overline{\mathbf{M}_1} = -2kT\boldsymbol{\Omega}_c\frac{\tau(0)}{1 + \Omega_c^2\tau^2(0)}, \quad (10)$$

where $\tau(0)$ is the value of the relaxation time at low frequencies.

Comparing expression (9) and (10), we obtain the ratio of the rotational moments for the bound and free particle:

$$\frac{\overline{\mathbf{M}_0}}{\overline{\mathbf{M}_1}} = \frac{1 + \Omega_c^2\tau^2(0)}{\omega_0\tau(0)}\frac{\partial F(\omega)}{\partial\omega}\bigg|_{\omega = \omega_0}.$$

This ratio is extremely small, because $\omega_0\tau(0) \gg 1$ and $\left|\frac{\partial F(\omega)}{\partial\omega}\right|_{\omega = \omega_0} \leq 1$. Nevertheless, simple estimations demonstrate that the value of the rotational moment for a bound particle is comparable with the rotational moment per atom in the conductor of an electric motor winding.

According to Newton's third law, the rotational moments under consideration will act on particles of the surrounding medium to cause the corresponding stresses and deformations in this medium.

A bound particle is subjected to (and induces in the surroundings) considerably lower stresses than does the free one. If the particle escapes from the potential well owing to some physical reason (e.g., the resonance MF) the stresses discussed above exhibit a stepwise rise. Therefore, the rotational moment is an indicator of the phase transition from bound to free particle. This transition caused by a resonance MF will probably lead to changes in some other parameters as well, in particular, in the specific conductivity of the medium. This is likely the phenomenon that was observed in [4].

REFERENCES

1. L. P. Semikhina, Candidate's Dissertation in Mathematical Physics (Moscow State University, Moscow, 1989), p. 21.
2. V. I. Klassen, *Magnetization of Aqueous Systems* (Khimiya, Moscow, 1982).
3. S. M. Rytov, *Introduction to Statistical Radiophysics* (Nauka, Moscow, 1966).
4. V. V. Novikov and M. N. Zhadin, Biofizika **39**, 45 (1994).

Translated by R. Tyapaev

Technical Physics Letters, Vol. 26, No. 2, 2000, pp. 163–164. Translated from Pis'ma v Zhurnal Tekhnicheskoĭ Fiziki, Vol. 26, No. 4, 2000, pp. 62–66.

New Buffer Sublayers for Heteroepitaxial III–V Nitride Films on Sapphire Substrates

M. I. Kotelyanskiĭ, I. M. Kotelyanskiĭ, and V. B. Kravchenko

Institute of Radio Engineering and Electronics, Russian Academy of Sciences, Moscow, 103907 Russia

Received July 9, 1999

Abstract—It is suggested to deposit III–V nitride films onto sapphire substrates upon preliminary deposition of a buffer sublayer of a crystalline material with a cubic structure. It is shown experimentally that the deposition of a heteroepitaxial niobium sublayer onto a (0001)-oriented sapphire substrate or a niobium nitride sublayer onto a $(11\bar{2}0)$-oriented Al_2O_3 substrate eliminates a 30° rotation of the (0001)-oriented nitride film in the substrate plane. The elimination of this rotation provides considerable reduction of the lattice mismatch between the substrate and the nitride film, which, in turn, should increase the degree of crystal perfection of the film. In addition, the planes of semiconductor nitride films become parallel to the natural cleavage planes of the substrate. This fact provides for the possibility of manufacturing a heterolaser with a Fabry–Perot resonator, in which the role of the mirrors is played by natural cleavage planes of the film. © *2000 MAIK "Nauka/Interperiodica".*

One of the major problems encountered in the creation of semiconductor devices based on heteroepitaxial III–V nitride films is a high defect concentration (10^{-8}–10^{-10} cm^{-2}) inherent in their crystal structures, which is caused by a considerable lattice mismatch between the surface planes of the substrate and the deposited semiconductor film. For the substrates used nowadays for the growth of epitaxial (0001) GaN films, this mismatch amounts to 16% for (0001) Al_2O_3, 9.5% for $MgAl_2O_4$, and 3.5% for SiC substrates. For the growth of epitaxial films on (0001) Al_2O_3 substrates, the lattice mismatch can be reduced with the aid of a heteroepitaxial buffer sublayer between the working surface of the substrate and the semiconductor nitride film. Usually, these buffer sublayers are prepared from materials with a wurtzite-type structure, such as GaN, AlN, or ZnO [1].

The pronounced mismatch of the lattice parameters during the heteroepitaxial growth of hexagonal materials with the wurtzite-type structure on (0001) Al_2O_3 substrates is explained by the fact that the matching (0001) planes of the Al_2O_3 substrate and the nitride film are rotated by 30° with respect to one another, so that the $\langle 1\bar{1}00\rangle$ directions of the Al_2O_3 substrate are parallel to the $\langle 11\bar{2}0\rangle$ directions of the nitride film. The translation along the $\langle 1\bar{1}00\rangle$ Al_2O_3 direction equals 2.747 Å, whereas the translation, e.g., along the ⟨1120⟩ GaN direction, equals 3.189 Å.

Below we suggest a method that eliminates the 30° rotation of the (0001) heteroepitaxial III–V nitride film with respect to the (0001) or $(11\bar{2}0)$ working surface of the sapphire substrate.

We paid attention to the fact that elimination of the 30° mutual rotation between these planes considerably reduced the lattice mismatch. Indeed, the lengths of two translations along $\langle 1\bar{1}00\rangle$ Al_2O_3 equals 5.494 Å, which almost (to within 0.5%) coincides with the translation along $\langle 1\bar{1}00\rangle$ GaN (equal to 5.52 Å). The sum of two translations along $\langle 11\bar{2}0\rangle$ Al_2O_3 (9.52 Å) almost (to within 0.5%) coincides with the length of three translations along $\langle 11\bar{2}0\rangle$ GaN.

Earlier, we proposed to eliminate the 30° rotation with the aid of a buffer sublayer of a cubic crystalline material, which, for the heteroepitaxial growth on the (0001) or $(11\bar{2}0)$ Al_2O_3 substrates, is characterized by the {111} orientation of the surface, with the ⟨112⟩ direction in this plane being parallel to the $\langle 1\bar{1}00\rangle$ directions located in the working surface of the Al_2O_3 substrate. The (0001) plane of a heteroepitaxial film with the wurtzite structure grown on this buffer sublayer and the $\langle 1\bar{1}00\rangle$ directions in this plane are parallel to the {111} planes and the ⟨112⟩ directions of the buffer sublayer, respectively.

In other words, the use of a buffer sublayer of such a cubic material provides for the following orientational relationships:

(a) $(0001)\,Al_2O_3 \| \{111\}_c \| (0001)_w$;

(b) $(11\bar{2}0)\,Al_2O_3 \| \{111\}_c \| (0001)_w$;

1063-7850/00/2602-0163$20.00

and, in both cases, $\langle 1\bar{1}00\rangle$ $Al_2O_3 \| \langle 112\rangle_c \| \langle 1\bar{1}00\rangle_w$. The buffer sublayer from such a cubic material considerably reduces the mismatch between the lattice parameters of the planar networks of the contacting planes, e.g., those of (0001) Al_2O_3 and {111} of the buffer sublayer, on the one hand, and the {111} of the buffer sublayer and (0001) of the wurtzite-type nitride film (e.g., GaN), on the other hand. With this aim, the lattice parameter of the cubic unit cell of the material of the buffer sublayer a should be chosen so as to ensure that the translation along the $\langle 112\rangle$ direction in this unit cell will be close to a multiple value of the translation along $\langle 1\bar{1}00\rangle$ Al_2O_3, i.e., $a\sqrt{2}\sqrt{3} = n \times 2.747$ Å, where 2.747 Å is the length of the translation along $\langle 1\bar{1}00\rangle$ Al_2O_3 and n is an integer, whence $a = 1.125n$ (Å). Since the lattice parameters of hexagonal Ga, In, and Al nitrides and related solid solutions range within 3.11–3.25 Å and the cubic materials available in practice have the lattice parameters a ranging within 2.5–13 Å, it is possible to prepare a buffer sublayer from a material with the lattice parameter a close to $a = 1.125n$ (Å), where $n = 3$, 4, 6, or 8. For n equal to 5, 7, or 9, the translations along the $\langle 112\rangle$ and $\langle 110\rangle$ directions of the {111} surfaces of the buffer sublayer are not multiples of the translations along the $\langle 1\bar{1}00\rangle$ and $\langle 11\bar{2}0\rangle$ directions of the semiconductor nitride films. Note that, in growing a heteroepitaxial semiconductor nitride film with a polytype structure of the zinc blende type, the material of the buffer sublayer can also be chosen proceeding from the conditions formulated above.

Elimination of the 30° rotation renders the natural cleavage planes of sapphire and semiconductor nitride parallel to one another. This circumstance allows a Fabry–Perot resonator for a heterolaser to be manufactured using natural cleavage planes of the films.

A heteroepitaxial buffer sublayer can be prepared from cubic materials having crystal lattices of various types such as α–Fe, NaCl, and spinel. Buffer sublayers can also be prepared from dielectrics (e.g., MgO, In_2CdO_4), conducting materials (niobium, hafnium, scandium, and titanium nitrides and carbides and related solid solutions), and metals (niobium and tantalum). A buffer sublayer prepared from a conducting material can simultaneously play the role of one of the contacts (electrodes) in a semiconductor device.

The use of several buffer sublayers may provide still better matching of the lattice parameters and thermal expansion coefficients of a sapphire substrate and a semiconductor film.

We started the experimental studies with the aim of checking this suggestion. Our experiments confirmed that a heteroepitaxial buffer sublayer prepared, e.g., from {111} Nb eliminated the 30° rotation of the (0001) AlN film with respect to the (0001)-oriented sapphire substrate. In this case, the lattice mismatch along the mutually parallel directions $\langle 1\bar{1}00\rangle$ $Al_2O_3 \| \langle 112\rangle$ Nb and $\langle 11\bar{2}0\rangle$ $Al_2O_3 \| \langle 110\rangle$ Nb was less than 2%. A thin {111} niobium nitride film formed subsequently on the niobium layer surface, and the (0001) AlN film deposited onto the niobium nitride had the contact along the flat atomic planes having the same symmetry and almost the same (to within 0.1%) translations. The 30° rotation between the $\langle 1\bar{1}00\rangle$ Al_2O_3 and $\langle 1\bar{1}00\rangle$ AlN directions in the $(11\bar{2}0)$ plane of the Al_2O_3 substrate was eliminated with the aid of a {111} NbN buffer sublayer. In this case, the lattice mismatch along the mutually parallel $\langle 1\bar{1}00\rangle$ Al_2O_3 and $\langle 112\rangle$ NbN directions was less than 2% and the contacting heteroepitaxial (111) NbN and (0001) AlN layers had almost identical flat atomic lattices.

The heteroepitaxial Nb, NbN, and AlN films were deposited onto the (0001) and $(11\bar{2}0)$ substrates by the method of magnetron sputtering. The orientational relationships, determined by the method of X-ray diffraction, were as follows:

$$(0001)\langle 1\bar{1}00\rangle Al_2O_3 \| \{111\}\langle 112\rangle NbN \| (0001)\langle 1\bar{1}00\rangle AlN$$

and

$$(11\bar{2}0)[1\bar{1}00]Al_2O_3 \| \{111\}[112]NbN \| (0001)[1\bar{1}00]AlN.$$

It should be noted that the orientational relationships obtained for the heteroepitaxial (111) Nb film on the (0001) Al_2O_3 substrate and the (111) NbN film on the $(11\bar{2}0)$ Al_2O_3 substrate are consistent with the data reported in [3] and [4], respectively.

Thus, it is shown that the 30° rotation of the semiconductor (0001) nitride film with respect to the (0001)- or $(11\bar{2}0)$-oriented sapphire substrate can be eliminated with the aid of a buffer sublayer made from a cubic material with the unit cell parameter close to $a = 1.125n$ (Å) and with the $\langle 11\bar{2}\rangle$ direction in the {111} surface parallel to the $\langle 1\bar{1}00\rangle$ direction of the substrate surface.

REFERENCES

1. H. Morkos, S. Strite, G. Gao, *et al.*, J. Appl. Phys. **76**, 1363 (1994).
2. M. I. Kotelyanskiĭ, I. M. Kotelyanskiĭ, and V. B. Kravchenko, Patent Application PCT/RU 98/00397 (25 November 1998).
3. K. Masek and V. Matolin, Thin Solid Films **317**, 183 (1998).
4. I. P. Noskov, Yu. V. Titenko, F. I. Korzhinskiĭ, *et al.*, Kristallografiya **25**, 878 (1980) [Sov. Phys.–Crystallogr. **25**, 504 (1980)].

Translated by L. Man

Technical Physics Letters, Vol. 26, No. 2, 2000, pp. 165–167. Translated from Pis'ma v Zhurnal Tekhnicheskoĭ Fiziki, Vol. 26, No. 4, 2000, pp. 67–71.

Generation of Electromagnetic Waves by a Rotating Cylindrical Electron Layer

V. V. Dolgopolov and Yu. V. Kirichenko

Kharkov Institute of Physics and Technology, Ukrainian State Scientific Center, Akademicheskaya ul. 1, Kharkov, 310108 Ukraine

Received July 26, 1999

Abstract—Generation of electromagnetic waves by electrons orbiting in crossed radial electrostatic and axial magnetic fields was studied. Frequencies and increments of the generated waves were calculated. The wave increments increase with the frequency for sufficiently large values of the radial electrostatic field strength. Strong radial electrostatic fields may considerably magnify the frequencies of waves generated in the systems.

Previously, we theoretically studied the generation of electromagnetic waves by electrons rotating about the axis of a cylindrical resonator in a radial electrostatic field or in crossed radial electrostatic and axial magnetic fields [1–3]. The consideration was restricted to cases where electrons generate and enhance free intrinsic oscillations that are uniform along the resonator axis of the cylindrical resonator. Frequencies ω of the generated waves were found to satisfy the condition $\omega \le mv/r$, where r is the radius of the electron layer, v is the azimuthal velocity of electrons, and m is the harmonic number (azimuthal wavenumber). According to this condition, the frequencies of generated waves increase with the wave number m. However, the increments of these waves rapidly decrease with increasing m. The latter circumstance hinders the obtaining of high frequencies by using large m values.

In this work, the generation of electromagnetic waves by electrons orbiting in crossed radial electrostatic and axial magnetic fields was studied in the case of nonzero axial wavenumbers k (i.e., there are waves running along the resonator axis). When electrons are absent, there are no waves with the frequency ω, axial wavenumbers k, or azimuthal quantum numbers m satisfying the above condition in the resonator (the resonator is close). It is shown that, in the presence of electrons, oscillations can occur with the frequencies $\omega \simeq mv/r$ and the increments increasing with m. This allows us to hope that high-frequency (submillimeter) oscillations can be obtained in the system studied under the conditions described below.

In the cylindrical coordinates r, φ, z, the resonator is represented by a cavity ($a < r < b$) unlimited along the z axis and limited by metal on the surfaces $r = a$ and $r = b$. The potential difference between the central rod or wire ($r < a$) and the sheath ($r > b$) determines the constant radial electrostatic field $E(r)$ ($\partial E/\partial\varphi = 0$, $\partial E/\partial z = 0$). The magnetic field B, which is constant in time and space, is directed along the z axis. The electron density n_e undisturbed by the electromagnetic field depends only on the space coordinate r:

$$\begin{aligned} n_e(r) &= 0 \quad \text{for} \quad r \le r_- \quad \text{and} \quad r \ge r_+, \\ n_e(r) &> 0 \quad \text{for} \quad r_- < r < r_+, \quad a < r_- < r_+ < b. \end{aligned} \tag{1}$$

Using the nonrelativistic equations of motion with neglect of the constant electric and magnetic fields induced by electrons, we obtain expressions for the electron rotation velocity

$$v = \frac{\omega_0 r}{2}\left\{1 \pm \left(1 + \frac{4eE}{m_e\omega_c^2 r}\right)^{1/2}\right\}, \tag{2}$$

where $\omega_c = eB/m_e c$ is the electron gyro frequency; e and m_e are the charge and mass of an electron, respectively; and c is the velocity of light. Assuming that dependence of the electromagnetic fields and the electron density and velocity perturbations on the coordinates φ, z, and time t is described by the exponential term $\exp[i(m\varphi + kz - \omega t)]$, from the Maxwell equations, linearized continuity equation, and linearized nonrelativistic equation of motion of electrons we derive three equations for the electric field components E_r, E_φ, and E_z of a wave in the resonator cavity. An analysis of this set of equations leads to the following relationships under the condition that $\omega \sim mv/r$:

$$E_z \sim \frac{v}{c}E_\varphi \sim \frac{v}{c}E_r. \tag{3}$$

Assuming these relationships to be valid, which makes it possible to neglect the field component E_z in two equations of the set, we introduce an error of the order of v^2/c^2 that falls within the limits of accuracy determined by neglect of the relativistic effects. The equations

for the components E_r and E_φ in the region $a < r < b$ have the final form

$$E_r \simeq -\frac{i}{m}\frac{d}{dr}(rE_\varphi), \tag{4}$$

$$\frac{d}{dr}\left\{r\varepsilon\frac{d}{dr}(rE_\varphi) + mr\frac{\bar{\omega}_c\Omega^2}{\omega_m w}E_\varphi\right\} = m\frac{\bar{\omega}_c\Omega^2}{\omega_m w}\frac{d}{dr}(rE_\varphi) + m^2\left\{\varepsilon + \frac{\bar{\omega}_c\Omega^2}{\omega_m^2 w}\left(\frac{dV}{dr} - \frac{V}{r}\right)\right\}E_\varphi, \tag{5}$$

where

$$\varepsilon = 1 - \frac{\Omega^2}{w}, \quad \omega_m = \omega - \frac{mV}{r}, \quad \Omega = \left(\frac{4\pi e^2 n_e(r)}{m_e}\right)^{1/2},$$

$$w = \omega_m^2 - \bar{\omega}_c\left(\frac{dV}{dr} + \frac{V}{r} - \omega_c\right), \quad \bar{\omega}_c = 2\frac{V}{r} - \omega_c.$$

Equation (5) is valid under the condition

$$\left|\frac{\omega^2}{c^2} - k^2\right| r^2 \ll 4|m|. \tag{6}$$

Since the axial wavenumber k will not enter into the dispersion equation, inequality (6) can always be satisfied by proper choice of k ($|k| \simeq |\omega/c|$). Taking into account that the electron layer is narrow, that is,

$$\delta \equiv \frac{r_+ - r_-}{r_-} \ll 1, \tag{7}$$

equation (5) can be solved as described in [1, 2] by the method of successive approximations in the region $r_- \le r \le r_+$. As a result, to within the first-order terms in the small parameter δ, we obtain the boundary conditions relating the fields in the region $r < r_-$ to the fields in the region $r > r_+$:

$$(rE_\varphi)\big|_{r=r_-} \simeq (rE_\varphi)\big|_{r=r_+},$$

$$\left(r\frac{d}{dr}(rE_\varphi)\right)\Big|_{r=r_+} - \left(r\frac{d}{dr}(rE_\varphi)\right)\Big|_{r=r_-} \simeq -\frac{m^2}{\omega_m^2\big|_{r_-}}FE_\varphi\big|_{r=r-}, \tag{8}$$

where

$$F = \int_{r_-}^{r_+} dr\Omega^2\frac{\Omega^2 - 2eE/m_e r}{\Omega^2 + \omega_c^2 + 2eE/m_e r}. \tag{9}$$

In deriving equations (8) and (9), we took into account that

$$|\omega_m| \ll |\omega|. \tag{10}$$

Since the axial component of the unperturbed electron velocity is equal to zero ($V_\varphi \equiv V$, $V_z = 0$), inequality (10) means that electrons interact with the wave under conditions of Cherenkov resonance. In the regions $a \le r \le r_-$ and $r_+ \le r \le b$, the Langmuir frequency Ω is equal to zero and solutions to equation (5) have the form

$$E_\varphi = A_\pm r^{|m|-1} + \frac{B_\pm}{r^{|m|+1}}, \tag{11}$$

where $A_\pm$ and $B_\pm$ are the integration constants in the regions $r > r_+$ and $r < r_-$, respectively. Joining the solutions in the region $a \le r \le r_-$ with those in the region $r_+ \le r \le b$ by using boundary conditions (8), and the solutions in these regions with those for the fields in a metal (taking into account that the component E_φ is continuous; the component E_r has a jump at the boundaries $r = a$, $r = b$; and the field in a metal decreases exponentially), we arrive at the dispersion equation

$$\omega_m^2\big|_{r=r_-} = \frac{|m|}{2r_-}F\frac{(1-\zeta)(\eta-1)}{\eta-\zeta}(1 - i\Delta), \tag{12}$$

where

$$\Delta = \frac{V}{r_- c}\left(\frac{|m|V}{2\pi r_-}\right)^{1/2} \times \frac{\zeta(\eta-1)^2 b\sigma_b^{-1/2} + (1-\zeta)^2\eta a\sigma_a^{-1/2}}{(\eta-1)(\eta-\zeta)(1-\zeta)} \ll 1; \tag{13}$$

$\eta = (r_-/a)^{2|m|} > 1$; $\zeta = (r_-/b)^{2|m|} < 1$; and σ_a and σ_b are the conductivities of the metal wire and resonator wall, respectively. The inequality in (13) is satisfied due to large values of the metal conductivities σ_a and σ_b. It follows from equation (13) that the quantity Δ decreases rapidly with increasing $|m|$ at large $|m|$ values. According to condition (10), the wave frequency is determined by the relationship

$$\omega \simeq \frac{mV}{r}; \tag{14}$$

that is, it increases linearly with the modulus of the wavenumber m. The wave increment $\mathrm{Im}(\omega) = \mathrm{Im}(\omega_m)$ is determined by equation (12), which always provides solutions increasing with time. For $F > 0$, the growth of waves is caused by dissipation effects (related to finite Δ values). The increments of these waves are small

and decrease with increasing modulus of the wavenumber m. For $F < 0$, the increments are not related to the wave dissipation and increase with $|m|$ ($\mathrm{Im}(\omega) \sim |m|^{1/2}$). For this growth to take place, according to formula (9), the wire must carry a positive potential $E > 0$ and the quantity $2eE(r_-)/m_e r_-$ must be greater than the average square $\overline{\Omega^2}$ of the Langmuir frequency. Therefore, the radial electrostatic field can considerably increase the frequency of the generated waves independently of the magnetic field strength.

REFERENCES

1. V. V. Dolgopolov, Yu. V. Kirichenko, Yu. F. Lonin, and I. F. Kharchenko, Zh. Tekh. Fiz. **68**, 91 (1998) [Tech. Phys. **43**, 959 (1998)].
2. V. V. Dolgopolov, M. V. Dolgopolov, and Yu. V. Kirichenko, Izv. Vyssh. Uchebn. Zaved., Radioélektron. **40**, 16 (1997).
3. V. V. Dolgopolov, Yu. V. Kirichenko, and I. F. Kharchenko, Izv. Vyssh. Uchebn. Zaved., Radioélektron. **42**, 33 (1999).

Translated by R. Tyapaev

Technical Physics Letters, Vol. 26, No. 2, 2000, pp. 168–169. Translated from Pis'ma v Zhurnal Tekhnicheskoĭ Fiziki, Vol. 26, No. 4, 2000, pp. 72–76.

Functional Materials Based on the Complex Compounds of Germanium

Ya. Lepikh and V. A. Smyntyna

Odessa State University, Odessa, Ukraine

Special Design Bureau, Element Company, Odessa, Ukraine

Received March 23, 1999; in final form, October 5, 1999

Abstract—A new class of functional materials based on the coordination compounds of germanium is developed and studied. The materials are capable of forming transparent films from aqueous solutions at room temperature and exhibit high technological properties. Physicochemical and electrophysical characteristics of some samples are presented. © *2000 MAIK "Nauka/Interperiodica".*

Substantial improvement of parameters and creation of new classes of the devices of functional electronics can be achieved by development of novel functional materials with predetermined properties [1–3]. Germanium compounds are among the substances that attract the attention of researchers in connection with this task. It was demonstrated, for example, that cadmium thiogermanate Cd_4GeS_6 is a rather effective photoconductor and piezoelectric [4]. Germanium coordination compounds with organic molecules are much less studied in this respect, although the structure and physicochemical properties of materials based on these compounds are substantially more versatile than those of inorganic semiconductors.

We have studied the physicochemical and electrophysical properties of several mono- and heteroligand germanium coordination compounds with organic polybasic acids.

Germanium complex compounds—germanium complexonates (GCs)—with intramolecular hydrogen bonds and isomerism (tautomerism), such as germanium complexes with oxyethylidenediphosphonic (Oedph) or diethylenetriaminepentaacetic (Dtpa) acids, form transparent films with high transmittance under certain conditions. It was demonstrated that the physicochemical and optical properties of GCs can be modified by forming various salts with ions of other metals and organic cations (tartaric acid, $NH_4F \cdot HF$, NaF, ethyl alcohol, etc.).

Study of the physicochemical parameters of GC films showed that they can be classified as supermolecular systems with special properties, in which the molecular structure determines, in particular, the optical characteristics. Thus, the properties of the films (e.g., optical absorption) can be controlled by selecting certain types of structures.

The GC-based materials exhibit high technological properties. They are capable of forming transparent films from aqueous solutions at room temperature, which is apparently explained by certain features of their molecular structure (the presence of a germanium-containing intracomplex anion capable of binding to both protons and other cations). These molecular systems can also take part in intermolecular interactions and in polymerization reactions. The laws of film formation and the dependence of this process on the composition, the molar ratio of the components, and other factors were determined. The materials are stable in air, possess sufficient mechanical strength, and exhibit high adhesion to the surface of substrates made from different materials used in microelectronics.

The thickness of GC films was varied from 0.5 to 20 μm. The films with a thickness of up to 1 μm possess a fine-grained structure and an optically smooth surface. An increase in the thickness leads to changes in the film structure, as manifested by the formation of crystalline macrodomains with a size of several tens of microns and the formation of domainlike areas with an ordered structure. The existence of domains allows one to suggest that GCs possess piezoelectric properties.

Data on the transmittance of some synthesized GC films measured using an SF-16 spectrophotometer are presented in Tables 1 and 2.

The thickness of the films deposited onto substrates made of a soda glass was 5 μm. As is seen, the film transmittance increases by 1–6% in the 1100–1200 nm wavelength range. The films of a Ba–Ge–Dpta compound exhibits a relatively uniform transmission spectrum in the wavelength range studied, with the maximum at $\lambda = 1200$ nm; for Ge–Oedph–$NH_4F \cdot HF$, the transmittance has an additional maximum at $\lambda = 1030$–1040 nm, which proves the possibility of controlling the optical parameters of GCs by introducing various admixtures in the course of synthesis.

If there is only a Ge–Oedph complex in the solution, the electric resistance of the optically transparent GC

1063-7850/00/2602-0168$20.00 © 2000 MAIK "Nauka/Interperiodica"

Table 1. Transmission spectrum of Ba–Ge–Dtpa film

Wavelength, nm	Transmittance, %	Wavelength, nm	Transmittance, %
316	98.5	900	99.5
330	98.5	920	99.5
340	98.5	940	99.5
400	99.5	960	99.5
500	99.5	980	99.0
510	100.0	1000	99.0
520	100.0	1010	98.0
530	100.0	1020	98.0
540	100.0	1030	98.0
560	100.0	1040	99.0
580	99.5	1050	98.5
600	99.0	1060	97.5
620	99.0	1070	98.0
640	99.0	1080	98.0
660	99.5	1090	97.5
680	99.5	1100	100.0
700	100.0	1110	98.0
720	100.0	1120	99.0
740	100.0	1130	100.0
760	100.0	1140	101.0
780	100.0	1150	100.5
800	100.0	1160	102.5
820	100.0	1170	100.0
840	100.0	1180	101.0
860	100.0	1190	101.0
880	100.0	1200	102.0

Table 2. Transmission spectrum of Ge–Oedph–$NH_4F \cdot HF$ film

Wavelength, nm	Transmittance, %	Wavelength, nm	Transmittance, %
316	98.5	900	99.0
330	98.5	920	99.5
340	98.5	940	99.5
400	100.0	960	99.5
500	100.0	980	99.0
510	100.0	1000	99.0
520	100.0	1010	98.0
530	100.0	1020	98.0
540	100.0	1030	107.0
560	100.0	1040	107.0
580	100.0	1050	98.0
600	99.5	1060	100.0
620	99.0	1070	98.0
640	99.0	1080	98.0
660	99.0	1090	97.5
680	99.5	1100	102.0
700	100.0	1110	98.0
720	100.0	1120	99.0
740	100.0	1130	100.0
760	100.0	1140	101.0
780	100.0	1150	102.0
800	99.5	1160	102.5
820	100.0	1170	103.0
840	100.0	1180	104.0
860	100.0	1190	104.5
880	100.0	1200	103.0

films is higher than 10^{10} Ω. The introduction of compounds such as $NH_4F \cdot HF$ and NaF into the solution decreases the resistance of GC films down to 1.5×10^8 Ω. The introduction of other inorganic substances, such as $BaCO_3$, leads to a slight increase in the electric resistance. The permittivity of the films varied within $\varepsilon = 3$–8 depending on the compositions of the GCs, which allows one to use the material in UHF devices.

The results of the study of GC films indicate that these materials can be used in optoelectronics and acoustooptics, which is proved by the experimental prototypes of new optical devices.

REFERENCES

1. Y. Nakagawa, Y. Gomi, and T. Okada, J. Appl. Phys. **61**, 5012 (1987).
2. V. A. Golenishchev-Kutuzov, S. A. Migachev, and S. P. Mironov, *Acoustoelectronics and Physical Acoustics* (Kazan, 1988), pp. 20–29.
3. Yu. V. Ilisavskiĭ, L. A. Kulakova, B. T. Melekh, *et al.*, in *Abstracts of International Scientific-Technical Conference, St. Petersburg, Russia* (1993), p. 70.
4. *Chemistry and Technology of Rare and Trace Elements* (Moscow, 1976), Part 2.

Translated by A. Chikishev

Technical Physics Letters, Vol. 26, No. 2, 2000, pp. 170–172. Translated from Pis'ma v Zhurnal Tekhnicheskoĭ Fiziki, Vol. 26, No. 4, 2000, pp. 77–82.

The Mechanism of the Streamer Stage of Breakdown in Crystal Dielectrics

V. D. Kulikov

Tomsk Polytechnical University, Tomsk, Russia

Received July 16, 1999

Abstract—A model of the initial stages of electric breakdown in crystals is suggested, which is based on the mechanisms of electron transitions in the valence band of a dielectric. © *2000 MAIK "Nauka/Interperiodica".*

The main phases of breakdown, namely, the loss of dielectric strength and the destruction of material, have been investigated in sufficient detail (see, for example, [1, 2]). However, the initial stages of breakdown in solid dielectrics involving the formation of streamer discharges (glow channels of high conductance) and partial breakdown have yet to be studied. In particular, one still fails to distinguish the glow of streamer discharge against the background of plasma glow in the breakdown channel [3]. The crystallographic orientation of breakdowns in ionic crystals is not entirely clear [4–6].

It was the objective of this study to construct a model of the initial stages of breakdown.

The main laws of partial breakdown in alkali-halide crystals in pulsed and constant electric fields are as follows [1–9]:

1. The breakdown in the case of alkali-halide crystals comes from the positively charged electrode (anode breakdown).

2. In LiF and NaCl crystals, the breakdowns are oriented in the ⟨110⟩ direction, while in the KCl, KBr, and RbCl crystals, they are oriented in the ⟨100⟩ direction.

3. The values of bulk-average threshold field intensities of partial breakdown decrease in the series LiF > NaCl > KCl > KBr > RbCl and amount to ~10^5–10^6 V/cm. The velocity of motion of the breakdown channel reaches ~10^7–10^8 cm/s.

A model of the initial stages of breakdown may be provided by the mechanism of formation of a channel of electron excitation (streamer) in the crystal, based on the notions of the band structure of dielectrics and the Auger electron transitions. This approach may be provided by the observed correlation between data on the orientation of breakdowns in crystals of LiF, NaCl (⟨110⟩ direction), KCl, and KBr (⟨100⟩), and the band structure of these crystals.

For LiF and NaCl, the 2*p* energy levels of cations in the valence band of the crystal lie much lower than the 3*p* energy levels of anions (~40 eV lower for LiF and ~25 eV lower for NaCl). The figure gives the position of single-electron energy levels for NaCl, KCl, and KBr crystals [10]. For KCl, the 3*p* energy level of cations is ~10 eV lower than the 3*p* energy level of Cl^- ions (see Fig. 1c). In a KBr crystal, the 3*p* energy level for K^+ ion is located ~1.5–2 eV lower than the 4*p* level for Br^- ion (see Fig. 1e).

An external field applied to a dielectric produces a band bending with a maximum value in the vicinity of the electrode inhomogeneity. One can assume that the streamer motion begins with the appearance of two holes on the 3*p* level of the Cl^+ ion (see Fig. 1b). These holes may form, for example, as a result of interatomic Auger decay of a Na^{++} 2*p*-hole according to the scheme [11, 12]

$$Na^{++}(2p)^{-1} \longrightarrow Cl^+(3p)^{-2} + e. \quad (1)$$

A further streamer motion is associated with the relaxation of these holes and injection of electrons into the conduction band. In the case of LiF and NaCl crystals, the decay of holes cannot proceed from the low-lying 2*p* energy levels of the cation. Most probably, hole relaxation proceeds from the neighboring Cl^- anion arranged in the ⟨110⟩ direction and, possibly, along two pathways: first, by an interatomic Auger transition with charge transfer from the 3*p* level of Cl^- (transition 1) and the subsequent injection of an Auger electron into the conduction band according to the scheme

$$Cl^-(3p) \longrightarrow Cl^+(3p)^{-2} + e; \quad (2)$$

second, by a resonance transition of an electron from the 3*s* level of Cl^- to the 3*p* level of Cl^+ (transition 2) with the subsequent interatomic Auger decay of the 3*s*-hole of Cl^0 according to the scheme

$$Cl^0(3s)^{-1} \longrightarrow Cl^+(3p)^{-2} + e. \quad (3)$$

It is of interest to estimate the value of the field strength necessary for transitions 1 and 2. The probability of transition 1 becomes nonzero provided that the minimum energy gap between 3*p* levels of neighboring ions (see Fig. 1b) is ~10 eV. This energy is required to transfer an Auger electron to the conduction band. In order to realize the resonance transition of an electron from the 3*s* level of Cl^- to the 3*p* level of Cl^+, one must

raise the 3*s* level by ~12 eV [10]. Given the average distance between neighboring atoms in the lattice of ~3 Å (the distance between $Cl^- - Cl^-$ is ~4 Å), the external field intensity must be ~$(2.5–3) \times 10^8$ V/cm. This level of field strength (exceeding the breakdown values by two to three orders of magnitude) may only be realized in the vicinity of the electrode inhomogeneity or at the end of the conducting channel. In a vacuum diode, explosive electron emission on electrode microinhomogeneities proceeds at an average field value of 10^6 V/cm; in so doing, it is assumed that fields of ~10^8 V/cm are required for the effect to take place [13].

Apparently, a factor of critical importance for the increase in the field strength on electrode inhomogeneities is the absence of the shunting effect of surface currents [9]. The effect of delay of surface currents is attained for a high value of the rate of field rise (~10^{12} V/cm s).

One must further take into account that two holes on a chlorine ion form an effective Cl^+ charged center. The e^+ charge at a distance of 3–4 Å produces a field strength of ~3×10^7 V/cm, which increases to ~ 3×10^8 V/cm for 1 Å, thus providing for additional electric fields.

Note that electric fields as high as ~10^8 V/cm are required in order to realize the suggested model. Possibly, in case the energy levels of filled *p*-orbitals of anion increase on the energy scale, lower values of the field strength would be required in the field of the neighboring hole. This is apparently associated with the fact that, out of three orbitals of the *p*-shell, only the orbital oriented in the direction of the hole takes part in the charge transfer. The effective distance over which the hole field acts upon the electron of the given orbital is less than the interatomic distance, and, as a result, the necessary (10–20 eV) increase in the orbital energy value is provided for.

In KCl and KBr crystals, the relaxation of holes on Cl^+ and Br^+ ions apparently proceeds through the 3*p* levels of the cation. For a resonance transfer of an electron, the 3*p* level of K^+ in KCl must be raised by ~12 eV and in KBr by ~2–3 eV (see Fig. 1e). The subsequent relaxation of the hole on K^{++} in a KCl crystal possibly proceeds in two ways (analogous to those considered above in the case of NaCl), namely, by interatomic Auger decay from the 3*p* level of Cl^- (transition 1) or by a resonance charge transfer from the 3*s* level of Cl^- with the subsequent interatomic Auger decay of the 3*s*-hole (transition 2; see Fig. 1d). For a KBr crystal, the 3*p*-hole of K^{++} ion relaxes by way of Auger decay from the Br^- ion.

In this case, the direction of streamer motion for KCl and KBr crystals corresponds to the ⟨100⟩ crystal orientation.

It follows from this model that the hole relaxation may proceed only in the direction of the negative electrode. This is confirmed by the anode character of breakdown.

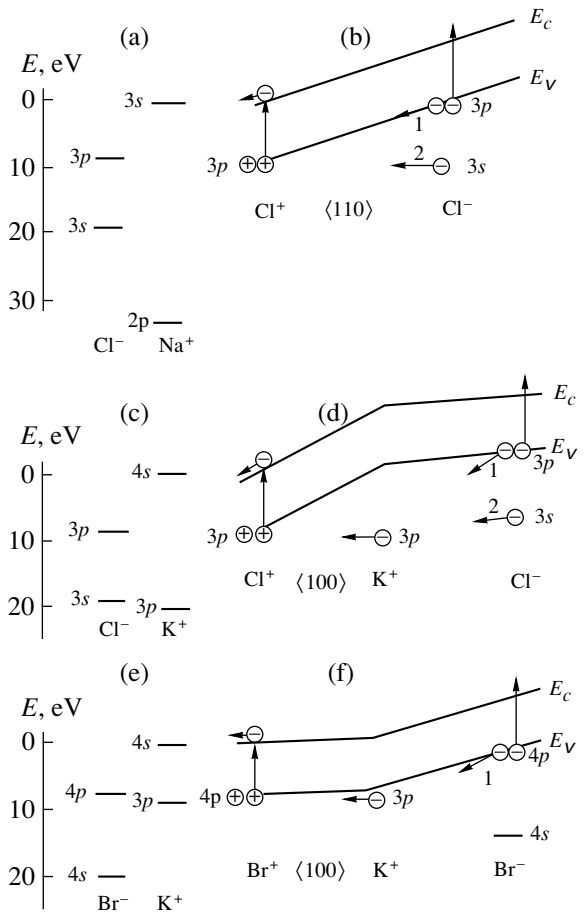

Fig. 1. Schematic diagrams showing (a, c, e) the ion energy levels in crystalline NaCl, KCl, and KBr and (b, d, f) the band structure of crystals in the presence of a strong electric field. E_c and E_v denote the energy level of the conduction band bottom and of the valence band top, respectively; (1, 2) possible electron transitions: (a, b) NaCl, (c, d) KCl, (e, f) KBr.

In alkali-halide crystals, the propagating streamer channel produces free electrons and holes. The lifetime of electrons is short, ~10^{-10}–10^{-11} s. However, an electron-hole recombination is accompanied by the formation of an exciton with energy levels in the forbidden band and a lifetime of ~10^{-8} s. An electron captured to exciton states is readily transferred to the conduction band of the dielectric; this maintains a high level of electron number density along the streamer channel. It appears, however, that in the presence of ~10^6–10^7 V/cm fields, a greater part of the charge carriers are immediately accelerated to the energies of interband ionization. This inference may be supported by the fact of low intensity of exciton glow against the background of glow of the discharge plasma.

Therefore, the suggested model of the initial stages of partial breakdown based on electron transitions in

the valence band of a crystal provides an adequate explanation for the available experimental facts related to the electrode and crystallographic orientation of breakdowns. The high rate of field rise (~10^{12} V/cm s) rules out the possibility of the shunting effect of surface currents, as a result of which the value of field strength at the conducting inhomogeneities may reach the necessary level (~10^8 V/cm).

REFERENCES

1. G. I. Skanavi, *Physics of Dielectrics (Strong Field Region)* (Fizmatgiz, Moscow, 1958).
2. A. A. Vorob'ev and G. A. Vorob'ev, *Electric Breakdown and Destruction of Solid Dielectrics* (Vysshaya Shkola, Moscow, 1966).
3. V. M. Lisitsyn and V. I. Oleshko, Pis'ma Zh. Tekh. Fiz. **9**, 15 (1983) [Sov. Tech. Phys. Lett. **9**, 6 (1983)].
4. M. E. Gaspari, Phys. Rev. **98**, 1679 (1955).
5. L. A. Chernozatonskiĭ, Pis'ma Zh. Éksp. Tekh. Fiz. **38**, 225 (1983) [JETP Lett. **38**, 265 (1983)].
6. V. V. Zubritskiĭ, Zh. Tekh. Fiz. **61**, 82 (1991) [Sov. Phys. Tech. Phys. **36**, 1123 (1991)].
7. A. L. Mironov, I. A. Zubarev, V. G. Shpak, and V. V. Bykov, Zh. Tekh. Fiz. **60**, 203 (1990) [Sov. Phys. Tech. Phys. **35**, 1354 (1990)].
8. Yu. N. Vershinin, A. V. Vodichev, and S. I. Petrukhovskiĭ, Dokl. Ross. Akad. Nauk **309**, 346 (1998).
9. V. D. Kulikov and V. M. Lisitsyn, Deposited at and Available from VINITI, No. 7202 V (1985).
10. J. C. Slater, *The Self-Consistent Field for Molecules and Solids* (McGraw-Hill, New York, 1974; Mir, Moscow, 1978).
11. É. S. Parilis, *Auger Effect* (Fan, Tashkent, 1969).
12. A. Kikas and M. Elango, Phys. Status Solidi B **130**, 211 (1985).
13. S. P. Bugaev, Yu. E. Kreĭndel, and P. M. Shchanin, *Wide Electron Beams* (Énergoatomizdat, Moscow, 1984).

Translated by H. Bronsteĭn

Technical Physics Letters, Vol. 26, No. 2, 2000, pp. 173–174. Translated from Pis'ma v Zhurnal Tekhnicheskoĭ Fiziki, Vol. 26, No. 4, 2000, pp. 83–87.

Estimation of the Parameters of the Spectral Components of Second-Order Nonlinear Systems

V. A. Dvinskikh and S. V. Frolov

Saratov State University, Universitetskaya ul. 42, Saratov, 410601 Russia

Received July 12, 1999

Abstract—A nonlinear conservative Lyapunov system is analyzed, and satisfactory agreement between the analytical solution and the results of numerical analysis is obtained. Oscillation spectra of a nonautonomous nonlinear system that is close to the Lyapunov one are discussed. *© 2000 MAIK "Nauka/Interperiodica".*

It is well known [1] that the discrete Fermi transformation is characterized by low resolution in detecting the fine structure of a spectrum. An analysis of the oscillation spectrum by parametric methods [2], which require a pilot sequence of solutions, also gives no means of separating components with close frequencies from other quasiperiodic oscillations. For these reasons, we have used a method for calculating parameters of the spectral components based on the approximation of the pilot sequence by a first-order trigonometric polynomial [3] that makes it possible to increase the resolution.

Consider the equation of a conservative nonlinear Lyapunov system

$$\frac{d^2x}{dt^2} + x + x^3 = 0, \tag{1}$$

and go over to the new argument

$$t \cong \tau(1 + h_2c^2 + h_4c^4 + \ldots), \tag{2}$$

where h_2, h_4, … are the constants to be calculated. In terms of this new argument, equation (1) acquires the form

$$\frac{d^2x}{d\tau^2} + (x + x^3)(1 + h_2c^2 + h_4c^4 + \ldots) = 0. \tag{3}$$

A solution to this equation is sought in the form of a series [4]

$$x(\tau) = c\cos\tau + c^3x_3(\tau) + c^5x_5(\tau) + \ldots, \tag{4}$$

where $x_3(\tau)$, $x_5(\tau)$, … are periodic functions of the argument τ with the period 2π that satisfy the initial conditions

$$\begin{aligned} &x_3(0) = x_5(0) = \ldots = 0; \\ &\left.\frac{dx_3}{d\tau}\right|_0 = \left.\frac{dx_5}{d\tau}\right|_0 = \ldots = 0. \end{aligned} \tag{5}$$

In this case, we have

$$\frac{d^2x_3}{d\tau^2} + x_3 = \left(\frac{3}{4} - 2h_2\right)\cos\tau + \frac{1}{4}\cos 3\tau, \tag{6}$$

and the periodicity condition (i.e., the condition that the coefficient of $\cos\tau$ is equal to zero) yields the value

$$h_2 = 3/8. \tag{7}$$

Then, taking into account the initial conditions (5), we

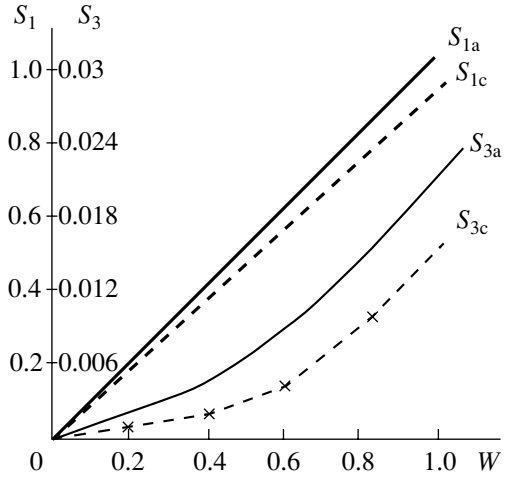

Fig. 1.

1063-7850/00/2602-0173$20.00 © 2000 MAIK "Nauka/Interperiodica"

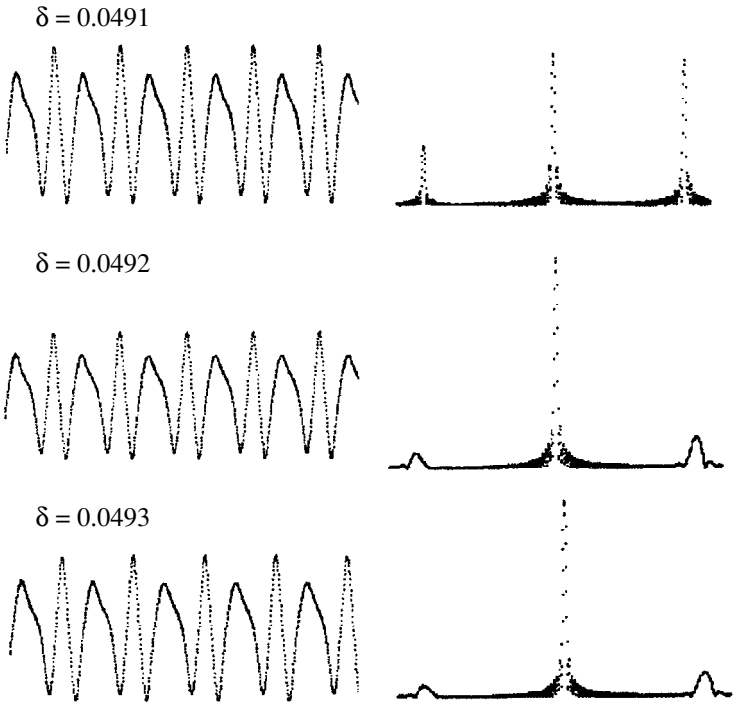

Fig. 2.

obtain from equation (6) that

$$x_3(\tau) = \frac{1}{32}(\cos\tau - \cos 3\tau). \tag{8}$$

The function $x_5(\tau)$ satisfies the equation

$$\frac{d^2x_5}{d\tau^2} + x_5 = \left(-2h_4 + \frac{57}{128}\right)\cos\tau + \frac{3}{16}\cos 3\tau - \frac{3}{128}\cos 5\tau, \tag{9}$$

which provides the equality

$$h_4 = 57/256. \tag{10}$$

Considering only the solutions found, we obtain the function

$$x(\tau) \cong x_1\cos\tau - x_3\cos 3\tau - \frac{c^5}{1024}\cos 5\tau, \tag{11}$$

where

$$x_1 = c + \frac{c^3}{32} + \frac{23c^5}{1024}, \quad x_3 = \frac{c^3}{32} - \frac{3c^5}{128}$$

with the period

$$T \cong 2\pi\left(1 - \frac{3c^2}{8} - \frac{57c^4}{254}\right). \tag{12}$$

In addition, we have solved equation (8) numerically by the fourth-order Runge–Kutta method with a step of 0.05 for various initial conditions *W*. Figure 1 shows the amplitudes of the first and the third harmonics as functions of the argument *W* derived in an analytical form (solid lines) as compared to those obtained numerically (dashed lines). Estimates show that the period obtained numerically is close to that derived analytically. Feigenbaum [5] derived the equation

$$\frac{d^2x}{dt^2} + \delta\frac{dx}{dt} + x^3 = b\sin t \tag{13}$$

with constant coefficients $\delta \ll 1$ and $b < 1$ ($b = 0.9$). Figure 2 displays the time diagrams calculated for δ = 0.0493, 0.0492, and 0.0491 (left panels) and the corresponding spectra (right panels). An analysis of the time dependence demonstrates that, in relation to instability of the transient processes, in the nonlinear system studied an amplitude modulation arises that results in the appearance of side components in the spectrum.

REFERENCES

1. A. S. Dmitriev and V. Ya. Kislov, *Stochastic Oscillations in Radiophysics and Electronics* (Nauka, Moscow, 1989).
2. S. L. Marple, Jr., *Digital Spectral Analysis* (Prentice-Hall, Englewood Cliffs, N.J., 1987).
3. V. A. Dvinskikh, Zh. Tekh. Fiz. **63**, 168 (1992) [Sov. Phys. Tech. Phys. **37**, 1213 (1992)].
4. I. G. Malkin, *Some Problems in Theory of Nonlinear Oscillations* (Gostekhizdat, Moscow, 1956).
5. M. I. Feigenbaum, Los Alamos Sci. **1**, 4 (1980).

Translated by R. Tyapaev

Technical Physics Letters, Vol. 26, No. 2, 2000, pp. 175–177. Translated from Pis'ma v Zhurnal Tekhnicheskoĭ Fiziki, Vol. 26, No. 4, 2000, pp. 88–94.

Magnetoacoustic Heating of a Flat Layer by Traveling Wave of Current

E. B. Postnikov and S. V. Sobolev

Kursk State Pedagogical University, Kursk, Russia

Received December 9, 1998; in final form, August 26, 1999

Abstract—A study is made of the Cherenkov generation and dissipation of the energy of magnetoacoustic vibrations in a flat metal layer located in the field of two traveling waves of current. It is demonstrated that the temperature field in the layer is in fact nongradient, and the heating rate is much higher than that in the case of previously studied mechanisms. *© 2000 MAIK "Nauka/Interperiodica".*

A promising way of the thermal and acoustic treatment of conducting materials is by resonance excitation of sound vibrations in these materials against the background of a constant strong magnetic field [1, 2].

The purpose of this work was to investigate the acoustic and electromagnetic fields in a homogeneous nonmagnetic flat layer ($\mu = 1$) with the thickness $2z_1$ and specific conductivity σ, which are excited in the Cherenkov mode by traveling current-density waves arranged symmetrically relative to the plane $z = 0$,

$$\begin{aligned}\mathbf{j} &= \{0, j\exp[i(k_0x - \omega t)]\delta(z - z_0), 0\},\\ |z_0| &> |z_1|, \quad j = \text{const}, \quad \operatorname{Im} j = 0\end{aligned} \tag{1}$$

in the presence of a sufficiently strong constant and uniform magnetic field $\mathbf{B} = (B, 0, 0)$. Here, $\omega/k_0 = v$ is the phase velocity of the wave, which exceeds one of the characteristic velocities of propagation of acoustic perturbations. It is assumed that the layer is located in a "light" medium (for example, a gas) possessing the electromagnetic properties of vacuum, under conditions of convective heat exchange with this medium.

1. SOLUTION OF THE VISCOELASTIC PROBLEM

The initial set of equations of magnetoelasticity has the form

$$\begin{cases}\dfrac{\partial^2\mathbf{u}}{\partial t^2} = \left(c_\perp^2 + \gamma_\perp\dfrac{\partial}{\partial t}\right)\Delta\mathbf{u} + \left[\left(c_\parallel^2 + \gamma_\parallel\dfrac{\partial}{\partial t}\right) - \left(c_\perp^2 + \gamma_\perp\dfrac{\partial}{\partial t}\right)\right]\\ \times \operatorname{graddiv}\mathbf{u} - c_a^2\dfrac{\mathbf{B}}{B^2}\times\operatorname{rot}\mathbf{b},\\ \Delta\mathbf{A} - \mu_0\sigma\dfrac{\partial\mathbf{A}}{\partial t} = -\mu_0\sigma\dfrac{\partial\mathbf{u}}{\partial t}\times\mathbf{B}, \quad \mathbf{b} = \operatorname{rot}\mathbf{A}.\end{cases} \tag{2}$$

Here, $\mathbf{u}$ is the displacement vector of a point in the medium; $c_\perp$ and $c_\parallel$ denote the rate of propagation of longitudinal and transverse acoustic waves, respectively; c_a is Alfvén's velocity; $\mathbf{b}$ is the magnetic field perturbation; $\mathbf{A}$ is the vector potential of the field; and the coefficients $\gamma_\perp$ and $\gamma_\parallel$ are expressed in terms of the coefficients ξ of bulk viscosity and η of shear viscosity by the formulas $\gamma_\parallel = (\xi + 4\eta/3)/\rho$ and $\gamma_\perp = \eta/\rho$. With due regard for the fact that, in solids, $c_a \ll c_\perp < c_\parallel$ even at $B \sim 10$ T, we introduce the "longitudinal" $\mathbf{u}_\parallel$ and "transverse" $\mathbf{u}_\perp$ components of the displacement vector $\mathbf{u} = \mathbf{u}_\perp + \mathbf{u}_\parallel$ such that $\operatorname{div}\mathbf{u}_\perp = 0$ and $\operatorname{rot}\mathbf{u}_\parallel = 0$ to derive the following set of equations equivalent to (2):

$$\frac{\partial^2\mathbf{u}_\perp}{\partial t^2} = \left(c_\perp^2 + \gamma_\perp\frac{\partial}{\partial t}\right)\Delta\mathbf{u}_\perp, \tag{3}$$

$$\frac{\partial^2\mathbf{u}_\parallel}{\partial t^2} = \left(c_\parallel^2 + \gamma_\parallel\frac{\partial}{\partial t}\right)\Delta\mathbf{u}_\parallel, \tag{4}$$

$$\Delta\mathbf{A} - \mu_0\sigma\frac{\partial\mathbf{A}}{\partial t} = -\mu_0\sigma\frac{\partial\mathbf{u}}{\partial t}\times\mathbf{B}. \tag{5}$$

On the surface of a layer of a material possessing high (metallic) conductivity, when the skin layer thickness in the direction perpendicular to its surface becomes negligibly small compared to the layer dimensions, the field vector potential $\mathbf{A} = (0, A, 0)$ satisfies the following boundary conditions:

$$\begin{aligned}A|_{z = z_1 + 0} - A|_{z = z_1 - 0} &= 0,\\ \left.\frac{\partial A}{\partial z}\right|_{z = z_1 + 0} - \left.\frac{\partial A}{\partial z}\right|_{z = z_1 - 0} &= -\mu_0 j_0.\end{aligned} \tag{6}$$

Two more boundary conditions on the $|z| = z_1$ surfaces are derived from the requirement of continuity of the

momentum flux density and have the form

$$\left(c_\perp^2 + \gamma_\perp \frac{\partial}{\partial t}\right)\left(\frac{\partial u_z}{\partial x} + \frac{\partial u_x}{\partial z}\right) = 0,$$

$$\left[\left(c_\parallel^2 + \gamma_\parallel \frac{\partial}{\partial t}\right) - 2\left(c_\perp^2 + \gamma_\perp \frac{\partial}{\partial t}\right)\right]\frac{\partial u_x}{\partial x} \qquad (7)$$

$$+ \left(c_\parallel^2 + \gamma_\parallel \frac{\partial}{\partial t}\right)\frac{\partial u_z}{\partial z} = \frac{B}{\rho} j_0,$$

where j_0 is the surface current density to be determined.

Remark 1. In writing the boundary conditions (6) and second boundary condition (7), it is assumed that the quantity j_0 in fact replaces the surface currents arising as a result of incidence of a high-frequency electromagnetic field onto a conducting medium. This, in particular, explains the discontinuity of the vector potential $\partial A/\partial z$ on the boundary $z = z_1$ of the layer [3]. Note further that the fourth unknown constant, which does not appear explicitly in conditions (6)–(7), defines characteristics of the field reflected from the layer and enters into the expressions for A and $\partial A/\partial z$ at $z = z_1 + 0$. The same quantities include the preset traveling wave current density j in (1).

The solution of problem (3)–(7) reduces to the following stages: (i) solving the elastic problem (3)–(4) on the propagation of a wave of the form $\mathbf{f}(z)\exp[i(k_0 x - \omega t)]$; (ii) finding from (5) (with the vector $\mathbf{u}$ in the right-hand part, as obtained above) a vector potential of the electromagnetic field appearing in the layer material; (iii) determining a vector potential of the external magnetic field as the solution of Poisson's equation with a field source (1); and (iv) determining unique solutions for the fields $\mathbf{u}$ and $\mathbf{A}$ by finding the involved constants from boundary conditions (6)–(7).

Equations (3) and (4) determine the conditions for the Cherenkov generation of waves: if the phase velocity v of the current wave exceeds $c_\parallel$, two branches of vibrations (modified transverse and longitudinal) are generated with the wave numbers $\kappa_{\perp,\parallel} = k_{\perp,\parallel} + i\omega^3\gamma_{\perp,\parallel}/2k_{\perp,\parallel}c_{\perp,\parallel}^4$ and $k_{\perp,\parallel} = k_0[(v/c_{\perp,\parallel})^2 - 1)]^{1/2}$. Nonzero components of the displacement vector $\mathbf{u}$ and vector potential $\mathbf{A}$ have the form

$$u_x = -[\kappa_\perp \alpha_1 \cos(\kappa_\perp z) + ik_0\alpha_2 \cos(\kappa_\parallel z)] \times \exp[i(k_0 x - \omega t)],$$

$$u_z = [ik_0\alpha_1 \sin(\kappa_\perp z) + \kappa_\parallel \alpha_2 \sin(\kappa_\parallel z)] \times \exp[i(k_0 x - \omega t)],$$

and

$$A = -[ik_0\alpha_1\beta_\perp \sin(\kappa_\perp z) + \kappa_\parallel \alpha_2\beta_\parallel \sin(\kappa_\parallel z)] \times \exp[i(k_0 x - \omega t)],$$

where $\alpha_{1,2}$ = const and $\beta_{\perp,\parallel} = i\omega\mu_0\sigma B/(\kappa_{\perp,\parallel}^2 + k_0^2 - i\omega\mu_0\sigma)$.

In case v satisfies the inequalities $c_\perp < v < c_\parallel$, only one branch of vibrations is excited with the wave number $\kappa_\perp$ (the second branch is a Rayleigh wave decaying exponentially in depth of the layer).

2. SOLUTION OF THE THERMAL PROBLEM

The energy of coupled acoustic and electromagnetic vibrations in the layer material converts into heat due to viscous and Joule dissipation. Figure 1 shows distributions of the power density of viscous q_γ and Joule q_σ heat release of the sources averaged over the period of vibrations,

$$q_\gamma = \frac{\rho\omega^2}{2}\left[2\gamma_\perp\left(\left|\frac{\partial u_x}{\partial z} + \frac{\partial u_z}{\partial x}\right|^2 + \left|\frac{\partial u_x}{\partial x}\right|^2 + \left|\frac{\partial u_z}{\partial z}\right|^2\right) + (\gamma_\parallel - 2\gamma_\perp)\left|\frac{\partial u_x}{\partial x} + \frac{\partial u_z}{\partial z}\right|^2\right], \quad q_\sigma = \frac{\sigma\omega^2}{2}|A + u_z B|^2,$$

in dimensionless form. The graphs are plotted for an aluminum layer and the second resonance harmonic whose frequency was found from the condition of minimum of the main determinant of the set of boundary conditions (6)–(7). As can be seen, the layer heating has a clearly pronounced bulk character. The use of a source of the Cherenkov type enables one to raise the power of heat release by approximately an order of magnitude compared to previously calculated case [2], when only transverse vibrations of the layer are excited under similar conditions.

Remark 2. It is known that, under conditions of purely induction high-frequency heating, the sources of Joule heat release are localized in a thin surface layer with the characteristic thickness of the order of skin depth. It is easy to show that, in the problem being treated (Fig. 1), the density of the sources of purely Joule surface heating at $z/z_1 = 1$ is of the order of the density of sources of bulk heat release due to viscosity, with the former decreasing exponentially in depth of the layer, (already at $z/z_1 = 0.95$ the value is seven orders of magnitude smaller than the boundary value). This means that, in what follows, the effect of surface induction heating can be ignored. (A similar result for a one-dimensional problem was obtained by Kiselev *et al.* [2].)

Time variation of the depth profile of the layer temperature may be found by solving the heat conductivity

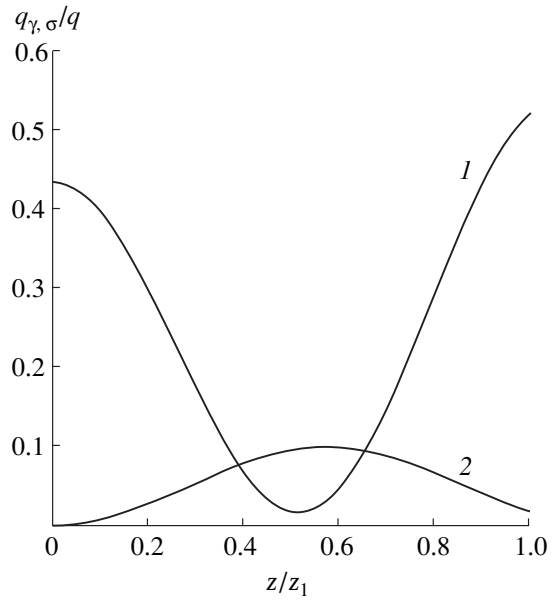

Fig. 1. The distribution of the power density of (*1*) viscous q_γ/q and (*2*) Joule $q_\sigma \times 10^5/q$ heat release of the heat sources over the layer half-thickness: $z_1 = 0.25$ m, $B = 1$ T, $v = 8 \times 10^3$ m/s, $k_0 = 4.85$ m^{-1}, $\omega = 3.88 \times 10^4$ s^{-1}, and $q = (Bj)^2/\rho z_1 c$.

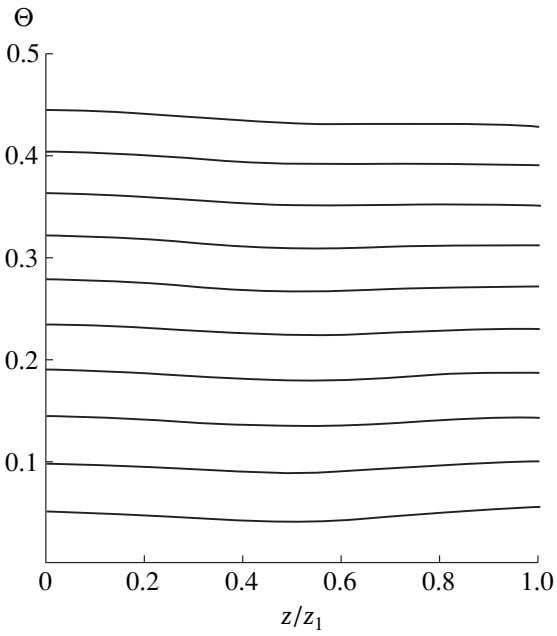

Fig. 2. The distribution of temperature Θ over the layer half-thickness for Fo = 0.1–0.2 with a step of 0.2.

equation for dimensionless temperature $\Theta = (T - T_0)\rho c a/q z_1^2$,

$$\frac{\partial \Theta}{\partial \mathrm{Fo}} = \frac{\partial^2 \Theta}{\partial \zeta^2} + \frac{q_\gamma + q_\sigma}{q}, \qquad (8)$$

where a is the thermal diffusivity, c is the heat capacity, ρ is the density of the layer material, $\zeta = z/z_1$, and $\mathrm{Fo} = at/z_1^2$ is the Fourier number.

We assume that the initial temperature of the layer $\Theta(\zeta, 0) = 0$ is equal to the ambient temperature T_0 and the layer proper is in the state of convective heat exchange with the ambient medium.

Equation (8) with the heat sources described above may be solved analytically using the Laplace transform in time. Figure 2 is a graphic representation of the solution $\Theta(\zeta)$ found for different values of the Fourier number. The Biot criterion $\mathrm{Bi} = Hz_1$ (H is the heat-transfer coefficient) was taken to be 0.1.

As seen in Fig. 2, the temperature field throughout the entire process of layer heating proves to be actually nongradient, which does not affect the quality of the material being processed. At the same time, the direct supply of energy to the bulk of the layer, which is due to the presence of a constant magnetic field, results in a sharp reduction of the time required to process an article. Finally, note that the effective bulk heating of some materials (for example, metals) has a favorable effect on the subsequent technological operations (welding, cutting, etc.).

REFERENCES

1. Ya. S. Podstrigach, Ya. I. Burak, and V. F. Kondrat, *Magnetothermoelasticity of Conducting Bodies* (Naukova Dumka, Kiev, 1982).
2. M. I. Kiselev, S. Yu. Ryzhkov, S. V. Sobolev, *et al.*, in *Physicochemical Processes of Treatment of Materials by Concentrated Energy Fluxes* (Nauka, Moscow, 1989), p. 226.
3. J. Burgers, *Magnetic Hydrodynamics* (Atomizdat, Moscow, 1958), p. 44.

Translated by H. Bronsteĭn

Technical Physics Letters, Vol. 26, No. 2, 2000, pp. 91–92. Translated from Pis'ma v Zhurnal Tekhnicheskoĭ Fiziki, Vol. 26, No. 3, 2000, pp. 1–5.

Recording High-Diffraction-Efficiency Holograms on a Photosemiconductor–Liquid Crystal Structure

N. L. Ivanova, A. N. Chaĭka, and A. P. Onokhov

Vavilov State Optical Institute, All-Russia Research Center, St. Petersburg, 193171 Russia

Received August 11, 1999

Abstract—Experimental real-time holograms were recorded on a structure comprising a liquid crystal and a *p–i–n*-diode based on a hydrogenated amorphous silicon. The holograms offer unprecedented diffraction efficiency at acceptable spatial frequencies. *© 2000 MAIK "Nauka/Interperiodica".*

Some structures comprising a photosemiconductor and a liquid crystal (PSC–LC) provide a spatial resolution sufficiently high to enable real-time hologram recording for optical data processing [1]. It was demonstrated that reversible hologram recording is possible on a structure with a *p–i–n* maximum photodiode based on hydrogenated amorphous silicon (α-Si : H) and a nematic liquid crystal exhibiting the orientation twist effect, the latter serving as a modulating medium [2]. However, the maximum diffraction efficiency of the structure was comparatively low.

We have studied the possibility of creating a similar structure possessing a diffraction efficiency close to the theoretical limit [3]. We employed the orientation S-effect, with which the liquid crystal features controllable birefringence. The standard sandwich structure comprised a 1.2-μm-thick α-Si : H *p–i–n* photodiode and a nematic liquid crystal (NIOPIK ZhK 1282) with $\Delta n = 0.164$, $\varepsilon = 9.9$, and a thickness of 5 μm. The LC orientation was provided by cerium dioxide layers formed by oblique evaporation. The structure was studied in a transmission mode. The interference pattern of two coherent plane-wavefront beams from a He–Ne laser was created on the photosensitive PSC layer. The readout was performed at a wavelength of 0.814 μm, the modulator being aligned so that the LC director was parallel to the polarization vector of the readout beam.

The structure was powered with unipolar rectangular pulses. If a positive pulse is applied, then the *p–i–n*-diode occurs in the conducting state, the structure is insensitive to light, and almost all of the voltage drops across the LC layer, irrespective of the intensity of the recording beam incident on the photosensitive layer (the off state). If a negative pulse is applied, then the photodiode goes to the reverse-bias state and a birefringent phase grating arises in the liquid-crystal layer under the action of the sinusoidal interference pattern.

The diffraction efficiency was studied for a first-order diffracted light as a function of the recording-beam intensity and the spatial frequency of the grating, as well as the absolute amplitude and the repetition rate of the power-supplying electric pulses. The diffraction efficiency was computed as $\eta = I_1/I_0$, where I_1 is the intensity of a first-order diffracted light and I_0 is the intensity of the light transmitted through the modulator in the absence of the recording beam.

Figure 1 shows the maximum diffraction efficiency plotted against the spatial frequency of the grating formed in the LC layer. The structure was powered with unipolar voltage pulses at an absolute pulse amplitude of 25 V and a pulse repetition rate of 10 Hz. The diffraction efficiency value η as high as 31.5% was obtained in the region of low spatial frequencies ($\nu = 28$ mm^{-1}). This result is close to the theoretical limit $\eta_{max} = 33.9\%$ computed for sinusoidally varying birefringence in a liquid crystal layer [4]. The structure is highly sensitive to the recording light: the diffraction efficiency attains its maximum at an intensity of 5.2 μW/cm^2 in each of the interferometer arms. Note a high resolution of the structure: the diffraction efficiency is reduced to 50% at

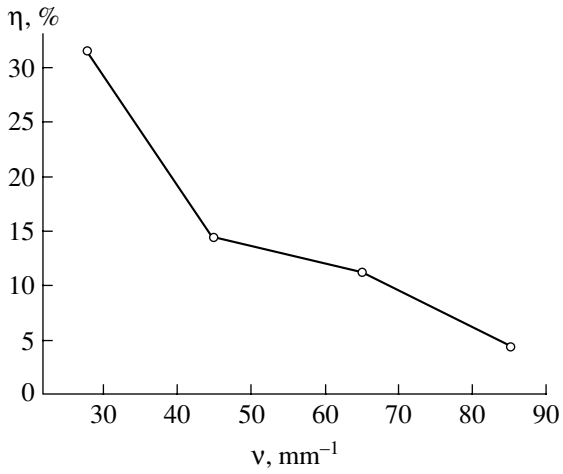

Fig. 1. Maximum diffraction efficiency versus the spatial frequency of the grating in the structure powered at an absolute pulse amplitude of 25 V and a pulse repetition rate of 10 Hz.

1063-7850/00/2602-0091$20.00

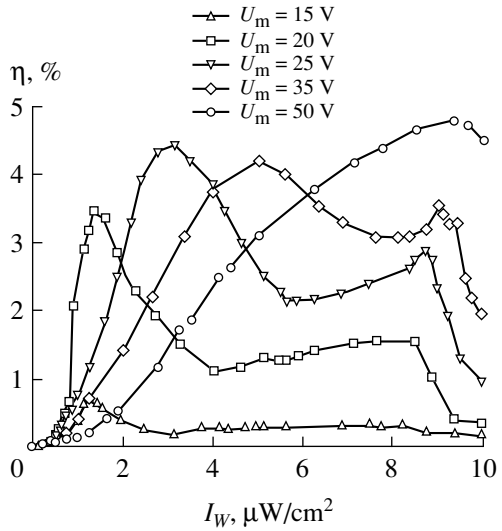

Fig. 2. Diffraction efficiency versus recording-beam intensity at a spatial frequency of 85 mm^{-1} for various absolute pulse amplitudes.

ν = 45 mm^{-1} and to 5% at ν = 85 mm^{-1}. These modulation parameters are achieved by means of a *p–i–n*-diode using hydrogenated amorphous silicon. If a reverse bias is applied to the diode, the voltage drops primarily across the high-resistance *i*-type layer. The layer is completely involved in the depletion region, where electric field is distributed almost uniformly between *p* and *n* contacts. The field is so strong that photogenerated carriers crossing the *i*-type layer have no time to recombinate or deviate in the transverse direction. Thus, the loss in the depth of modulation in transforming an input interference pattern into a modulating electric field is less than that in the case where the entire photosensitive layer is made of an intrinsic semiconductor.

Figure 2 shows the diffraction efficiency as a function of the recording beam intensity I_W (measured in one of the interferometer arms) at various absolute pulse amplitudes for the repetition rate 10 Hz. The spatial frequency of the grating formed was 85 mm^{-1}. The curves have an oscillatory shape resulting from the S-effect in the liquid crystal. They can serve as the basis for evaluating the operating range of the modulator and for choosing optimal conditions of reversible hologram recording. The effect of the pulse amplitude on the slope of the modulation characteristics and on the dynamic range may be important to the design of parametric optical logic [5].

ACKNOWLEDGMENTS

We are grateful to A.V. Pavlov for helpful discussion.

This study was funded by the Russian Foundation for Basic Research, project no. 98-02-18189.

REFERENCES

1. S. Fukushima and T. Kurokawa, Appl. Phys. Lett. **58**, 787 (1991).
2. A. N. Chaĭka, N. L. Ivanova, A. P. Onokhov, *et al.*, Pis'ma Zh. Tekh. Fiz. **21**, 83 (1995).
3. N. Mukohzaka, N. Yoshida, H. Toyoda, *et al.*, Appl. Opt. **33**, 2804 (1994).
4. E. Hamakava, in *Current Topics in Photovoltages*, Ed. by T. Coutts and J. Meakin (Academic Press, London, 1985).
5. A. V. Pavlov, in *Proceedings of the International Conference "Soft Computing and Measurement" (SCM'90), St. Petersburg, Russia, 1999* (St. Petersburg, 1999), Vol. 1, p. 218.

Translated by A. A. Sharshakov

Technical Physics Letters, Vol. 26, No. 2, 2000, pp. 93–95. Translated from Pis'ma v Zhurnal Tekhnicheskoĭ Fiziki, Vol. 26, No. 3, 2000, pp. 6–11.

Features in the Dielectric Properties and Temperature-Composition Phase Diagrams of $NaNbO_3$–$A_{0.5}Bi_{0.5}TiO_3$ (A = Li, Na, K, Ag) Solid Solutions

I. P. Raevskiĭ, L. A. Reznichenko, and M. A. Malitskaya

Research Institute of Physics, Rostov State University, Rostov-on-Don, 344104 Russia

Received July 14, 1999

Abstract—In the systems of solid solutions $(1 - x)NaNbO_3 - xA_{0.5}Bi_{0.5}TiO_3$, where A is Li (I), Na(II), K(III), and Ag(IV), the concentration dependence of the temperature T_m, corresponding to a maximum in the dielectric permittivity ε, is described by a curve with minimum. In systems II and IV, a "break" is observed on the $T_m(x)$ dependences in the region of $x \approx 0.2$, and the compositions with $x < 0.2$ are characterized by anomalously large temperature hysteresis of $\varepsilon(T)$ reaching 80–100 K. Some compositions of systems I and III have very diffuse peaks of $\varepsilon(T)$ in the room temperature range, which is of interest from the standpoint of search for lead-free relaxer materials. © *2000 MAIK "Nauka/Interperiodica".*

In view of increasing environmental requirements placed on the production of ceramics, an intensive search has been undertaken in recent years for new lead-free ferroelectric (FE) materials for various applications [1–4]. At present, ferroelectric ceramics based on alkali metal niobates and sodium–bismuth titanate [1–3] are treated as the most likely alternative to lead-containing piezoelectric and pyroelectric materials. The search for the so-called relaxer materials characterized by significant smearing of the peak of dielectric permittivity ε and by a strong frequency dependence of ε is conducted mainly among solid solutions of barium titanate, in particular, with alkali metal niobates [4]. However, the problem of preparing lead-free materials with a very broad maximum of $\varepsilon(T)$ in the room temperature range remains unsolved [4], which adds urgency to further investigations pursuing this objective. We have investigated the dielectric properties of ceramics based on the solid solutions of antiferroelectric $NaNbO_3$ with ternary compounds $A_{0.5}Bi_{0.5}TiO_3$ for the purpose of determining the features of their properties in comparison with the well-studied solid solutions of $NaNbO_3$ with compounds of the ABO_3 type [5–7], as well as of assessing the possibility of using the new systems as the basis of lead-free functional materials. The second components in the solid solutions studied are $A_{0.5}Bi_{0.5}TiO_3$ oxides, of which two (A = Na, K) are known as ferroelectrics (FE) [5]. $Na_{0.5}Bi_{0.5}TiO_3$ contains also an antiferroelectric (AFE) phase [5]. The $A_{0.5}Bi_{0.5}TiO_3$ oxides in which A is Li or Ag do not crystallize in the perovskite structure under normal conditions. However, the perovskite modification of $Ag_{0.5}Bi_{0.5}TiO_3$ synthesized recently at a pressure of 14 GPa exhibited an $\varepsilon(T)$ maximum in the region of 580 K, which is indicative of the presence of FE or AFE properties [8]. To present, $Li_{0.5}Bi_{0.5}TiO_3$ was not obtained in the perovskite structure. However, this compound has been long used as a component increasing the Curie point of $PbTiO_3$-based piezoceramic materials [9], which also suggests the presence of FE or AFE properties.

Ceramic samples of the systems $(1 - x)NaNbO_3 - xA_{0.5}Bi_{0.5}TiO_3$, where A is Li (I), Na (II), K (III), or Ag (IV) with $0 < x < 0.3$, were prepared by solid-phase synthesis with subsequent hot pressing (II and III) or annealing without pressure (I and IV). X-ray diffraction analysis showed that all of the investigated compositions were single-phase and had a structure of the perovskite type. After polishing, silver electrodes were deposited onto the samples in the form of disks 10 mm in diameter and 1 mm thick by the method of paste fusing. The measurements of ε were performed using an R5083 capacitance bridge in the course of continuous heating or cooling a sample at a rate of 2–5 K/min.

Figure 1 shows the concentration dependence of the temperature T_m of the maximum of $\varepsilon(T)$ for solid solutions of the investigated systems. In all systems, the $T_m(x)$ curves exhibit a minimum. Therefore, the solid solutions of $NaNbO_3$ with ternary oxides $A_{0.5}Bi_{0.5}TiO_3$, obey a rule that was previously established for binary systems of mixed oxides of the ABO_3 type. According to this rule, the curve $T_m(x)$ has a minimum if the extreme system components have no cations in common [10, 11]. In the solid solutions of other ternary perovskites, for example, of the $PbB'_nB''_mO_3$ type, this rule is not always valid because of the effects of composition ordering of B' and B" ions [12].

1063-7850/00/2602-0093$20.00 © 2000 MAIK "Nauka/Interperiodica"

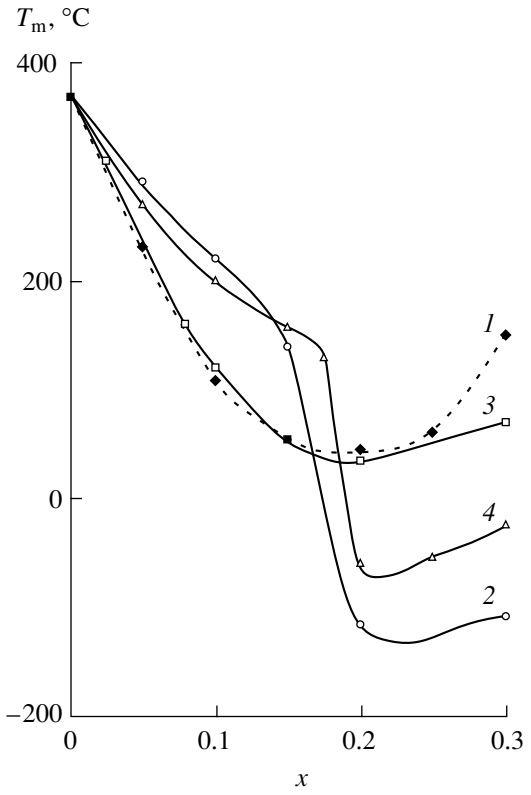

Fig. 1. The concentration dependence of temperature T_m of the maximum of dielectric permittivity ε measured at a frequency of 1 kHz in the course of heating of $(1 - x)NaNbO_3 - xA_{0.5}Bi_{0.5}TiO_3$ solid solutions, where A is (*1*) Li, (*2*) Na, (*3*) K, and (*4*) Ag.

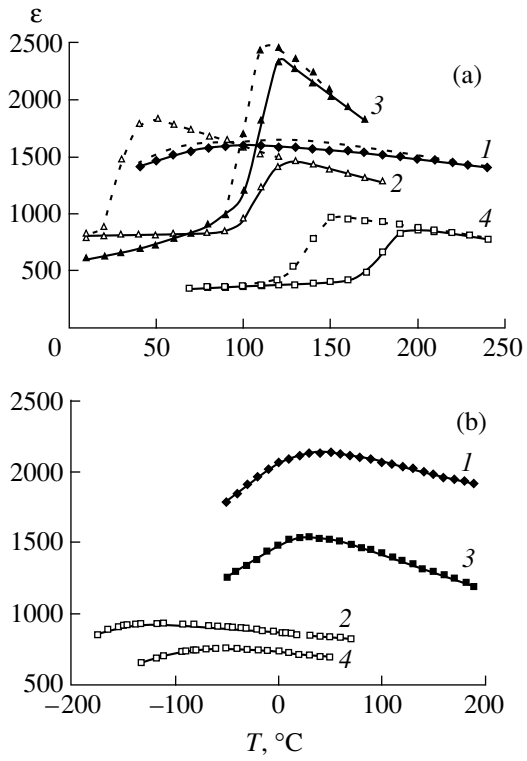

Fig. 2. The ε(*T*) dependence of $(1 - x)NaNbO_3 - xA_{0.5}Bi_{0.5}TiO_3$ solid solutions, where A is (*1*) Li, (*2*) Na, (*3*) K, and (*4*) Ag, measured at a frequency of 1 kHz in the course of heating (solid lines) or cooling (broken lines). The sample compositions: (a) from the region $x < x_0$, where x_0 is the concentration of second component, corresponding to a "break" in the dependence $T_m(x)$, $x = 0.1$ (*1–4*); (b) the corresponding regions of minimum of the $T_m(x)$ plots, $x =$ 0.2 (*1*); 0.3 (*2*); 0.2 (*3*); 0.25 (*4*).

It was previously found [5] that niobate-based systems, similarly to other AFE oxides of the perovskite family, may be divided into two groups. A high-temperature FE phase may form in the solid solutions of group I, and no such phases arise in group II. At the same time (unlike, for example, well-studied $PbZrO_3$-based systems), in the phase diagrams of $NaNbO_3$-based systems of group II exhibit a break of the line of the AFE phase transition at a certain concentration x_0 of the second component. As seen in Fig. 1, a break in the region of $x \approx 0.2$ is observed on the $T_m(x)$ curves of the samples belonging to systems II and IV, while T_m in systems I and III varies smoothly with increasing x. It was reported [6, 7] that, in solid solutions of $NaNbO_3$ with oxides of the ABO_3 type, a fairly reliable experimental feature indicating that a given composition belongs to group II is provided by the presence of an anomalously large temperature hysteresis of the ε(*T*) curves in the samples with $x < x_0$. As is seen in Fig. 2a, the compositions of systems II and IV with $x = 0.10$ are indeed characterized by an anomalously large temperature hysteresis of ε(*T*) reaching 80–100 K. The obtained results provide additional evidence of the fact that systems I and III belong to group I, and systems II and IV, to group II according to the classification of [5]. Lisitsyna *et al.* [7] demonstrated that, by determining the group to which a $NaNbO_3$-based solid solution belongs, one can also solve a frequently encountered inverse problem, namely, determine whether the second component of the solid solution is FE or AFE, provided that this component is known to possess anomalous dielectric properties (if it is for some reason difficult to perform direct measurements). As mentioned above, the available literature data suggest the presence of FE or AFE properties in perovskite modifications of $Ag_{0.5}Bi_{0.5}TiO_3$ and $Li_{0.5}Bi_{0.5}TiO_3$ (which may be synthesized only under high pressure conditions) [8, 9]. The results obtained by us indicate that $Ag_{0.5}Bi_{0.5}TiO_3$ is apparently AFE, and $Li_{0.5}Bi_{0.5}TiO_3$ is FE.

Figure 2b presents the ε(*T*) curves for the compositions of the solid solution systems investigated characterized by the presence of minima in the $T_m(x)$ plots. As seen, the curves are very diffuse, which agrees with the data [10, 13] indicating that solid solutions from this

range of compositions are characterized by maximum smearing of the peaks of $\varepsilon(T)$. As the frequency increases, the peaks of $\varepsilon(T)$ shift toward high temperatures (by 5–10 K with the frequency varying from 1 to 100 kHz), i.e., these materials possess relaxer properties. Of special interest from the standpoint of possible applications are the compositions of systems I and III, in which the values of ε are much higher than those in systems II and IV, while the maxima of $\varepsilon(T)$ lie in the room temperature range.

Therefore, the form of the temperature-composition phase diagrams, as well as the character of variation of the dielectric properties depending on the content of the second component in solid solutions of $NaNbO_3$ with ternary oxides $A_{0.5}Bi_{0.5}TiO_3$, agree with the regularities found previously for binary systems of mixed oxides of the ABO_3 type. The presence of very diffuse maxima of $\varepsilon(T)$ in the room temperature range in a number of compositions of systems I and III is of interest from the standpoint of search for lead-free relaxer materials.

ACKNOWLEDGMENTS

This study was supported in part by the Russian Foundation for Basic Research, project no. 99-02-17575.

REFERENCES

1. T. Takenaka and K. Sakata, Ferroelectrics **95**, 153 (1989).
2. T. Takenaka and H. Nagata, in *Abstracts of ISAF XI'98, Montreux, Switzerland, 1998*, p. 13.
3. A. Ya. Dantsiger, O. N. Razumovskaya, L. A. Reznichenko, *et al.*, *High-Efficiency Piezoceramic Materials: Optimization of Search* (Paik, Rostov-on-Don, 1995).
4. J. Ravez and A. Simon, J. Korean Phys. Soc. **32** (Suppl.), S955 (1998).
5. G. A. Smolenskiĭ, V. A. Bokov, V. A. Isupov, *et al.*, *The Physics of Ferroelectric Phenomena* (Nauka, Leningrad, 1985).
6. I. P. Raevskiĭ, V. G. Smotrakov, S. O. Lisitsyna, *et al.*, Neorg. Mater. **21**, 846 (1985).
7. S. O. Lisitsyna, I. P. Raevskiĭ, and G. A. Geguzina, Zh. Tekh. Fiz. **56**, 1150 (1986) [Sov. Phys. Tech. Phys. **31**, 673 (1986)].
8. J.-H. Park, P. N. Woodward, J. B. Parise, *et al.*, Chem. Mater. **11**, 177 (1999).
9. T. Takenaka and K. Sakata, Jpn. J. Appl. Phys. **22** (Suppl. 22-3), 118 (1983).
10. G. I. Smolenskiĭ, A. I. Agranovskaya, and N. N. Kraĭnik, Dokl. Akad. Nauk SSSR **91**, 55 (1953) [Sov. Phys. Doklady **91** (1) (1953)].
11. T. Y. Tien, E. C. Subbarao, and J. Hrizo, J. Am. Ceram. Soc. **45**, 572 (1962).
12. A. A. Bokov and I. P. Rayevsky, Ferroelectrics **144**, 147 (1993).
13. I. P. Raevskiĭ, L. M. Proskuryakova, L. A. Reznichenko, *et al.*, Izv. Vyssh. Uchebn. Zaved., Fiz., No. 2, 152 (1978).

Translated by H. Bronsteĭn

Technical Physics Letters, Vol. 26, No. 2, 2000, pp. 96–98. Translated from Pis'ma v Zhurnal Tekhnicheskoĭ Fiziki, Vol. 26, No. 3, 2000, pp. 12–17.

Microwave Bandpass Filter Based on a Superconductor/Ferrite (YBCO/YIG) Film Structure

S. F. Karmanenko and A. A. Semenov

St. Petersburg State University of Electrical Engineering, St. Petersburg, Russia

Received July 15, 1999

Abstract—Effective practical uses of HTSC/YIG film structures are demonstrated. Controlled microwave filters based on HTSC/YIG film structures may find practical application in communication and radar equipment.

Possible practical applications of the unique physical phenomena, such as spin waves (SW) [1] and high-temperature superconductivity (HTSC), have been subjected to investigation in recent years in view of intensive development of radiotelephony and wireless telecommunications [2, 3]. The band-pass filter (BPF) is an instrument that is most generally employed in various means of communication. The basic requirements placed on a modern radioelectronic BPF include a narrow bandwidth, an almost zero level of losses, a high front steepness, and the possibility of frequency tuning [3].

Spin waves propagate in single crystals and epitaxial films of yttrium iron garnet $Y_2Fe_5O_{12}$ (YIG) with an extremely small specific attenuation in a wide frequency range. Main difficulties in developing SW devices involving YIG films are related to their low thermal stability and a relatively high level of signal transformation losses. Therefore, a combination of $YBa_2Cu_3O_{7-x}$ (YBCO) superconductor film transducers with YIG films in which spin waves are excited under a fixed cryogenic temperature appear a promising line of research and development in radioelectronics.

It was the objective of this study to investigate the possibility of using superconducting antennas in a tunable radioelectronic BPF based on the traveling wave principle.

The experiments were performed with an epitaxial YIG ferrite film grown on a gadolinium gallium garnet (GGG) substrate and characterized by the following parameters: the saturation magnetization M_s = 1200 G, the thickness h = 62 μm, and the crystallographic orientation (111). Films of this type are very suitable for constructing a BPF based on a superconductor/ferrite structure, functioning at a temperature of 77 K in one of the promising microwave ranges of 1–3 GHz employed by developers of base stations for cellular radiotelephony. In addition, a low magnetic field applied to the structure produces a lower effect on the superconductor film and its surface resistance [4].

A spin waveguide cut from the YIG film in the form of a 2 × 7 × 0.55 mm trapezoid (Fig. 1a) was applied directly to the film structure of an antenna. The ends of the ferrite waveguide structure were cut at an angle of ~30° to exclude the reflection of SW from the waveguide edge.

The topology of radiating and receiving transducers is shown in Fig. 1b: two microstrip segments bent at an angle of 90° are located on a substrate sized 17 × 6 × 0.5 mm. Two dimensions of the antenna topology were varied, namely, the width of the microstrip in its part joined to the YIG film (W) and the distance between the antennas (L). Antennas with W = 15, 50, and 500 μm were used in the experiments. The width of the conducting microstrip line was 500 μm. Along with super-

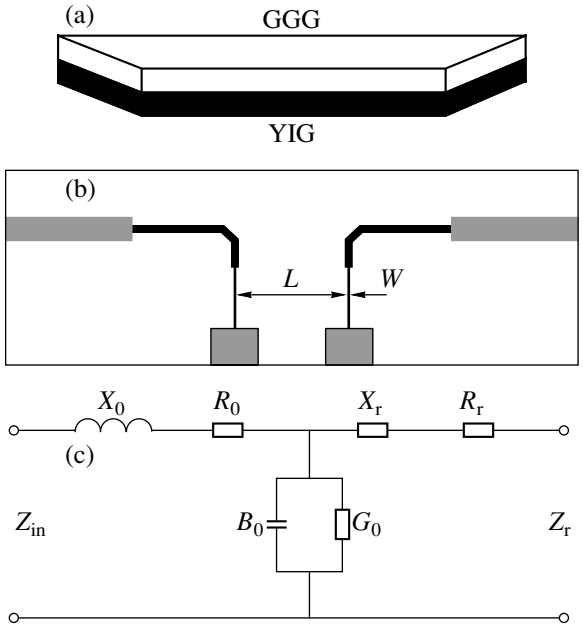

Fig. 1. Schematic diagrams of (a) waveguide structure, (b) antenna topology, and (c) an equivalent circuit of microstrip antenna.

1063-7850/00/2602-0096$20.00 © 2000 MAIK "Nauka/Interperiodica"

conducting microstrip antennas, we used similar structures with copper transducers.

Figure 1c illustrates a model of microstrip antenna, where R_0, X_0, B_0, and G_0 are the long line parameters in the absence of radiation, and $Z_r = R_r + iX_r$ is the complex radiation impedance [1]. The reduction of losses in a device with superconducting transducers may be associated only with variation of the primary long line parameters, and the radiation resistance does not depend on the transducer material. It is probable that, in case of slot or coplanar antennas used to excite spin waves, a difference in the levels of losses in superconductor and metal antennas will be more significant, because these antenna structures will be characterized by additional losses due to the spin wave propagation along the ferromagnetic–antenna transducer interface.

The superconducting YBCO films were grown on both sides of $LaAlO_3$ (LAO) substrates by dc magnetron sputtering [5] and were subjected to photolithography and chemical etching. The YBCO films were 0.7–1.0 μm thick. Layered compositions of contact pads (Au/Ag), thermocompression, and brazing were used to ensure a reliable transition from a YBCO microstrip to coaxial lines of the breadboard. The housing structure incorporated miniature electromagnets with cores, which were used to develop a uniform magnetic field with the magnetic vector parallel to the surface of the YIG film and perpendicular to the direction of SW propagation. For performing measurements under cryogenic temperature, the housing design provided for the possibility of its immersion into a tank with liquid nitrogen.

The experimental setup for obtaining the amplitude-frequency characteristics (AFC) of a filter was based on an R2-54 panoramic voltage standing wave ratio meter. For recording the obtained characteristics and their further processing, a computer was connected to the meter via special interface.

As a result of measurements, we obtained the AFCs of spin-wave BPFs for different combinations of ferrite elements, antenna transducers, and the experimental temperature. Of most interest are the results of comparison of the characteristics of similar structures based on different antenna materials, measured at $T = 77$ K. Figure 2 gives two AFCs for an antenna structure with $W = 500$ μm and $L = 5$ mm. Curve *1* corresponds to a setup with superconducting antennas, and curve *2*, to that with copper antennas. A difference in the level of losses in the transmission band (2 dB) is due to a lower surface resistance in superconductor antennas.

Figure 3 gives the transmission characteristics of the experimental setup, taken for different magnetizing fields, from which one can see that an insignificant variation of the magnetizing field strength (70 Oe) shifts the center frequency by 600 MHz. Such a high sensitivity to changes in the BPF parameters is very promising for constructing controlled microwave-frequency filters. The investigated BPF design is disadvantageous in that the level of losses in the transmission band also varies as a result of tuning of the center frequency.

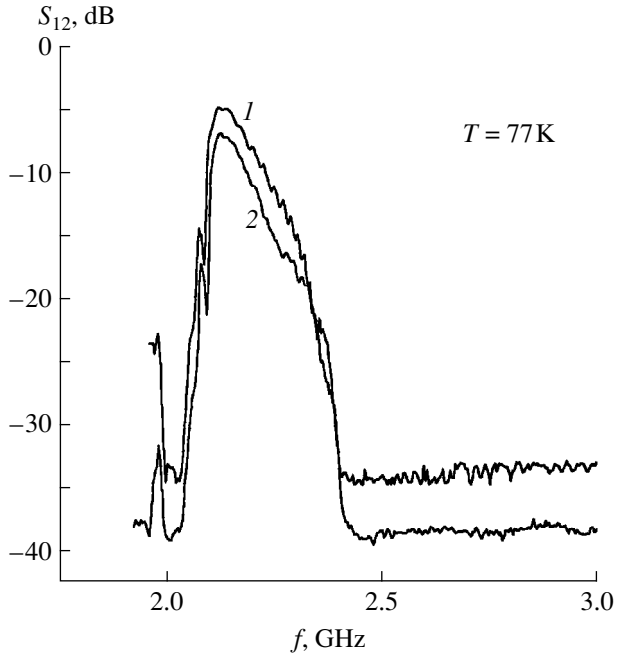

Fig. 2. Transmission characteristics of the experimental setup (*1*) with superconducting antennas and (*2*) with copper antennas.

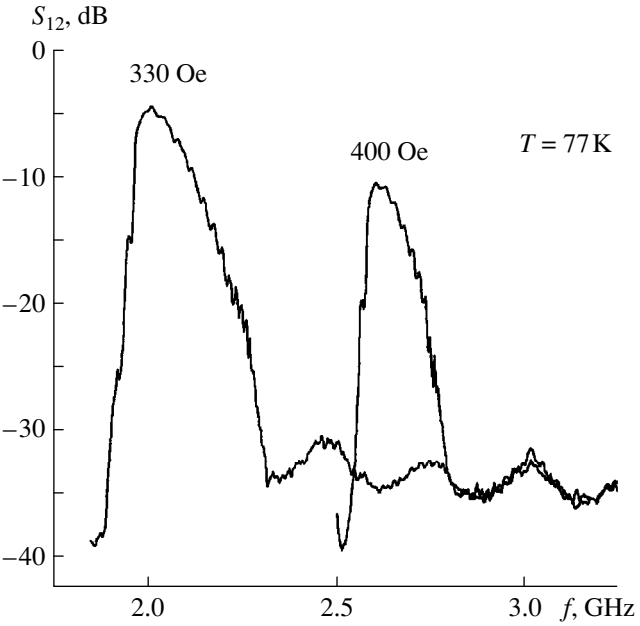

Fig. 3. Rearrangement of the characteristic of a filter with superconducting antennas as a result of variation of the magnetizing field.

The experiments resulted mainly in demonstrating the possibility of construction and effective operation of cryogenic radioelectronic devices utilizing an HTSC/YIG film structure and their advantages over

similar metal/YIG structures. We used a simplest microstrip antenna topology in this experimental investigations. The use of microstrip transducers in the form of inphase and antiphase lattices [6], BPF designs with limiting and switching elements in HTSC antennas, and combined designs of bandpass and bandstop filters are capable of improving the characteristics of controlled cryogenic SW BPFs and promoting their practical use.

REFERENCES

1. V. F. Dmitriev and B. A. Kalinikos, Izv. Vyssh. Uchebn. Zaved., Fiz., No. 11, 24 (1988).
2. Z.-Y. Shen, *High-Temperature Superconducting Microwave Circuit* (Artech House, Nortwood, 1994).
3. R. B. Hammond, D. J. Scalarino, J. R. Schrieffer, *et al.*, Microwave J. Euro-global ed. **41**, 94 (1998).
4. M. M. Gaĭdukov, S. F. Karmanenko, A. B. Kozyrev, *et al.*, Supercond. Sci. Technol. **7**, 721 (1994).
5. S. F. Karmanenko, Supercond. Sci. Technol. **12**, 36 (1999).
6. A. V. Zhuravlev, S. F. Karmanenko, E. V. Nam, *et al.*, in *Proceedings of IEEE-Russia MIAME'97 Conference on Microwave Electronics, Novosibirsk, Russia, 1997*, p. 69.

Translated by H. Bronsteĭn

Technical Physics Letters, Vol. 26, No. 2, 2000, pp. 99–101. Translated from Pis'ma v Zhurnal Tekhnicheskoĭ Fiziki, Vol. 26, No. 3, 2000, pp. 18–22.

Coupled States in a Curved Nanostructure

S. Albeverio*, V. A. Geĭler*, and V. A. Margulis**

** Institut für Angewandte Mathematik und Stochastic, Universität Bonn, Bonn, D-53115 Germany*

*** Ogarev State University, Saransk, Mordovia, Russia*

Received October 4, 1999

Abstract—The spectrum of a Schrödinger operator with the zero-radius potential in a nanostructure of a constant total curvature is considered. Positions of the coupled states in a well of zero radius and the corresponding binding energy are determined. Their dependence on the scattering length and curvature is studied. The condition of the formation of the coupled state is determined. *© 2000 MAIK "Nauka/Interperiodica".*

The recent development of a technique for manufacturing the curved 2D layers in nanostructures [1] makes it necessary to study theoretically the properties of electron systems in such layers. Interesting physical effects determined by the influence of the curvature on the electronic energy spectrum were studied in [1–4]. The possibility of manufacturing the fullerene-like structures with negative surface curvature was demonstrated in [5]. Models of the quantum Hall effect at the surfaces of both positive and negative curvature were considered in [6–8]. In all these systems, it is important to take into account the influence of the short-range impurity centers on the energy spectrum of electrons. In connection with this, we consider the impurity-coupled states in layers of a constant Gaussian curvature. The impurity potential was represented by a zero-radius potential (point potential) that has proved to be effective in solving a wide variety of problems in theoretical physics [9–12]. Models with the zero-radius potentials allow one to obtain both qualitative and quantitative results suitable for practical applications [10, 12]. This is especially true for the systems with small binding energies. The point potentials can be used for the study of periodic systems in the layers of constant negative curvature [13].

Our work is aimed at obtaining explicit formulas for the discrete levels of weakly coupled quantum systems with the use of the zero-radius potential at the surfaces of constant Gaussian curvature K and at studying their dependence on K. Hamiltonian H^0 of a free particle can be presented in our case as $H^0 = -(\hbar^2/2m)\Delta_{LB}$, where Δ_{LB} is Laplace–Beltrami operator [14]. Consider a perturbation of the Hamiltonian H^0 by a zero-radius potential centered in point q. The introduction of such a potential is equivalent to imposing a boundary condition in point q that is determined by a real parameter α related to the length λ of scattering at the potential by the relationship $\pi\hbar^2\alpha/m = -ln\lambda$. The Green function $G_E(x, y)$ of the perturbed operator H can be expressed via the Green function $G_E^0(x, y)$ of the operator H^0 with the help of the Kreĭn formula for resolvents [11, 12]:

$$G_E(x, y) = G_E^0(x, y) - [Q(E) + \alpha]^{-1} G_E^0(x, q) G_E^0(q, y), \quad (1)$$

where $Q(E)$ is the renormalized value of $G_E^0(x, y)$ at the diagonal $Q(E) = \lim_{x \to q}[G_E(x, q) + (m/\pi\hbar^2)\ln\rho(x, q)]$ and ρ is the geodesic distance at the surface. A coupled state (if it does exist) with the energy $E_0 \equiv E_0(K)$ in the zero-radius potential lies below the energy of the ground state ε_0 of the Hamiltonian H^0 (note that $\varepsilon_0 > 0$ if $K < 0$ and $\varepsilon_0 = 0$ if $K \geq 0$). It follows from (1) that energy E_0 satisfies the equation:

$$Q(E) + \alpha = 0. \quad (2)$$

A normalized eigenfunction corresponding to the state E_0 is given by

$$\Psi_0(x) = [Q'(E_0)]^{-1/2} G_{E_0}(x, q).$$

Let us first consider the case $K > 0$ (a sphere with the radius $a = K^{-1/2}$). In this case, $-\Delta_{LB}$ is the operator of the square angular momentum $\mathbf{L}^2$. It is well known that the spectrum of H^0 is discrete and consists of the degenerate levels $\varepsilon_l = (\hbar^2/2ma^2)l(l + 1)$ with the multiplicity $2l + 1$ ($l = 0, 1, \ldots$). Using an expression for G_E^0 [14]:

$$G_E^0(x, y) = \frac{m}{2\hbar^2 \cos(\pi\zeta/2)} \times \mathcal{P}_{-1/2+\zeta}(-\cos(\rho(x, y)/a)), \quad (3)$$

where $\mathcal{P}_\mu(x)$ is Legendre function,

$$\zeta \equiv \zeta(E) = \left[\frac{1}{4} + \frac{2mE}{\hbar^2 K}\right]^{1/2}, \quad (4)$$

we obtain:

$$Q(E) = -\frac{m}{\pi\hbar^2}\left[\psi\left(\frac{1}{2}+\zeta\right) - \frac{\pi}{2}\tan(\pi\zeta) - \ln(2a) + \gamma\right], \quad (5)$$

where $\psi(x)$ is the logarithmic derivative of the Euler Γ-function and $\gamma = -\psi(1)$ is the Euler constant.

It follows from (5) that $\lim_{E\to-\infty} Q(E) = -\infty$, $\lim_{E\to\varepsilon_l-0} Q(E) = +\infty$, and $\lim_{E\to\varepsilon_l+0} Q(E) = -\infty$. Hence, for any α equation (2) has only one solution E_l, $l = 0, 1, \ldots$ in each of the segments $(-\infty, \varepsilon_0)$, $(0, \varepsilon_1)$, …, $(\varepsilon_l, \varepsilon_{l+1})$, … . Therefore, the spectrum of H consists of simple eigenvalues E_l, $l \geq 0$ and the levels ε_l, $l \leq 1$ (the multiplicity of which in the spectrum of H is $2l$). Consider the most important extreme cases using the asymptotics $Q(E)$ for the case $|2ma^2E/\hbar^2 - (l+1)| \ll 1$ and for $E \longrightarrow -\infty$.

For $\lambda \ll a$ we have $E_0(K) \simeq -2\hbar^2/e^{2\gamma}m\lambda^2$ and $E_1(K) \simeq \hbar^2/4ma^2\ln(2a\lambda^{-1})$. Since $E_0(0) = -2\hbar^2/e^{2\gamma}m\lambda^2$ [12], the positive curvature does not virtually influence the value of the ground state energy. On the other hand $E_1(K) - E_0(K) > \varepsilon_0 - E_0(0)$, that is, the binding energy increases with the curvature.

In the case of $\lambda \gg a$, we have $E_0(K) \simeq \hbar^2/4ma^2\ln(2a\lambda^{-1})$, $E_1(K) \simeq \hbar^2/ma^2 + 3\hbar^2/4ma^2\ln(2a/e\lambda)$, and, hence, $E_1(K) - E_0(K) < \varepsilon_1 - \varepsilon_0$, that is, the well of zero radius decreases the binding energy if the curvature is large.

Finally, if a and λ are comparable (specifically, if $\lambda \sim 8a$), then

$$E_0(K) \simeq -\frac{\hbar^2}{8ma^2} - \frac{\hbar^2}{ma^2\psi''(1/2)}\ln\frac{\lambda}{8a}.$$

Thus, the energy of the coupled state for moderate values of a in this case is higher by almost one order of magnitude than the corresponding energy for $K = 0$.

Consider now the case of $K < 0$ (a pseudosphere of the radius $a = |K|^{-1/2}$). In this case, the continuous spectrum of H^0 occupies the semiaxis $E \geq \varepsilon_0(K) = \hbar^2/8ma^2$. Green function of the operator H^0 is given by an explicit formula [14]:

$$G_E^0(x,y) = \frac{m}{2\pi\hbar^2}\frac{\Gamma^2(1/2+\zeta)}{\Gamma(1+2\zeta)}\left(\cosh\frac{\rho(x,y)}{a}\right)^{-1-\zeta} \times F\left(\frac{1}{2}+\zeta, \frac{1}{2}+\zeta; 1+2\zeta; \cosh^{-1}\frac{\rho(x,y)}{a}\right), \quad (6)$$

where $F(a, b, c; z)$ is a hypergeometric function and ζ is given by the formula (4). From (6) we obtain [13]: $Q(E) = -(m/\pi\hbar^2)[\psi(1/2+\zeta) - \ln 2a + \gamma]$. This case is substantially different from the case when $K \geq 0$: only a well with the scattering length $\lambda < 8a$, rather than any well of zero radius, is capable of coupling. The spectrum of H comprises all the points of the continuous spectrum of the operator H^0 and the level E_0 (if any). Therefore, the negative curvature can "squeeze" a level out of the well into the continuous spectrum. A level that just appears ($\lambda \sim 8a$) can be determined from the formula $E_0 \simeq \hbar^2/8ma^2\{1 - 4/\pi^4)[\ln(8a/\lambda)]^2\}$.

In the extreme case of a sufficiently deep well $\lambda \ll a$, we have $E_0(K) \simeq E_0(0) + (\hbar/a)\sqrt{-E_0(0)/2m}$ and, hence, in the case of $K < 0$ the curvature substantially influences the position of the level in a deep well, thus decreasing the binding energy. A simple estimate can be given for the case $\lambda \sim 2a$: $E_0(K) \simeq (\pi^2\hbar^2/12ma^2)\ln(\lambda/2a)$ and the binding energy is also lower than that in the case $K = 0$.

The following conclusions can be derived from the results presented above. In the case when $K > 0$, the spectrum is discrete and the level in the zero-radius well goes down along the E axis. However, in a deep well the level does not change (to within the accuracy of $O(|E|^{-1})$) and the binding energy increases with the curvature. In this case (similarly to the case $K = 0$) the level appears in a well with any scattering length.

In the case of $K < 0$ (in contrast to the case of $K \geq 0$) the condition $\lambda < 8a$ is both necessary and sufficient for the appearance of the level. If this condition is met, the spectrum of H consists of the level E_0 and a continuous spectrum (semiaxis $E \geq \hbar^2|K|/8m$). The levels inside the well go up along the E axis, as well as does the edge of the continuous spectrum. The value of the gap $\varepsilon_0(K) - E_0(K)$ is smaller than that for the case of $K = 0$.

This work was supported by grants of the Russian Foundation for Basic Research and Ministry of Education of the Russian Federation.

REFERENCES

1. L. I. Magarill, D. A. Romanov, and A. V. Chaplik, Zh. Éksp. Teor. Fiz. **113**, 1411 (1998).
2. C. L. Foden, M. L. Leadbeater, J. Burroughes, *et al.*, J. Phys.: Condens. Matter. **6**, L127 (1994).
3. C. L. Foden, M. L. Leadbeater, and M. Pepper, Phys. Rev. B: Condens. Matter. **52**, 8646 (1995).
4. M. Encinosa and B. Etemadi, Phys. Rev. A: Gen. Phys. **58**, 77 (1998).
5. D. Vanderbilt and J. Tersoff, Phys. Rev. Lett. **68**, 511 (1992).

6. J. E. Avron, M. Kleĭn, and A. Pnueli, Phys. Rev. Lett. **69**, 128 (1992).
7. R. Lengo and D. Li, Nucl. Phys. B **413**, 735 (1994).
8. A. L. Carey, K. C. Hannabus, V. Mathaĭ, *et al.*, Commun. Math. Phys. **190**, 629 (1998).
9. A. I. Baz', Ya. B. Zel'dovich, and F. M. Perelomov, *Scattering, Reactions, and Decay in Nonrelativistic Quantum Mechanics* (Nauka, Moscow, 1971).
10. Yu. N. Demkov and V. N. Ostrovskiĭ, *Method of Zero Radius Potentials in Atomic Physics* (LGU, Leningrad, 1975).
11. B. S. Pavlov, Usp. Mat. Nauk **42**, 99 (1987).
12. S. Albeverio *et al.*, *Solvable Models in Quantum Mechanics* (Springer-Verlag, New York, 1988; Mir, Moscow, 1991).
13. Ĭ. Bryuning and V. A. Geĭler, Teor. Mat. Fiz. **119**, 368 (1999).
14. C. Grosche and F. Steĭner, *Handbook of Feynman Path Integrals* (Springer-Verlag, Berlin, 1998).

Translated by A. Chikishev